Università degli Studi di Perugia

Department of Physics and Geology

Dottorato in Scienza e Tecnologia
per la Fisica e la Geologia

Curriculum in Physics

XXXII Ciclo

Study of the upstream background for the measurement of the branching ratio of the $K^+ \to \pi^+ \nu \bar{\nu}$ decay with the NA62 experiment at CERN

PhD thesis

Candidate:
Riccardo Lollini

Supervisors:
Prof. Giuseppina Anzivino
Dr. Mauro Piccini

21 February 2020

CERN-THESIS-2020-299
21/02/2020

Abstract

The $K^+ \to \pi^+ \nu\bar{\nu}$ decay is one of the most sensitive channels suitable for finding indirect signals of new physics at high energy scales. The NA62 experiment at the CERN SPS plans on measuring the branching ratio of this decay with an unprecedented precision using a decay-in-flight technique. The kinematic selection of the signal is based on the reconstruction of the squared missing mass, obtained from the momentum of the parent K^+ and the π^+ in the final state. The main background sources include more abundant kaon decays such as $K^+ \to \pi^+\pi^0$, $K^+ \to \mu^+\nu_\mu$ and $K^+ \to \pi^+\pi^+\pi^-$, that under certain circumstances can mimic the experimental signature of the signal; in order to reduce the background due to these kaon decays, NA62 relies on the kinematic selection, an excellent timing between the sub-detectors, a good particle identification and muon rejection, and a hermetic photon veto. The main residual source of background is due to the so-called upstream background, which is any kaon decay or interaction happening before the fiducial decay region, matched to a pile-up particle in the upstream part of the detector. In this thesis I performed a $K^+ \to \pi^+ \nu\bar{\nu}$ selection that allowed to study and understand the features of the upstream background and measure it in the 2017 data set. This task is particularly difficult because of the non-trivial topology that these kind of events has in order to contribute to the background.

Every great story seems to begin with a snake.
— Nicolas Cage

Acknowledgements

I would like to thank all the people that helped me during the three years of the doctoral studies. A very special gratitude goes out to my supervisors, Prof. Giuseppina Anzivino and Dr. Mauro Piccini, for constantly helping, supporting and encouraging me. The advices they gave me are invaluable and I will always be grateful to them.

I would like to express my sincere gratitude to all the physicists of the Perugia NA62 group that helped me and became very dear friends, in particular Francesco Brizioli, Patrizia Cenci, Viacheslav Duk, Pasquale Lubrano, Monica Pepe and Roberto Piandani.

I owe Dr. Giuseppe Ruggiero a debt of gratitude. He introduced me to the technicalities of the $K^+ \to \pi^+ \nu \bar{\nu}$ measurement, without his help and his patience I could have never understood many of the subtleties of this analysis.

I am grateful to all the people of the NA62 Collaboration that helped me during my time at CERN and that, in one way or another, gave me plenty of opportunities to grow as a physicist and as a person.

I would also like to thank all the friends that were always there for me, Sara, the Aula Dottorandi A, Szabolcs, Samuel, Francisco, Susheel and all the other people that accompanied me in this journey.

I am especially grateful to my parents for all the sacrifices they have made on my behalf, my love for them cannot be expressed by words. Finally, I would like to thank my better half for always being there for me, teaching me to believe in myself and pushing me to always do my best.

Contents

List of Figures

Introduction

Precision measurements in the context of flavour physics are one of the most effective tools to investigate the presence of physics beyond the Standard Model. In particular, the branching ratio of the ultra-rare decay $K^+ \to \pi^+\nu\bar{\nu}$ is an extremely sensitive probe for New Physics. NA62 is a fixed target high-energy physics experiment located in the North Area of the CERN SPS. The experiment aims at measuring the branching ratio of $K^+ \to \pi^+\nu\bar{\nu}$ with an unprecedented precision. The Standard Model theoretical prediction for this branching ratio is

$$BR_{th}(K^+ \to \pi^+\nu\bar{\nu}) = (8.4 \pm 1.0) \times 10^{-11} \ ,$$

while the most precise experimental value, up to now, is

$$BR(K^+ \to \pi^+\nu\bar{\nu}) = (1.73^{+1.15}_{-1.05} \times 10^{-10}) \ .$$

This FCNC process is theoretically very clean and it is an important test for the unitarity of the CKM matrix in the Standard Model, besides being a very sensitive probe for New Physics in many scenarios beyond the Standard Model. The first NA62 data taking for $K^+ \to \pi^+\nu\bar{\nu}$ started in 2016 and lasted until the end of 2018; the analysis of the 2016 data led to the observation of 1 signal event. In September 2019 NA62 announced the observation of two more signal events that, when combined to the 2016 event, allowed us to put an upper limit on the branching ratio of the decay:

$$BR(K^+ \to \pi^+\nu\bar{\nu}) < 1.85 \times 10^{-10} \ \text{@90\%C.L.}$$

The main source of background in NA62, besides the more abundant kaon decays in the fiducial volume, is the so-called upstream background originated by early kaon decays or interactions before the fiducial decay volume. Understanding the complex mechanisms behind this unexpected background was extremely difficult and an enormous effort was made in order to understand how the background originated, how to suppress it and how to evaluate its contribution in the signal region. The study of all the technicalities concerning the upstream background is the core of this thesis.

In Chapter 1 the theoretical motivation for the measurement is given, with a short summary of the main features of the Standard Model that provide the context in which this measurement can be understood, and a summary of some of the models predicting relevant New Physics contributions to the branching ratio of $K^+ \to \pi^+ \nu \bar{\nu}$.

The NA62 detector is described in detail in Chapter 2 where the main role of all the sub-systems in the analysis is presented.

The description of the 2017 $K^+ \to \pi^+ \nu \bar{\nu}$ analysis can be found in Chapter 3. The chapter starts with an overview of the software framework and the definition of the data samples, and continues with the description of the main issues of the analysis, the main sources of background and how the signal can be selected and the background rejected.

In Chapter 4 the upstream background is presented in detail: how the upstream background originates, how it could contaminate the signal region, the strategies that can be used to suppress it and how the contribution of this background to the signal region can be evaluated. A full demonstration of the ineffectiveness of the 2016 technique for the evaluation of the upstream background is given and a new method is presented. In the last section of the chapter, a brief and preliminary overview of the upstream background in 2018 data is given.

The results of this work are presented in Chapter 5, together with the results obtained by the NA62 Collaboration for the measurement of the $K^+ \to \pi^+ \nu \bar{\nu}$ decay. The conclusions are given in Chapter 6, where results and future prospects are discussed.

Finally, an additional appendix was included, appendix A, reporting the work I have done on the CHOD detector software that was under my responsability from 2016 to 2019.

Chapter 1

Theoretical framework

In this chapter a general overview of the most important features of the Standard Model of particle physics will be given. The focus will be on the aspects more closely related to flavour physics and the NA62 experiment, e.g. the CKM matrix, the quark mixing and charged weak currents in the Kaon sector. Finally, the main features of the unitary triangle will be introduced with an emphasis on the theoretical motivation for the measurement of $K^+ \to \pi^+ \nu \bar{\nu}$ at NA62.

1.1 The Standard Model

Our current understanding of high energy physics is embodied in the *Standard Model* (SM) of particle physics, which describes the properties of the elementary particles and the interactions happening among them. The Standard Model is remarkably successful: not only the central functions for which the model was produced are in excellent agreement with the experimental evidence, but the same is true also for every subsequent and fortuitous detail following from them, such as the suppression of flavour-changing neutral currents, proton stability and a multitude of other precision electroweak observables[1] [2].

The Higgs boson is the last addition to the picture. It was discovered in 2012 by the ATLAS and CMS experiments at the Large Hadron Collider with a mass of $m_H = 125$ GeV/c^2 [3] [4]. It differs from all the other fundamental particles: while all fermions are $^1/_2$-spin particle and all bosons are 1-spin particle, the Higgs is the only 0-spin scalar boson (see fig. 1.1). Moreover, the origin of the mass of the fundamental particles is understood in the context of the Higgs mechanism: while the fields associated to all the other fundamental particles have zero expectation value in vacuum, this is not true for the Higgs field: as a consequence, the fundamental particles interacting with the Higgs field acquire mass [1].

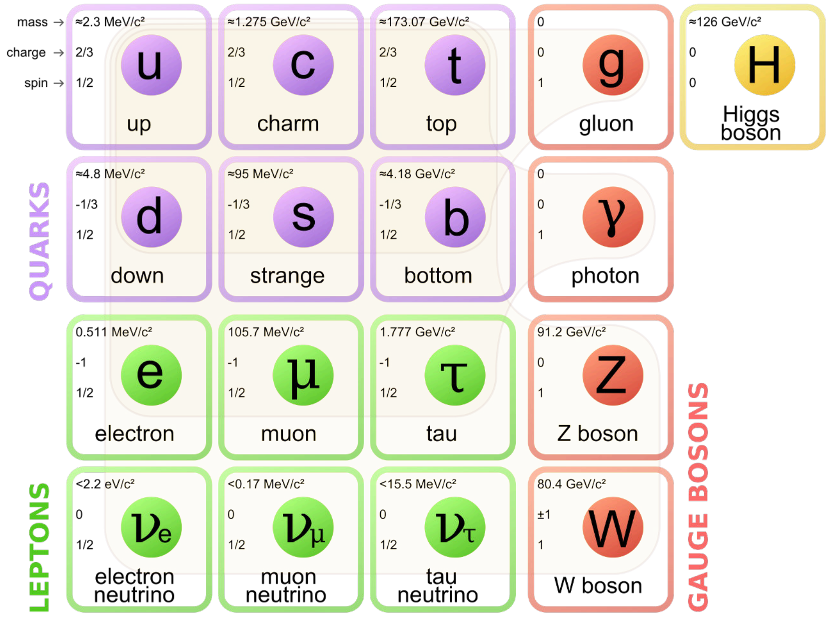

Figure 1.1: A schematic representation of the fundamental particles in the Standard Model, along with their mass, electric charge and spin.

Whilst the outstanding success of the Standard Model in high energy physics is undisputable, many measurements coming from related fields of physics seems to be in stark contrast with some of the most fundamental features of the model:

- the SM lacks a mechanism by which the neutrinos acquire a mass and, as a result, these particle are supposed to have no mass according to the model. However the discovery of flavour oscillations in the neutrino sector implies non-zero masses for these particles [5];

- no fundamental particle in the SM has all the properties needed to explain the effects of the cold dark matter, a kind of matter which does not interact electromagnetically and whose existence is deduced only from its gravitational effects. The most notable evidences hinting to the existence of this kind of matter include the observations in gravitational lensing, the cosmic microwave background, the mass location in galactic collisions and the anomalous galaxy rotation curves [6];

- the observed baryon asymmetry can't be explained in the SM, according to which equal amounts of baryons and anti-baryons were produced right after the Big Bang. Although the SM predicts a small baryon/antibaryon asymmetry coming from the CP-violation induced by the complex phase in the CKM matrix, the effect is definitely too small to be consistent with the observations [7][8];

- a quantum description of gravity does not exists at the moment. As a matter of fact, we still lack a quantum field theory of gravity since the general theory of relativity can't be easily harmonized with quantum mechanics. This is usually not considered a problem in experimental particle physics, since gravity is several orders of magnitude weaker than the other forces and has negligible effects; nevertheless it highlights an important problem in our fundamental understanding of Nature [9].

For all these reasons, and many others, physics beyond the Standard Model is expected to be found. Many different models have been proposed during the years, involving new exotic particles, extra-dimensions, an internal structure for elementary particles, and so on. NA62 will be able to give a contribution to discriminating between some of these models, while also performing precision measurement of SM processes.

Indeed, besides the measurement of the branching ratio of $K^+ \to \pi^+ \nu\bar{\nu}$ and other precision SM measurements, NA62 can perform direct and indirect searches for light exotic particles, such as heavy neutral leptons (HNL), dark photons (DP) and axion-like particles (ALP), and investigate lepton number and lepton flavour universality violation (LNV/LFV). Some of these searches have already brought results improving the state of the art, like in the case of HNL [10], DP [11] and LNV/LFV [12], while other searches (such as those on ALPs) will require further data taking in a particular setup in the future [13].

1.2 The CKM matrix

The six quarks of the SM are grouped into three generations, each consisting of a doublet that has an up-type quark with electrical charge $+2/3$ and a down-type quark with electrical charge $-1/3$. The transition of a quark of a certain flavour to a quark of another flavour happens through charged weak interactions mediated by $W^{\pm}$ bosons. This transition is described in the Standard Model by the Cabibbo-Kobayashi-Maskawa (CKM) matrix. This unitary matrix connects the weak eigenstates to the mass eigenstates of quarks in the following way [8]:

$$\begin{pmatrix} d' \\ s' \\ b' \end{pmatrix} = \begin{pmatrix} V_{ud} & V_{us} & V_{ub} \\ V_{cd} & V_{cs} & V_{cb} \\ V_{td} & V_{ts} & V_{tb} \end{pmatrix} \begin{pmatrix} d \\ s \\ b \end{pmatrix} . \tag{1.1}$$

Therefore weak charged current vertices can be written as

$$-i\frac{g_W}{\sqrt{2}}(\bar{u},\ \bar{c},\ \bar{t})\gamma^\mu \frac{1}{2}(1-\gamma^5) \begin{pmatrix} V_{ud} & V_{us} & V_{ub} \\ V_{cd} & V_{cs} & V_{cb} \\ V_{td} & V_{ts} & V_{tb} \end{pmatrix} \begin{pmatrix} d \\ s \\ b \end{pmatrix} . \tag{1.2}$$

The CKM matrix elements can be written in terms of three rotation angles and a complex phase:

$$V_{\mathrm{CKM}} = \begin{pmatrix} 1 & 0 & 0 \\ 0 & c_{23} & s_{23} \\ 0 & -s_{23} & c_{23} \end{pmatrix} \times \begin{pmatrix} c_{13} & 0 & s_{13}e^{-i\delta} \\ 0 & 1 & 0 \\ -s_{13}e^{i\delta} & 0 & c_{13} \end{pmatrix} \times \begin{pmatrix} c_{12} & s_{12} & 0 \\ -s_{12} & c_{12} & 0 \\ 0 & 0 & 1 \end{pmatrix} , \tag{1.3}$$

where $s_{ij} = sin\theta_{ij}$, $c_{ij} = cos\theta_{ij}$ and δ is the phase responsible for the CP violation in the SM, while θ_{ij} is the mixing angle between i and j quark families [8].

Because of the structure of the neutral current, flavour changing neutral current processes do not take place at tree level, and they are strongly suppressed at one-loop. This suppression at one-loop level is due to the Glashow-Iliopoulos-Maiani (GIM) mechanism [5]. As an example, consider the decay $K^+ \to \pi^+\nu\bar{\nu}$. If one considers the matrix connecting the mass and the weak eigenstates of d and s quarks, limiting ourselves to only two flavours, this matrix elements can be approximated using the Cabibbo angle:

$$\begin{pmatrix} d' \\ s' \end{pmatrix} = \begin{pmatrix} \cos\theta_C & \sin\theta_C \\ -\sin\theta_C & \cos\theta_C \end{pmatrix} \begin{pmatrix} d \\ s \end{pmatrix} . \tag{1.4}$$

Therefore, the relevant two terms describing neutral current transitions in the Lagrangian are

$$\bar{d}'\gamma_\alpha d' = \cos^2\theta_C \bar{d}\gamma_\alpha d + \sin^2\theta_C \bar{s}\gamma_\alpha s + \cos\theta_C \sin\theta_C [\bar{d}\gamma_\alpha s + \bar{s}\gamma_\alpha d] \tag{1.5}$$

$$\bar{s}'\gamma_\alpha s' = \sin^2\theta_C \bar{d}\gamma_\alpha d + \cos^2\theta_C \bar{s}\gamma_\alpha s - \cos\theta_C \sin\theta_C [\bar{d}\gamma_\alpha s + \bar{s}\gamma_\alpha d] \tag{1.6}$$

and adding up eq. 1.5 and 1.6,

$$\bar{d}'\gamma_\alpha d' + \bar{s}'\gamma_\alpha s' = \bar{d}\gamma_\alpha d + \bar{s}\gamma_\alpha s \ , \tag{1.7}$$

the terms describing FCNC that were present in eq. 1.5 and 1.6 cancel out. Actually this cancellation is not perfect, since one has to consider higher order corrections making possible FCNC at second order.

Another parametrization can be used to express the elements of the CMK matrix. This parametrization was introduced by Wolfenstein [14] and makes use of four real parameters λ, A, ρ and η, related to the previous ones in the following way:

$$s_{12} = \lambda, \qquad s_{23} = A\lambda^2, \qquad s_{13}e^{i\delta} = A\lambda^3(\rho + i\eta) \tag{1.8}$$

$$\bar{\rho} = \rho(1 - \frac{\lambda^2}{2}), \qquad \bar{\eta} = \eta(1 - \frac{\lambda^2}{2}) \ . \tag{1.9}$$

Using the Wolfenstein parametrization, the matrix can be expanded in terms of the small parameter $\lambda = 0.225$:

$$V_{CKM} = \begin{pmatrix} 1 - \frac{\lambda^2}{2} & \lambda & A\lambda^3(\rho - i\eta) \\ -\lambda & 1 - \frac{\lambda^2}{2} & A\lambda^2 \\ A\lambda^3(1 - \rho - i\eta) & -A\lambda^2 & 1 \end{pmatrix} + O(\lambda^4) \ . \tag{1.10}$$

As it is evident from eq. 1.10, the most favoured quark transitions are those corresponding to the diagonal matrix elements, while off-diagonal elements represent suppressed transitions. As of 2018, the measured values of the matrix elements are [1]:

$$\begin{pmatrix} |V_{ud}| = 0.97420 \pm 0.00021 & |V_{us}| = 0.2243 \pm 0.0005 & |V_{ub}| = 0.00349 \pm 0.00036 \\ |V_{cd}| = 0.218 \pm 0.004 & |V_{cs}| = 0.997 \pm 0.017 & |V_{cb}| = 0.0422 \pm 0.0008 \\ |V_{td}| = 0.0081 \pm 0.0005 & |V_{ts}| = 0.0349 \pm 0.0023 & |V_{tb}| = 1.019 \pm 0.025 \end{pmatrix} \tag{1.11}$$

It is worth noticing that according to the Wolfenstein parametrization, $\lambda = |V_{us}|$.

1.3 The unitary triangle

The unitarity condition for the CMK matrix implies various relations between the matrix elements such as:

$$V_{us}^* V_{ud} + V_{cs}^* V_{cd} + V_{ts}^* V_{td} \ . \tag{1.12}$$

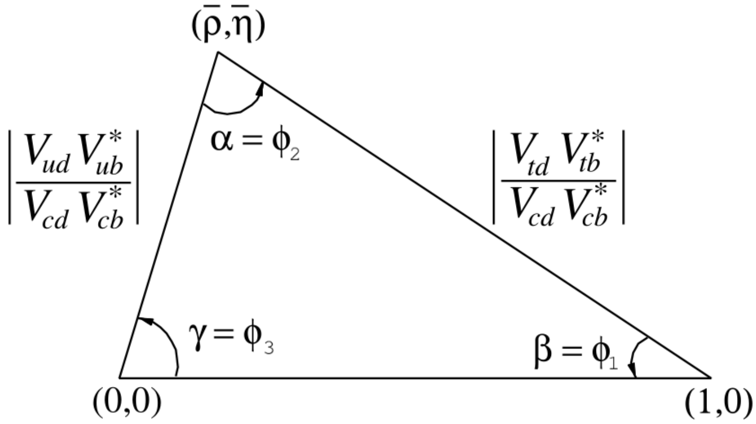

Figure 1.2: One of the unitary triangles defined by the unitarity conditions on the CKM matrix, namely by eq. 1.12. The sides and angles of the triangle are directly related to the value of the matrix elements.

Eq. 1.12 represents a triangle in the complex plane defined by the two Wolfenstein parameters (ρ, η). The triangle is shown in fig. 1.2, where $\bar{\rho}$ and $\bar{\eta}$ are

$$\bar{\rho} = \rho\left(1 - \frac{\lambda^2}{2}\right) \tag{1.13}$$

$$\bar{\eta} = \eta\left(1 - \frac{\lambda^2}{2}\right) , \tag{1.14}$$

while the angles of the triangle are:

$$\alpha = \arg\left(-\frac{V_{td}V_{tb}^*}{V_{ud}V_{ub}}\right), \quad \beta = \arg\left(-\frac{V_{cd}V_{cb}^*}{V_{td}V_{tb}}\right), \quad \gamma = \arg\left(-\frac{V_{ud}V_{ub}^*}{V_{cd}V_{cb}}\right) \tag{1.15}$$

1.4 The $K^+ \to \pi^+\nu\bar{\nu}$ decay

The values of the branching ratios of $K^+ \to \pi^+\nu\bar{\nu}$ and $K_L \to \pi^0\nu\bar{\nu}$ provide an extremely interesting test of the Standard Model [15]. Both processes are *flavour changing neutral current* (FCNC), strongly suppressed by the GIM mechanism. The charged version of the decay proceeds at the lowest level via the two Z penguin diagrams and the W box shown in fig. 1.3.

Theoretically this process is very clean and the main sources of uncertainty originate from the uncertainties on the CKM matrix elements [15]; in particular, the formula for the branching ratio of $K^+ \to \pi^+ \nu\bar{\nu}$ can be written as follows

$$BR(K^+ \to \pi^+ \nu\bar{\nu}) = \kappa_+ (1 + \Delta_{\rm EM}) \cdot \left[\left(\frac{{\rm Im}\lambda_t}{\lambda^5} X(x_t) \right)^2 + \left(\frac{{\rm Re}\lambda_c}{\lambda} (P_c^{\rm SD}(X) + \delta P_{c,u}) + \frac{{\rm Re}\lambda_t}{\lambda^5} X(x_t) \right)^2 \right] , \quad (1.16)$$

where

$$\kappa_+ = (5.173 \pm 0.025) \cdot 10^{-11} \left[\frac{\lambda}{0.225} \right]^8 , \qquad \Delta_{\rm EM} = -0.003 \; . \quad (1.17)$$

κ_+ is the hadronic matrix element extracted from semi-leptonic decays of K^+, K_S and K_L; $\Delta_{\rm EM}$ is the electromagnetic radiative correction from photon exchanges; $x_t = m_t^2/M_W^2$, $\lambda = |V_{us}|$ and $\lambda_i = V_{is}^* V_{id}$ are CKM factors; $X(x_t)$ represents the loop function for the top quark contribution; $P_c^{\rm SD}(X)$ and $\delta P_{c,u}$ are the loop functions for the short distance charm quark and long distance charm and up quark contributions. The top quark contribution is $X(x_t) = 1.48 \pm 0.01$ and includes the two-loop electroweak corrections and NLO QCD corrections; the short distance contribution for charm quark and long distance contribution for charm and up quark are, respectively, $P_c^{\rm SD}(X) = 0.365 \pm 0.012$ and $\delta P_{c,u} = 0.04 \pm 0.02$ and include electroweak and NNLO QCD corrections. The apparent dependence of the branching ratio on λ actually cancels out to a large extent since $P_c(X) \sim \lambda^{-4}$.

Since New Physics seems to be distant enough from the electroweak scale, the CKM matrix can be determined using tree-level measurements of the observables $|V_{us}|$, $|V_{cb}|$, $|V_{ub}|$ and γ, where γ is one of the angles of the unitary triangle. Therefore the quantities λ_t and λ_c can be expressed using only these input parameters:

$$\mathrm{Re}\lambda_t \simeq |V_{ub}||V_{cb}| \cos\gamma (1 - 2\lambda^2) + (|V_{ub}|^2 - |V_{cb}|^2)\lambda \left(1 - \frac{\lambda^2}{2} \right) , \quad (1.18)$$

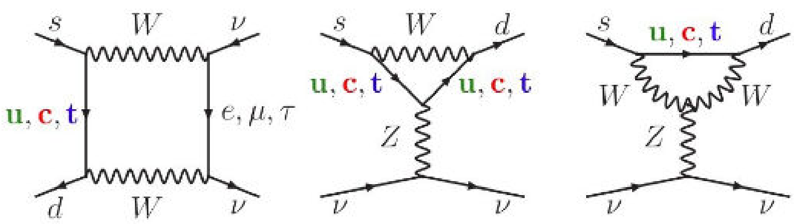

Figure 1.3: The three most relevant diagrams for the $K^+ \to \pi^+ \nu\bar{\nu}$ decay. The $s \to d$ transition, forbidden at the three level, is dominated by two Z penguins and a W box diagrams.

$$\text{Im}\lambda_t \simeq |V_{ub}||V_{cb}| \sin\gamma \ , \tag{1.19}$$

$$\text{Re}\lambda_c \simeq -\lambda \left(1 - \frac{\lambda^2}{2}\right) \ , \tag{1.20}$$

accurate up to $O(\lambda^4)$. For the calculation, the values of $\gamma = (73.2^{+6.3}_{-7.0})^\circ$ and $\lambda = |V_{us}|$ are taken from the PDG [1], while for $|V_{ub}|$ and $|V_{cb}|$ a weighted average between the exclusive and inclusive determination is used:

$$|V_{ub}|_{avg} = (3.88 \pm 0.29) \times 10^{-3} \qquad |V_{cb}|_{avg} = (40.7 \pm 1.4) \times 10^{-3} \ . \tag{1.21}$$

These last expressions can be plugged into 1.16 to determine the expected theoretical value for the branching ratio:

$$BR_{th}(K^+ \to \pi^+ \nu\bar{\nu}) = (8.4 \pm 1.0) \times 10^{-11} \ . \tag{1.22}$$

A similar calculation for the neutral counterpart $K_L \to \pi^0 \nu\bar{\nu}$ can be found in [15] and leads to

$$BR_{th}(K_L \to \pi^0 \nu\bar{\nu}) = (3.4 \pm 0.6) \times 10^{-11} \ . \tag{1.23}$$

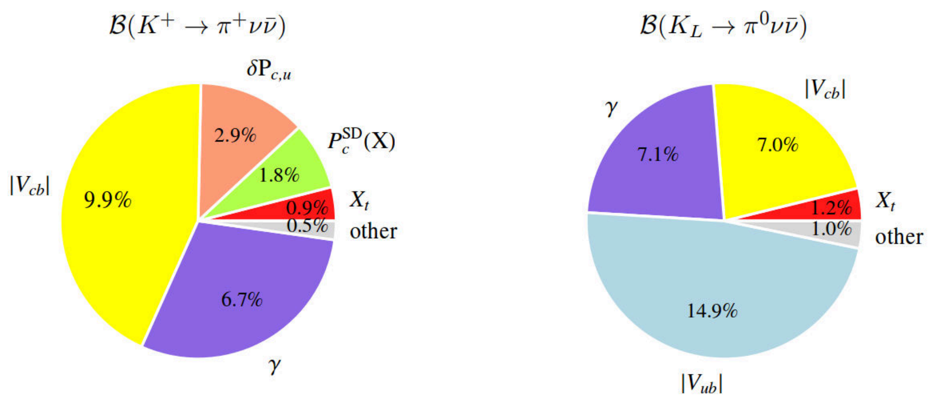

Figure 1.4: Error budgets for the branching ratio of $K^+ \to \pi^+\nu\bar{\nu}$ and $K_L \to \pi^0\nu\bar{\nu}$.

Figure 1.4 shows the error budgets for the two branching ratios. The CKM uncertainties dominate the error in both cases and, in particular, the largest contributions to the error come from $|V_{cb}|$ and γ for the charged channel, while for the neutral channel there is also an important contribution from $|V_{ub}|$. Therefore it may be convenient to have an expression for the branching ratios where the theoretical and the parametric uncertainties are kept separate:

$$BR(K^+ \to \pi^+\nu\bar{\nu}) = (8.39 \pm 0.30) \times 10^{-11} \cdot \left[\frac{|V_{cb}|}{0.0407}\right]^{2.8} \cdot \left[\frac{\gamma}{73.2^o}\right]^{0.74} \ , \tag{1.24}$$

$$BR(K_L \to \pi^0 \nu\bar{\nu}) = (3.36 \pm 0.05) \times 10^{-11} \cdot \left[\frac{|V_{ub}|}{3.88 \times 10^{-3}}\right]^2 \cdot \left[\frac{|V_{cb}|}{0.0407}\right]^2 \cdot \left[\frac{\sin\gamma}{\sin 73.2^{\text{o}}}\right]^2 . \quad (1.25)$$

The state of the art on the measurement of the branching ratios of the two K decays is shown below:

$$BR_{\text{exp}}(K^+ \to \pi^+ \nu\bar{\nu}) = (1.73^{+1.15}_{-1.05} \times 10^{-10}) \quad (1.26)$$

$$BR_{\text{exp}}(K_L \to \pi^0 \nu\bar{\nu}) < 300 \times 10^{-11} \text{ @90\% C.L.} \quad (1.27)$$

The measurement of the BR in eq. 1.26 was performed by the E787/949 experiments at BNL and it is based on the observation of 7 decays of stopped K^+ interpreted as signal [16]. The upper limit in eq. 1.27 was put by the KOTO experiment, based on the analysis of 2015 data; this result is expected to be improved with the analysis of the full data sample [17].

NA62 published recently its results on the $K^+ \to \pi^+ \nu\bar{\nu}$ analysis with the 2016 data set; the results and a description of the analysis can be found in [18]. With a number of expected SM events of $0.267 \pm 0.001_{stat} \pm 0.020_{syst} \pm 0.032_{ext}$, an expected background of $0.152^{+0.092}_{-0.033}|_{stat} \pm 0.013_{syst}$ and 1 observed event in the signal region, NA62 was able to put an upper limit on the branching ratio of the decay:

$$BR(K^+ \to \pi^+ \nu\bar{\nu}) < 14 \times 10^{-10} \text{ at 95\% CL.} \quad (1.28)$$

This result has improved with the 2017 data set, on which this thesis will focus, and will be further improved with the analysis of the 2018 data set.

1.5 Beyond the Standard Model

The measurement of $BR(K^+ \to \pi^+ \nu\bar{\nu})$ and $BR(K_L \to \pi^0 \nu\bar{\nu})$ defines the unitarity triangle independently of the B system, thus being an important test for the SM itself independently of any new physics model (fig. 1.7). Indeed, the unitary triangle defined by equation 1.12 is tightly linked to the two aforementioned decays: the branching ratio of $K_L \to \pi^0 \nu\bar{\nu}$ provides the height of the triangle, while $K^+ \to \pi^+ \nu\bar{\nu}$ provides the measurement of one side of the triangle (see fig. 1.5).

Nonetheless, a plethora of models beyond the Standard Model predict sizable differences in the value of the branching ratio of these two decays. This models comprise custodial Randall-Sundrum [19], Minimal Supersymmetric Standard Model (MSSM) Analysis [20][21], simplified Z, Z' models [22], littlest Higgs with T-parity [23] and lepton flavour universality violation

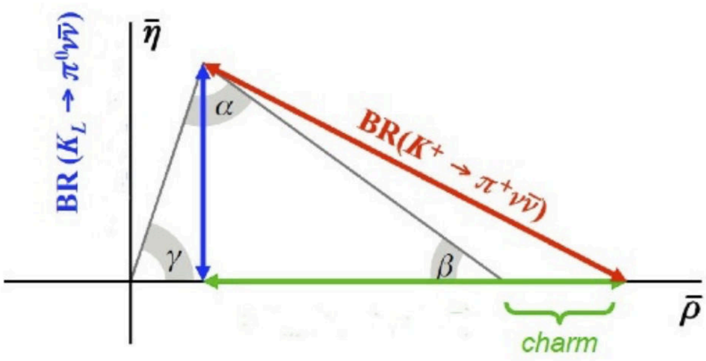

Figure 1.5: The relation between the sides of the unitary triangle and the two decays $K^+ \to \pi^+\nu\bar{\nu}$ and $K_L \to \pi^0\nu\bar{\nu}$.

models [24]. The importance of performing a precision measurement in this context is better understood looking at the plot in fig. 1.6, where one can see the different correlation patterns between $K^+ \to \pi^+\nu\bar{\nu}$ and $K_L \to \pi^0\nu\bar{\nu}$ for different BSM scenarios; the plot shows also the Grossman-Nir bound [25], that is model independent and it can be derived just assuming the lepton flavour conservation[1]. In the following, a brief description of NP models mentioned above for which the $K^+ \to \pi^+\nu\bar{\nu}$ decay is relevant will be given.

The **Randall-Sundrum** model (RS) [19] is a higher-dimensional mechanism that solves the hierarchy problem by postulating that a large scale (of the order of the Planck scale) produces the weak scale through an exponential hierarchy; in the RS model the hierarchy arises from warped higher-dimensional space-time, where only one additional dimension is required [2]. In this context, rare K and B meson decays (such as $K^+ \to \pi^+\nu\bar{\nu}$, $K_L \to \pi^0\nu\bar{\nu}$, $K_L \to \pi^0 l^+ l^-$, $K_L \to \mu^+\mu^-$, $B_{s,d} \to \mu^+\mu^-$ and $B \to K(*)\nu\bar{\nu}$) receive tree level contributions from the Z and the new heavy electroweak gauge bosons, besides the usual SM one-loop contributions. Specifically, the branching ratio of kaon decays can have large differences with respect to the SM, while the effects in the B decays are smaller.

In the **Minimal Supersymmetric Standard Model** (MSSM) the SM Lagrangian is extended by supersymmetric terms that typically bring new sources of flavour violation. The FCNC amplitudes depend on the sparticle masses and the pattern of their mixing, and important contribution to the $K^+ \to \pi^+\nu\bar{\nu}$ decay amplitude can arise from the squark mass matrices [20]. The branching ratios of $K \to \pi\nu\nu$ decays are indeed very useful to determine the flavour structure of the model. In particular, under certain hypothesis,

[1]Specifically, $\Gamma(K_L \to \pi^0\nu\bar{\nu})/\Gamma(K^+ \to \pi^+\nu\bar{\nu}) = \sin^2\theta$, where θ is the relative CP violating phase between the $K - \bar{K}$ mixing amplitude and the $s \to d\nu\bar{\nu}$ decay amplitude.

the two branching ratios for $K \to \pi\nu\nu$ decays could receive $O(1)$ corrections with respect to SM [21].

A correlation between $K^+ \to \pi^+\nu\bar{\nu}$ and $B \to K(K*)\mu^+\mu^-$ can arise in **models with tree level Z and Z' contributions** in which either Minimal Flavour Violation (MFV) or a $U(2)^3$ symmetry is imposed on the quark flavour-violating couplings [22]. In this case, $K^+ \to \pi^+\nu\bar{\nu}$ and $K_L \to \pi^0\nu\bar{\nu}$ can probe energy scales up to 1000 TeV and Z and Z' models with general flavour couplings allow for $BR(K^+ \to \pi^+\nu\bar{\nu}) > 20 \times 10^{-11}$.

The **Littlest Higgs Model with T-parity** (LHT) is one of the simplest New Physics models that can account for new sources of flavour and CP violation [23]. In this scenario, the branching ratios of $K^+ \to \pi^+\nu\bar{\nu}$ and $K_L \to \pi^0\nu\bar{\nu}$ can have significant differences with respect to the SM predictions, while the effect on B meson decays are smaller. The LHT model predicts new heavy fermions that can interact with the ordinary quarks and leptons through new heavy electroweak gauge bosons. The Littlest Higgs model without T-parity was first introduced to deal with the quadratic divergences in the Higgs mass without having to resort to supersymmetry, so that the cancellation of the divergences happens with the intervention of new particles of the same spin-statistics. However, a discrete symmetry (the T-parity, under which all SM particles are even) has to be introduced in order to make the Littlest Higgs model consistent with electroweak precision tests and, at the same time, make the new particles of this model in the reach of the LHC. The LHT produces correlation patterns between the branching ratios of $K^+ \to \pi^+\nu\bar{\nu}$ and $K_L \to \pi^0\nu\bar{\nu}$ and, in particular, $BR(K^+ \to \pi^+\nu\bar{\nu})$ can reach values of the order of $20 \cdot 10^{-11}$. If no new particle is discovered at LHC, no deviation from the SM is observed in electroweak and Higgs physics measurements and the New Physics happens to be at a scale of several TeV, $K \to \pi\nu\nu$ decays become the best candidate to prove the LHT model; if that is the case, the branching ratio of $K^+ \to \pi^+\nu\bar{\nu}$ could be enhanced by up to a factor 2.

Recent hints of **violation of Lepton Flavour Universality** (LFU) in B meson decays may be easily accommodated in models where new interactions responsible for these violations couple mainly to the third generation of left-handed fermions [24]. For this reason, $K \to \pi\nu\nu$ decays are particularly interesting because they are the only kaon decays with third-generation leptons[2] in the final state. In order to relate B physics anomalies and K decays, an Effective Field Theory approach can be used, where the new interactions satisfy an approximate $U(2)_q \times U(2)_l$ flavour symmetry. It turns out that in this case the models predict $O(1)$ deviations from the SM value

[2]The tau neutrinos.

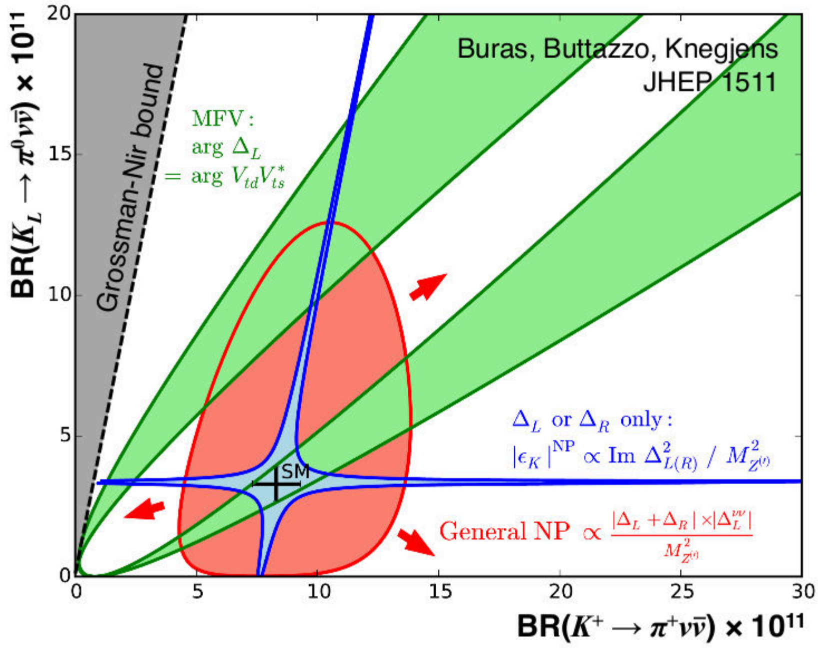

Figure 1.6: Correlation between the branching ratios of $K^+ \to \pi^+\nu\bar{\nu}$ and $K_L \to \pi^0\nu\bar{\nu}$. The green region shows the correlation emerging in models with constrained minimal flavour violation. The blue region shows the correlation arising from ε_K constraints when LH or RH couplings are present. Conversely, the red region shows the lack of correlation in models with general LH and RH couplings.

of $BR(K \to \pi\nu\nu)$.

In conclusion, kaon rare decays are of paramount importance in many New Physics scenarios. Even in the event of the discovery of New Physics at the TeV scale by direct searches at the LHC, these analyses are unlikely to determine the structure of the new theory; for this purpose precision experiments such as NA62 are fundamental [21].

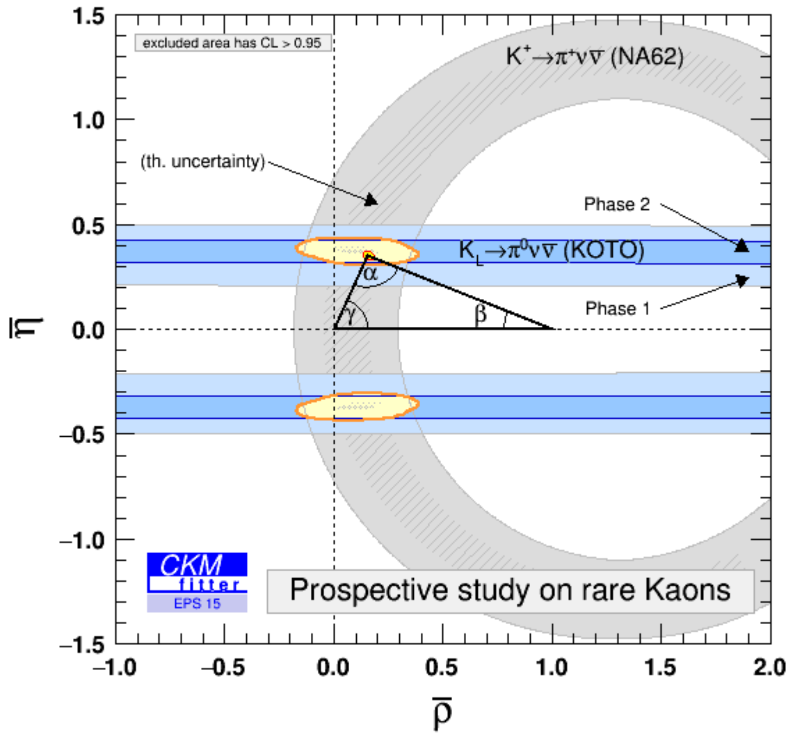

Figure 1.7: Expected constraints on the unitary triangle from the measurements on $K^+ \to \pi^+ \nu \bar{\nu}$ (NA62) and $K_L \to \pi^0 \nu \bar{\nu}$ (KOTO). For NA62 a 10% accuracy is assumed, where the dashed region corresponds to the theoretically contribution to the uncertainty; for KOTO, a 3σ evidence is assumed for Phase 1 (lighter blue) and a 10% accuracy for Phase 2 (darker blue) [26][27].

Chapter 2

The NA62 experiment

The experimental strategy for the measurement of $K^+ \to \pi^+\nu\bar{\nu}$ at NA62 is illustrated in section 2.1. A brief description of the accelerator complex is given in section 2.2; the primary and secondary beam characteristics and the beam line are described in section 2.3, while the NA62 detector is described in detail in 2.4.

2.1 Experimental strategy

NA62 exploits a decay-in-flight technique, letting the kaons decay in flight along the detector. This allows to have a significant flux of kaons ($O(10^{13})$ over a few years of data taking) and better measurements on the decay products [28]. In the decay-in-flight technique, the exploitation of a high energy hadron beam boosts the decay products into a small angular region, enabling to use a fixed target experiment geometry; moreover the decay products are boosted to high energies, ensuring a more efficient detection and particle identification. On the other hand, because of the huge beam intensity, the beam tracker measuring the momentum of the beam particles require particular care (see 2.4.2), and so does the trigger and the data acquisition system (section 2.4.11).

Since the two neutrinos in the final state of $K^+ \to \pi^+\nu\bar{\nu}$ cannot be seen by the detector, the only information about the decay comes from accurate measurements on the upstream track (the K^+) in the initial state and the downstream track (the π^+) in the final state. The main variable used in the analysis for the kinematic rejection of the background K decays is the *squared missing mass*, m^2_{miss}, i.e. the square of the difference between the K^+ and the π^+ 4-momenta,

$$m^2_{\text{miss}} = (P_K - P_\pi)^2 \ . \tag{2.1}$$

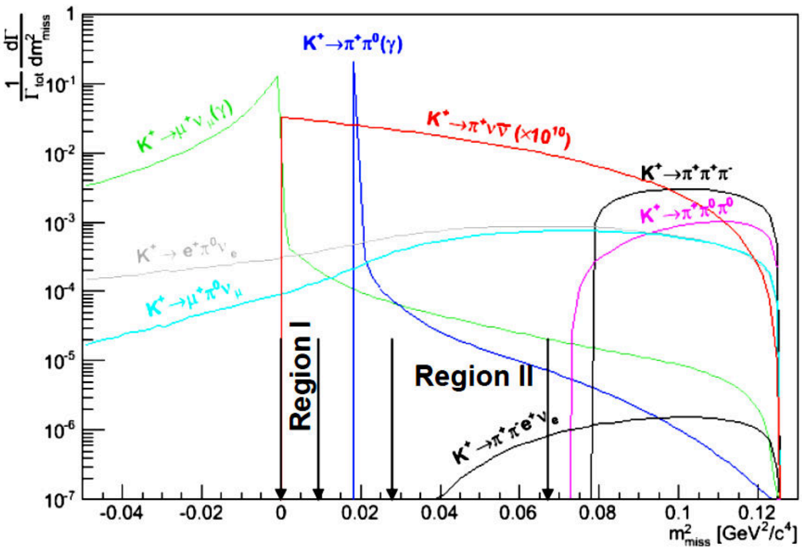

Figure 2.1: Squared missing mass distribution for the signal and the background K^+ decays. The signal is shown in red and is enhanced by a factor 10^{10} in the plot. The two chosen signal regions are delimited by black arrows.

The distributions of the squared missing mass for the signal and the main background kaon decays are shown in fig. 2.1. Two signal regions can be defined, in order to avoid the sharp peak of the $K^+ \to \pi^+\pi^0$ that happens to be right in the middle of the m^2_{miss} distribution for the signal process.

2.2 The CERN accelerator complex

At present, the CERN Large Hadron Collider (LHC) is the most powerful collider in the world, with unprecedented center of mass energies. Four main experiments (ATLAS, CMS, LHCb and ALICE) are located at the interaction points, where proton beams collide producing all kinds of particles. The Super Proton Synchrotron (SPS, the last step in the acceleration system before the LHC), provides the proton beam needed by the NA62 experiment in order to produce its secondary hadron beam.

A scheme of the accelerator complex is shown in fig. 2.2 [29]. The protons are initially extracted from a hydrogen gas thanks to the Duoplasmatron where electrons are stripped off the gas by an electrical field. The particles are then accelerated by a linear accelerator, the LINAC2, that uses radio-frequency cavities to accelerate protons which, at that point, have reached an energy of 50 MeV. LINAC2 was stopped at the beginning of the Long

Shutdown 2 and will be permanently replaced by LINAC4 for future physics runs.

Once the protons pass through the LINAC2, they are sent to the Proton Synchrotron Booster (PSB), a circular accelerator with a 157 m circumference that accelerates them to 1.4 GeV and they are subsequently sent to the Proton Synchrotron (PS). The PS protons are accelerated to 25 GeV before being injected into the 7 km long ring of the Super Protons Synchrotron (SPS). The ring of the SPS is divided in sextants, where each sextant is made of two arcs and a Long Straight Section (LSS). The nominal intensity in the SPS is 1.2×10^{11} ppb[1] [29]. The protons accelerated in the SPS reach an energy of 450 GeV and, eventually, they are injected into the LHC. Another possibility for the SPS is to extract 400 GeV protons and send them to experiments in the North Area, such as NA62 [30][28].

The LHC is a 27 km long circular accelerator capable of accelerating protons to energies as high as 6.5 TeV per beam. The collider has four interactions points where the four main experiments are located and the energy of the collisions in the center of mass is 13 TeV. Besides protons, the LHC can provide heavy-ion beams, so that it is possible to have lead-lead, proton-lead or even xenon-xenon collisions [29].

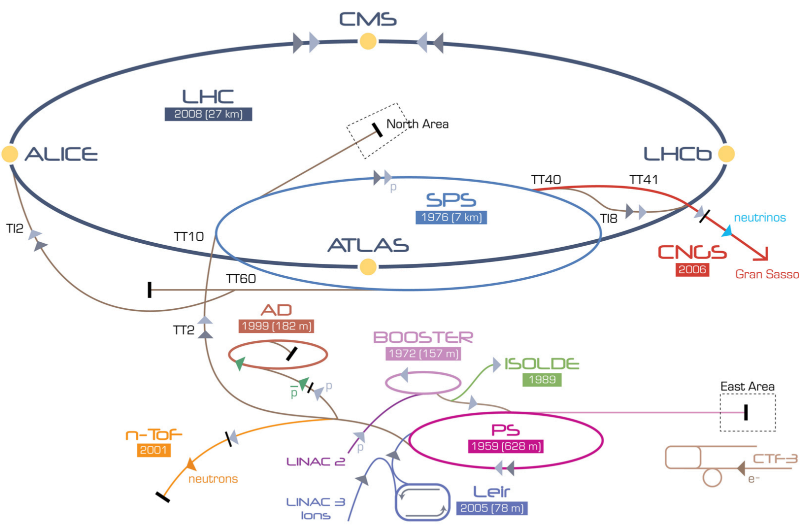

Figure 2.2: The CERN accelerator complex.

[1] protons per bunch

NA62 beam composition		
p	23%	173 MHz
K^+	6%	45 MHz
π^+	70%	525 MHz
μ^+	$< 1\%$	5 MHz
Total	100%	750 MHz

Table 2.1: Composition of the NA62 secondary beam.

2.3 The beam line

A 400 GeV/c slow extracted proton beam provided by the SPS is split into three branches and, subsequently, impinges on three different targets (T2, T4 and T6). Protons interacting with T4 make up two different beam lines, H6 and H8, while protons that do not interact with T4 are deviated to the P42 beam line. The P42 beam line transports this 400 GeV/c primary proton beam to the TCC8 underground tunnel where it interacts with the T10 beryllium target, producing a 75 GeV/c secondary charged hadron beam, containing about 6% K^+. The instantaneous beam intensity is 750 MHz. The composition of the secondary beam is reported in table 2.1. The K^+ momentum is 75 GeV/c, with a $\Delta p/p \sim 1.6\%$.

The beam line defines the Z axis of the experiment, with the origin at the beryllium target and the positive direction coinciding with the one of the traveling beam particles; the Y axis is aligned vertically and points up, while the horizontal X axis forms a right-handed coordinate system.

A 95 cm long copper collimator follows the T10 target, where the K12 beam line starts; a 15 mm hole in the collimator is usually selected to transmit the beam. A triplet of quadrupole magnets (Q1, Q2 and Q3) and an achromat (A1) select a beam with 75 GeV/c momentum and a large solid angle acceptance (± 2.7 mrad horizontally and ± 1.5 mrad vertically). The achromat is made of four dipole magnets, where the first two displace the beam of 11 cm downwards and the last two bring it back to the original direction: in between the two pairs of magnets, there are two copper collimator (TAX1 and TAX2) with holes of different sizes that allow the momentum selection and dump part of the unwanted particles (fig. 2.3). If necessary, the TAXes can be completely closed and the detector can run in *dump mode* to perform searches for exotic particles. Between TAX1 and TAX2, a radiator made of 5 mm thick tungsten foils degrades positron energies by bremsstrahlung to the point where they are easily rejected by the following beam elements, while minimizing the losses of hadrons due to scattering.

After the TAXes, a series of quadrupoles and collimators (Q4-10, C1-7) focus and select the beam further. The beam passes through a field-free bore in a dipole magnet (B3), crossing iron plates inserted in the poles of the magnet. The vertical magnetic field in the surrounding iron sweeps away off-axis muons of both signs. Two dipoles (TRIM1 and TRIM2) placed before and after B3 cancel the small deviation of the beam due to the stray-field in the bore.

The upstream tracking system of NA62 (GTK) consists of three stations of silicon pixel detectors (GTK1, GTK2 and GTK3) and the second achromat (A2) is located between GTK1 and GTK3. A steering magnet (TRIM5) at the level of GTK3 deflects the beam towards positive X, to compensate the subsequent effect of the Spectrometer magnet (MNP33) placed 95 m downstream keeping the beam in the beam pipe until the end of the apparatus.

The fiducial decay volume consists of the first 60 m of a 117 m long tank, at a pressure of $\sim 10^{-6}$ mbar, 102.4 m after the target. The tank is made of 19 cylindrical steel sections and hosts 11 LAV stations and the 4 STRAW chambers. At the end of the vacuum tank, a 2 mm thin aluminium window separates the vacuum from the neon gas contained inside the 17 m long RICH vessel. The flange around the hole at the center of the aluminium window is connected to a thin aluminium tube of 168 mm diameter that transports the beam in vacuum throughout the length of the detectors.

Finally, after the MUV3 detector, the beam receives a deflection towards negative X by the BEND magnet, leaving the SAC detector clear from the hadron beam (see also section 2.4.9); the beam reaches eventually the beam dump where it is completely absorbed (fig. 2.4).

2.4 The NA62 detector

The NA62 detector is located in the North Area of the SPS, in the underground caverns TCC8 and ECN3, where the NA48 detector [31] used to be. Indeed NA62 inherited a few sub-systems from NA48, such as the LKr calorimeter, the charged hodoscope and part of the muon veto.

Figure 2.5 shows a simple sketch of the experiment, starting from the target where the hadron beam is produced, moving to the upstream detectors (KTAG, GTK and CHANTI) in the TCC8 cavern, and ending with the downstream detectors after the fiducial decay volume (LAV, STRAW, RICH, CHOD, NewCHOD, HASC, LKr, MUV, IRC/SAC) in the ECN3 cavern. The full detector, occupying the full length of TCC8/ECN3, is approximately

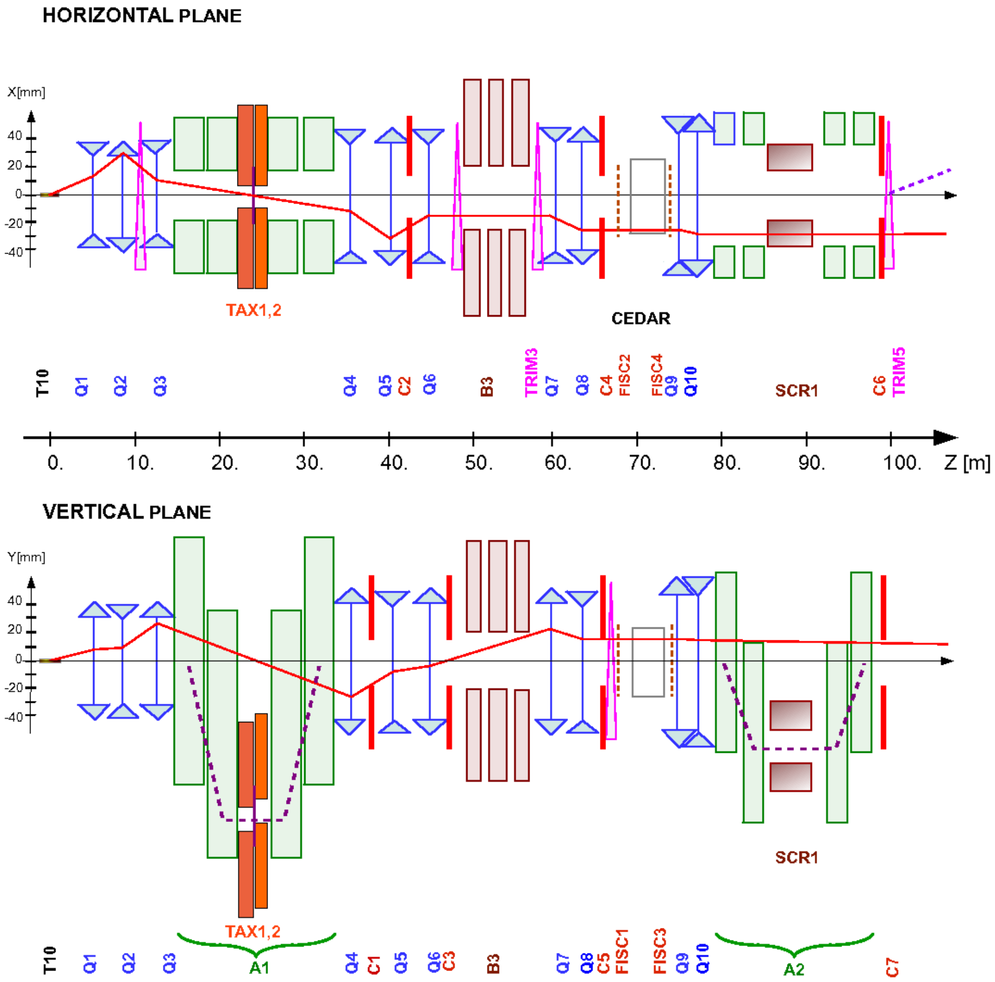

Figure 2.3: The K12 beam line, from the T10 target to the entrance of the fiducial decay volume. The solid line corresponds to the trajectory of a 75 GeV/c particle leaving the target from the center at the indicated angle. The dashed line shows the trajectory of a 75 GeV/c particle that is initially on-axis.

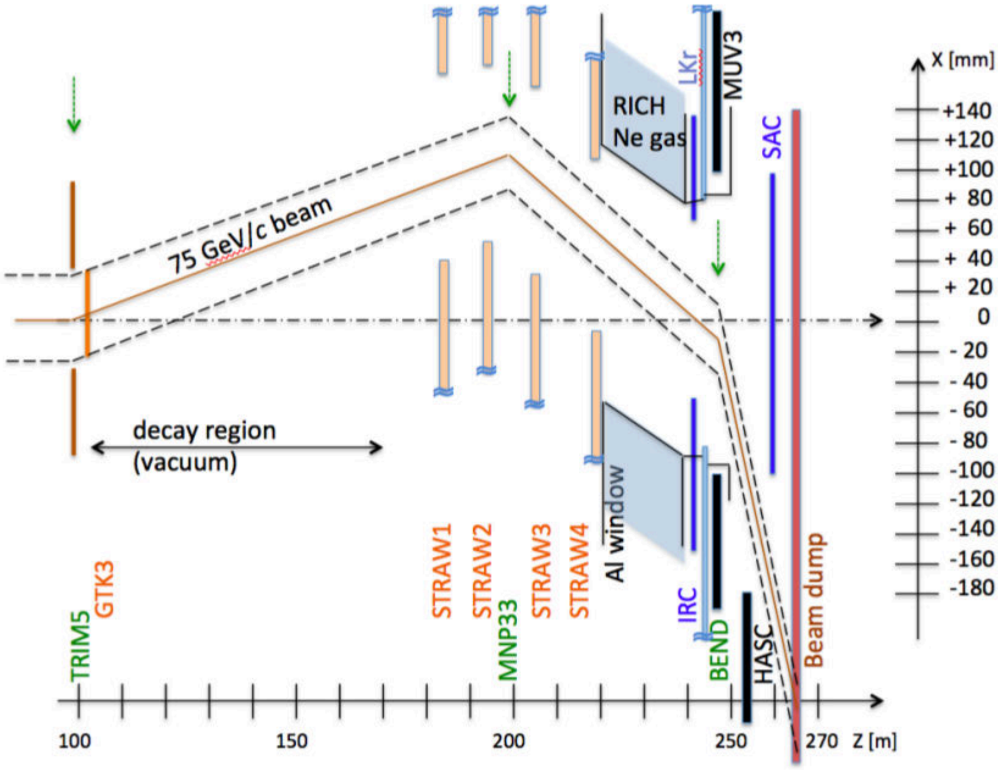

Figure 2.4: Beam line layout from the TRIM5 to the beam dump in the (X,Z) plane. The dashed lines represent the 2σ width of the beam profile. Initially, the beam has a $+1.2$ mrad angle towards positive X at the entrance of the decay region. At the STRAW spectrometer, the MNP33 magnet deflects the beam by -3.6 mrad in order to match the LKr central aperture. Then, after MUV3, the beam receives a final deflection by the BEND dipole magnet that kicks all the charged particles away from the SAC detector and into the beam dump.

250 m long. In the following, a short description of all the sub-systems of NA62 relevant for the $K^+ \to \pi^+ \nu\bar{\nu}$ analysis is given.

2.4.1 CEDAR/KTAG

As it has been described in section 2.3, the 750 MHz NA62 secondary beam contains just a 6% K^+, while the prevalent components are charged pions and protons. Therefore a fast and efficient kaon tagging sub-system is mandatory in order to identify the K^+ in the beam. This is required to have a 95% tagging efficiency, a pion mis-identification probability smaller than 10^{-4}, a time resolution better than 100 ps in order to minimize accidental coincidences with the downstream π^+, and the capability to sustain a 45 MHz K^+ rate.

This sub-system is the ChErenkov Differential counter with Achromatic Ring focus (CEDAR), based on the CERN West Area CEDAR built in the 70s and later updated in NA62 as the *KTAG* in order to meet the timing and rate requirements of the experiment. A schematic view of the sub-detector is shown in fig. 2.6. The CEDAR is a 7 m long tank filled with 1.1 m^3 of Nitrogen at 1.7 bar as a Cherenkov radiator. Because of the narrow momentum spread, a beam particle entering the CEDAR emits photons at a very specific angle which depends only on the particle mass. The photons are reflected by a mirror into 8 spots, each covered by 48 photomultipliers (PMT). The light passes through a chromatic corrector before reaching the PMTs. A ring shaped diaphragm with adjustable aperture (0 to 20 mm) is placed in front of the PMTs [32]. The choice of a differential counter is ideal because Cherenkov radiation generated by the passage of particles different from kaons will simply not reach the PMTs, so that the actual rate on the detector is 45 MHz and not the total 750 MHz of particles in the beam.

The measured kaon time resolution is $\sim$ 70 ps [32].

2.4.2 GigaTracker

The GigaTracker (GTK) is a silicon pixel beam tracker used to measure the momentum, direction and the spacial and time coordinates of the particles in the 75 GeV/c NA62 beam [33].

The GTK is made of three stations, GTK1, GTK2 and GTK3. Each station is made of 18000 time resolving pixels of 300×300 µm^2, covering an area of 60.8×27 mm^2. The three stations are installed in vacuum inside the beam pipe with two pairs of bending magnets as shown in fig. 2.7. The silicon sensors in the stations are read by two rows of five custom made ASICs. The

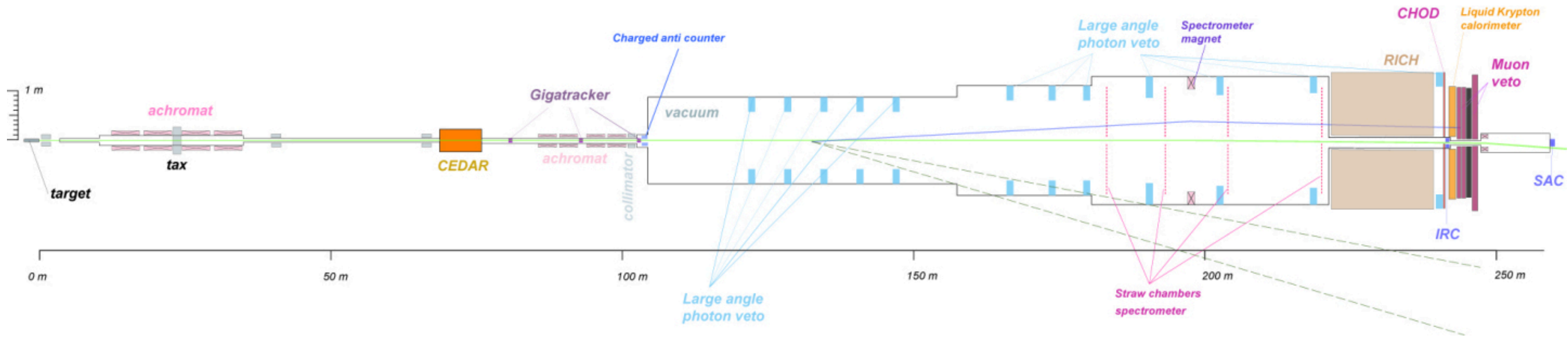

Figure 2.5: Layout of the NA62 detector.

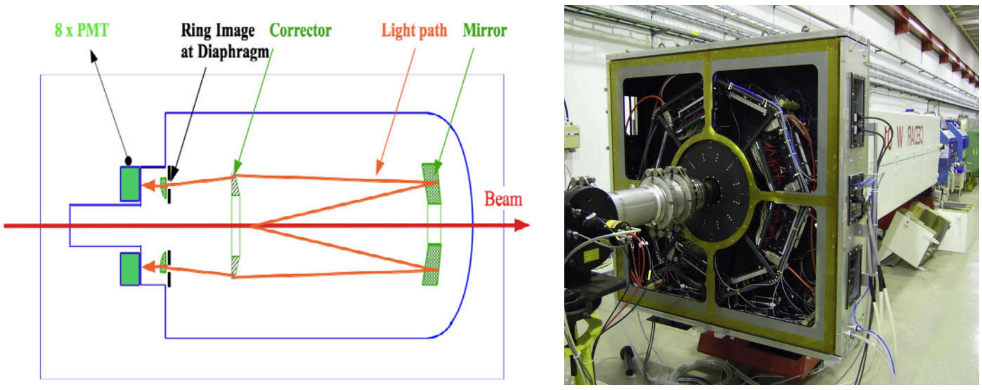

(a) (b)

Figure 2.6: Left: schematic view of the CERN West Area CEDAR. Right: picture of the NA62 CEDAR.

whole pixel detector plus the 10 chips is glued on a silicon plate used as a mechanical support and cooling plate.

The direction of the beam particle is obtained from the position at the first and the third GTK stations, while using also the position at GTK2 it is possible to evaluate the vertical displacement between the magnets which is related to the momentum rigidity. The momentum and direction of the beam particles are used to compute the squared missing mass (eq. 2.1).

In order to obtain the rejection needed for the $K^+ \to \pi^+ \nu \bar{\nu}$ measurement, the angular and momentum resolutions of the beam particle exiting the GTK need to be $\theta_{x,y} = p_{x,y}/p_z = 16$ µrad and $\delta p/p = 0.2\%$. The time resolution measured for the track is 75 ps.

The three stations constructed and used for the first data taking in 2016 had a thickness of 380 µm for GTK1 and GTK2, and 280 µm for GTK3. Consequently the material budget in the acceptance is $0.73\% X_0$ for the first two stations and $0.62\% X_0$ for the third one. The same three stations were used for the 2017 data taking, when the beam intensity rose from the 35% of the nominal one that was present in 2016 to 60-65% (depending on the data taking period).

2.4.3 CHANTI

A possible source of background for the $K^+ \to \pi^+ \nu \bar{\nu}$ measurement comes from beam particles impacting the GTK3 station producing a positively charged pion, which is detected by the NA62 subsystems in a way that the origin is wrongly reconstructed inside the fiducial volume, mimicking a sig-

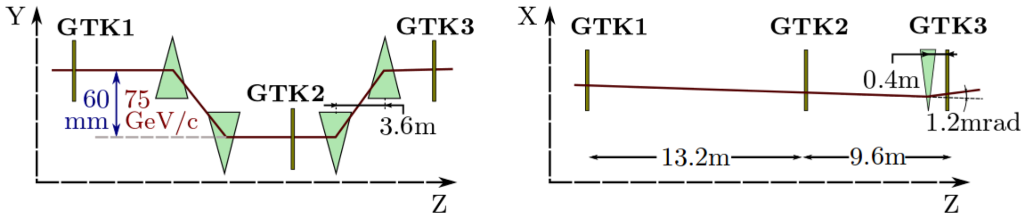

Figure 2.7: Schematic view of the GTK. The green triangles represent the bending magnets. The 1.2 mrad deflection in the XZ plane is needed in order to compensate the effect of the STRAW magnet placed downstream.

nal event. To avoid this unfortunate situation and reduce this background to a reasonable level, NA62 makes use of the CHarged ANTI-counter, or *CHANTI* [34].

The CHANTI is placed in vacuum, right after the last GTK station and outside of the beam acceptance. The detector is made of plastic scintillator counters intercepting charged tracks produced at angles from 49 mrad to 1.34 rad with respect to the beam nominal direction and generated at the Z position of the GTK3.

In particular, the CHANTI consists of six square hodoscopes, 30 cm side, placed in vacuum along the beam direction (fig. 2.8). A central rectangular hole of $65 \times 95\text{mm}^2$ with the longer side along the horizontal x-axis is present so that the detector doesn't interfere with the beam. The scintillator bars have a triangular cross section and the signal is read out with WLS (Wave-Length Shifting) fibers coupled to silicon photomultipliers (SiPM).

The single hit time resolution of the detector is 1.14 ns, while the position of the hit can be measured with a resolution of 2.5 mm.

2.4.4 STRAW

As already discussed in 2.1, the kinematic rejection of the background for the $K^+ \to \pi^+\nu\bar{\nu}$ measurement is based on the squared missing mass (eq. 2.1), which relies on the measurement of the momentum and direction of the beam particles and of the decay products.

The measurement of momentum and direction of the decay products downstream the decay region (e.g. the π^+ in the final state of the $K^+ \to \pi^+\nu\bar{\nu}$ decay) is accomplished with the STRAW Spectrometer (fig. 2.9). Unlike the compact design of the silicon pixel stations of the GTK, the STRAW is a 35 m long and 2 m wide straw tracker [35], in order to maximize the angular acceptance for the π^+ from the K^+ decays.

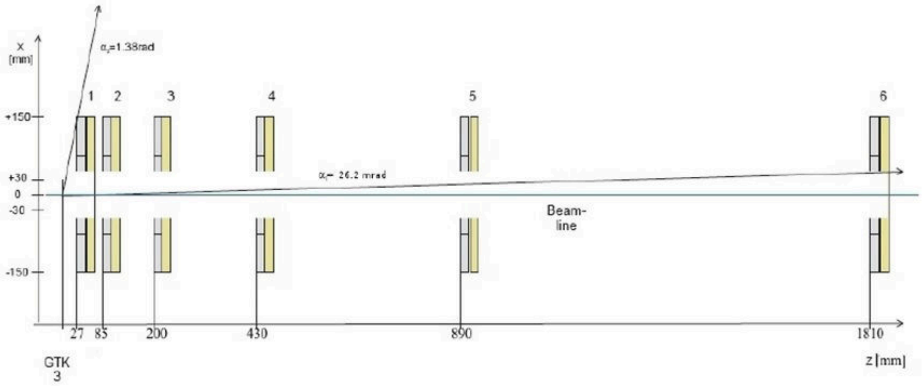

Figure 2.8: CHANTI stations layout, where the Z coordinate is measured with respect to GTK3.

The Spectrometer is composed of 4 chambers, placed in vacuum at the end of the decay region, and a dipole magnet (MNP33) of $B = 0.36$ T providing a 270 MeV/c p_T kick, placed between the second and the third station. The chambers are 10 m distant from each other, except for the last one that is 15 m far from the third one. Each chamber is made of four views (X,Y,U,V), where the straw tubes in the X and Y view follow the horizontal and vertical direction, while the U and V view are perpendicular with respect to each other like X and Y, but with a 45° tilt (fig. 2.10, left). The straw tubes in each view are placed following a certain pattern that is depicted in fig. 2.10, in order to guarantee geometrical coverage.

The straw tubes ($\oslash = 9.75$ mm and 2.1 m long) are realized with a 36 µm thick Mylar foil with a $50 - 20$ nm thick Cu-Au metalization and a 30 µm gold-plated tungsten wire. The gas mixture used is 70% Ar and 30% CO_2 to guarantee a maximum drift time of the order of 150 ns with an operating voltage of 1750 V.

The reconstruction of the track is based on a Kalman filter fit technique; the time resolution of the track is of the order of 5 ns, while the resolution of the $K^+ \to \pi^+\pi^0$ squared missing mass peak is measured to be 1.2×10^{-3} GeV^2/c^4, close to the design value [36].

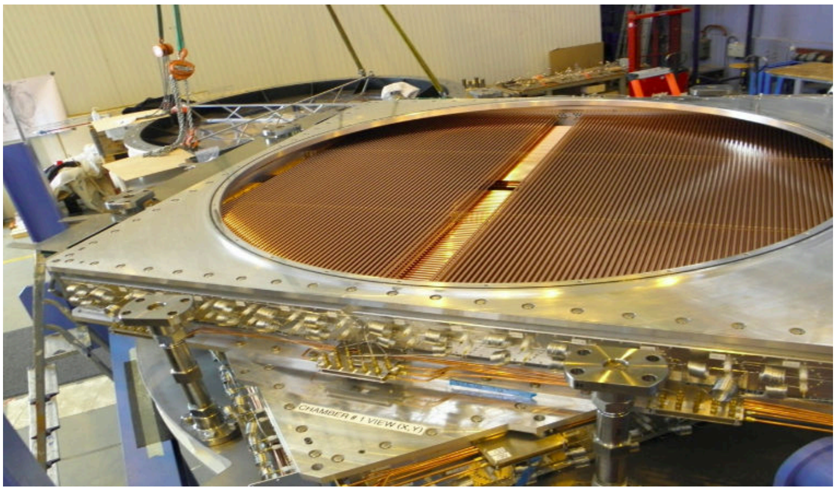

Figure 2.9: A picture of one of the STRAW detector chambers prior to installation.

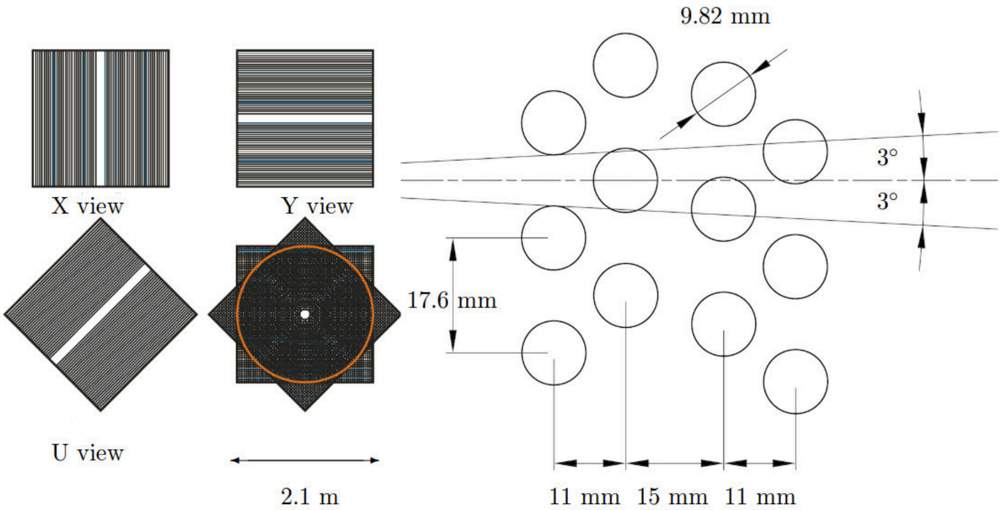

Figure 2.10: Left: drawing of the four views present in each STRAW chamber. Right: pattern of the straw tubes in each view of a chamber in the STRAW.

2.4.5 RICH

The Ring Imaging Cherenkov (RICH) of NA62 is a key element for the particle identification, in particular for the separation of pions, muons and electrons in the downstream region.

One of the main background to the $K^+ \to \pi^+\nu\bar{\nu}$ signal in NA62 is the $K^+ \to \mu^+\nu_\mu$, with a $BR \sim 63\%$ which needs to be suppressed by a rejection factor of 4×10^{13}. This can be accomplished with a combination of kinematical cuts, the muon veto system and the RICH. In particular, the RICH has to provide a rejection factor of 10^2 in the momentum range from 15 to 35 GeV/c.

In addition to this, the crossing time of the track must be measured by the RICH at a precision level better than 100 ps in order to have an efficient association between the downstream track passing through the RICH and the upstream track (the kaon) identified in the KTAG. Moreover the RICH provides a fast L0 trigger signal.

The muon misidentification probability should not go above 1% level in order to achieve the required $\pi - \mu$ separation. The best separation is achieved for low momentum, ideally close to the Cherenkov threshold. On the other hand, in order for the detector to be efficient at 15 GeV/c, the threshold needs to be $\sim$ 12.5 GeV/c: the refractive index corresponding to this threshold is $(n-1) = 6.2 \cdot 10^{-5}$, which is almost equal to the refractive index of Neon at atmospheric pressure. The smallness of (n-1) imply a low number of Cherenkov photons, which is compensated by having a long radiator.

A 17 m long vessel is filled with Neon slightly above atmospheric pressure and constitutes the radiator with a volume of 200 m^3 [37] (see fig. 2.14). An aluminium beam pipe[2] crosses the vessel, allowing undecayed particles to travel in the vacuum until the end of the NA62 detector where they are eventually dumped. The vessel is divided into four sections with decreasing diameter, from 3.9 m upstream to 3.2 m downstream and the total radiation length is 5.6% X_0. At the downstream end of the vessel there is a spherical mirror with a 17 m focal length that is actually a mosaic of 20 hexagonal mirrors, as shown in fig. 2.11. The mirrors reflect the photons into two different spots at the upstream end of the vessel, where two flanges of photomultipliers are housed. Each flange contains 976 Hamamatsu R7400-U03 PMTs [38].

The time resolution of the detector is shown in fig. 2.12. It can be evaluated dividing the ring randomly into two groups of hits and calculating the difference between the average time of the two groups, or comparing the time of the full ring with the time of the KTAG candidate. The time resolution for rings generated by (ultrarelativistic) electrons is found to be $\sim$ 70 ps [39].

The PID performances of the RICH can be assessed computing the squared mass of the candidate particle, calculated from the velocity

[2]The aluminium beam pipe starts at the entrance window and passes through the following sub-detectors.

measured by the RICH and the momentum measured by the spectrometer,

$$m^2 = p^2 \cdot \frac{n^2 - 1 - \left(\frac{R}{f}\right)^2}{c^2 \left[1 + \left(\frac{R}{f}\right)^2\right]} , \tag{2.2}$$

where p is the momentum, n is the refractive index of neon, R is the radius of the reconstructed Cherenkov ring and f is the focal length of the mirror; the squared mass for different kind of particles is plotted in fig. 2.13. A cut on the squared mass allows to select pions and reject muons. For instance, in 2016 a π identification efficiency of 90% has been measured to correspond to a muon mis-identification of 0.8% [37].

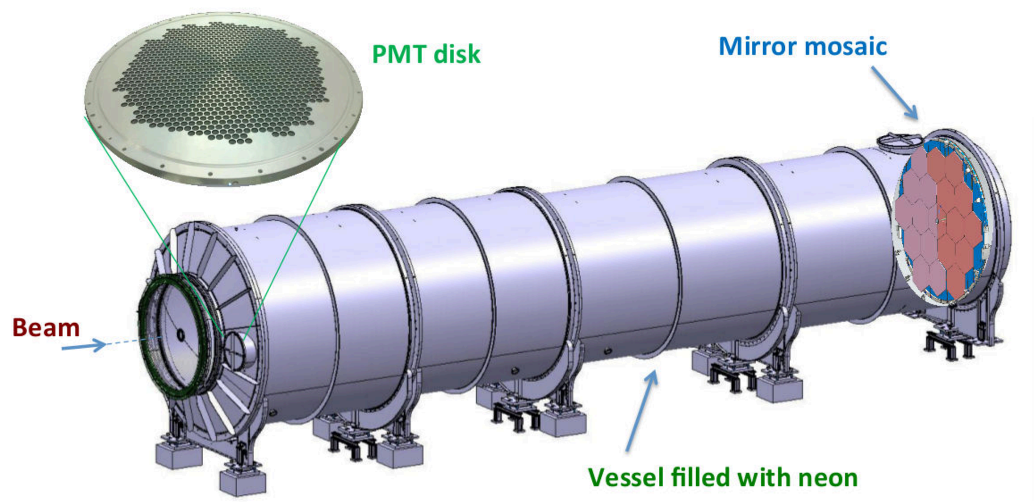

Figure 2.11: Schematic drawing of the RICH detector. The beam travels in vacuum inside the beam pipe, from left to right.

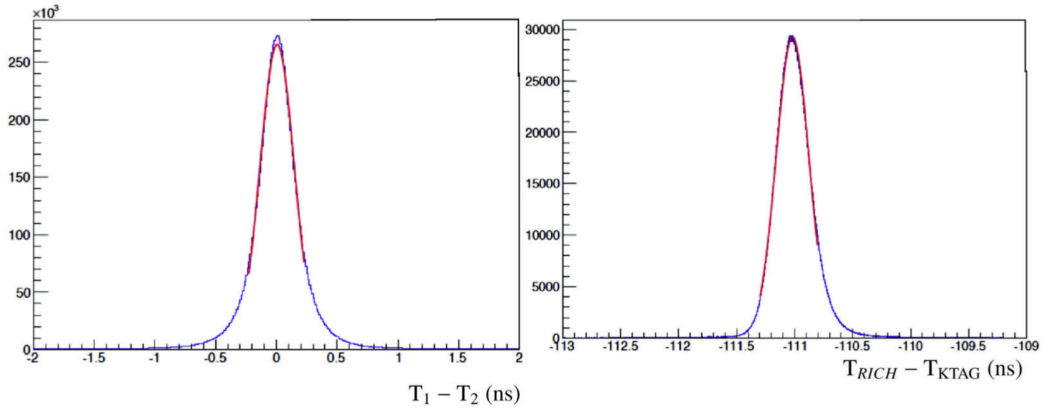

Figure 2.12: Left: difference between the average time of two subsets of hits in the same ring in the RICH. Right: difference between the time of a ring in the RICH and the time of the KTAG candidate.

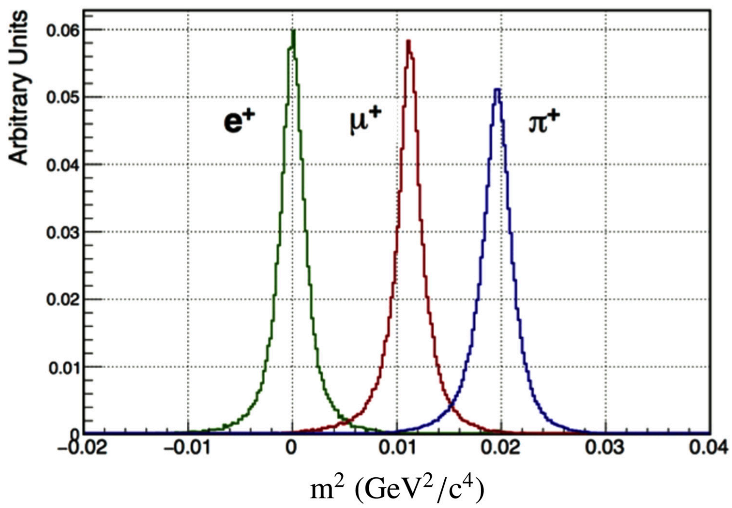

Figure 2.13: Squared mass for electrons, muons and pions reconstructed using the velocity measured by the RICH and the momentum reconstructed by the spectrometer.

Figure 2.14: A picture of the downstream part of the NA62 detector. The RICH green vessel is clearly visible; on the left there is the gray tank of the LKr calorimeter; between the LKr and the RICH, the CHOD is partially visible; the blue MNP33 magnet of the STRAW spectrometer can be spotted on the right.

2.4.6 The Hodoscopes

Two hodoscopes are present in NA62: the old NA48-CHOD (or simply CHOD) and the NA62-CHOD (also known as NewCHOD). Both hodoscopes are used for multiplicity rejection in the context of the $K^+ \to \pi^+ \nu\bar{\nu}$ analysis, to detect photonuclear reactions of pions in the RICH mirrors and to take part in the L0 trigger: the old CHOD provides the control trigger while the time of the NewCHOD is exploited in the physics trigger.

The **CHOD** detector (Charged HODoscope) is an hodoscope located downstream LAV12 and made of 128 plastic scintillators, with 20 mm thickness (0.1 X_0) divided into two planes (see fig. 2.15), that provides the L0 signal for the control trigger and the track time for events with a charged particle in the final state. The upstream plane contains 64 vertical-oriented scintillators, while the second plane has 64 horizontal-oriented scintillators. The scintillators in each plane are divided into four quadrants, each with 16 scintillators whose length vary between 1200 mm for the central slabs to 600 mm for the external ones, forming an octagon shape (see fig. 2.15); in each quadrant the scintillator width ranges from 6.5 cm for the 11 internal slabs to 9.9 cm for the 5 external ones. The scintillation light from each counter is collected with a plexiglas light guide and detected by a photomultiplier Photonis XP2262B.

A particle travelling through the detector releases two in-time signals into the scintillators, one into a vertical counter and one into a horizontal one. The intersection point of the two counters defines the position of the track with a time resolution varying from ~ 200 ps in 2016 to ~ 250 ps in 2018.

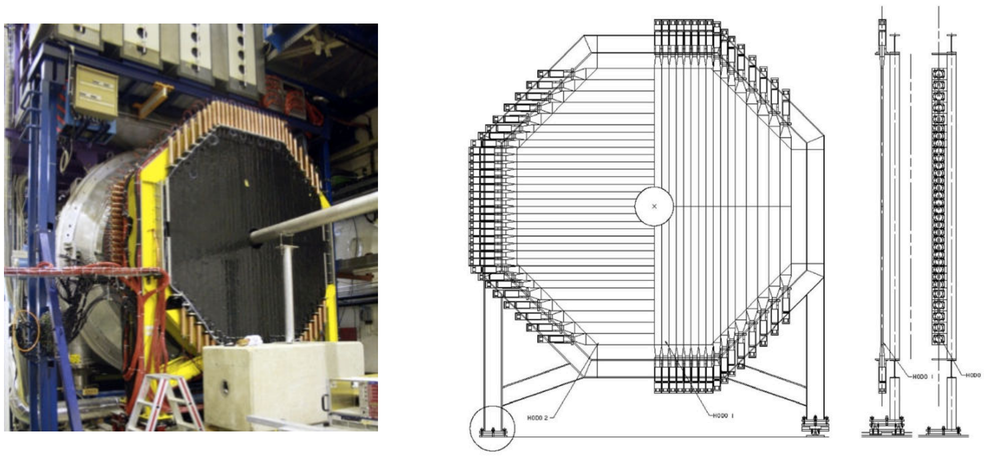

Figure 2.15: Left: picture of the CHOD detector before the installation of the RICH. Right: schematic front and lateral views of the CHOD detector.

The **NewCHOD** detector is a hodoscope with a pad structure and 152 scintillation counters [40]. The detector covers an annular area around the beam pipe, with a radius ranging from 140 to 1070 mm, and is placed right after the RICH and in front of the LAV12 detector mainframe. The scintillators are 30 mm thick and have typical sizes of 267.5×108 mm^2 and 133.75×108 mm^2, organized in rows (see fig. 2.16). The scintillation light is collected by WLS fibers and detected by SiPMs. The time resolution measured during the 2016 data taking is (1.01 ± 0.01) ns.

2.4.7 LKr

Together with the RICH, the NA48 liquid krypton calorimeter (LKr) is a key element for the particle identification in NA62. Moreover, the LKr is used to provide a signal for the trigger and acts as a photon veto, covering angles between 1 and 8.5 mrad. It is a 27 X_0 quasi-homogeneous electromagnetic calorimeter placed between the CHOD and the MUV1 (fig. 2.17), filled with 9000 litres of liquid krypton at 120 K, placed inside a cryostat. The calorimeter is 127 cm deep and extends for a radius of 128 cm around the beam pipe and is composed of 13248 longitudinal cells with a 2×2 cm^2 cross section (fig. 2.18) [28].

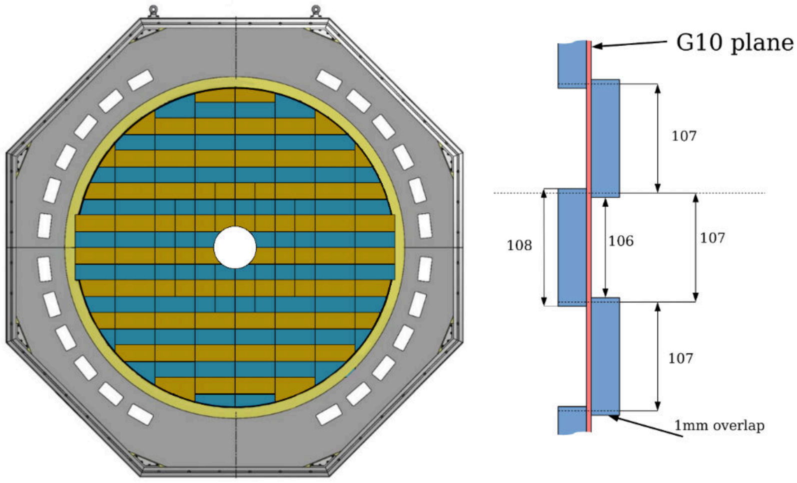

Figure 2.16: Schematic drawing of the NewCHOD detector. Left: support panel and scintillator tiles. Right: tile rows layout.

The energy resolution obtained from data is

$$\frac{\sigma(E)}{E} = \frac{4.8\%}{\sqrt{E}} \oplus \frac{11\%}{E} \oplus 0.9\% \;, \tag{2.3}$$

where the energy E is measured in GeV [28]. The spatial resolution is 1 mm, while the time resolution can go from 0.5 to 1 ns, depending on the energy release. Clusters are built starting from a seed that is a cell with energy $E_{\text{seed}} > 250$ MeV, larger than the energy of the 8 adjacent cells.

2.4.8 MUV

The Muon Veto System (MUV) of NA62 consists of three different detectors (MUV1, MUV2 and MUV3) and it complements the RICH and the LKr for the π/μ discrimination.

MUV1 and **MUV2** together form a hadron calorimeter, placed right after the LKr calorimeter (fig. 2.17), made of alternate planes of iron and scintillator accounting for about 8 interaction lengths. The front detector (MUV1) was newly constructed specifically for NA62, whereas MUV2 is the front layer of the former NA48 hadron calorimeter tilted by 180°. In particular, MUV1 contains 24 layers of 26.8 mm thick iron plates, 12 mm distant from each other, covering an area of 2700 × 2600 mm^2 around the beam pipe. 23 layers of scintillator strips (9 mm thick, 60 mm wide, 2600 mm long) are placed between the iron plates. Each layer has the strips either vertically or horizontally aligned, alternately. Similarly to MUV1, MUV2 consists of

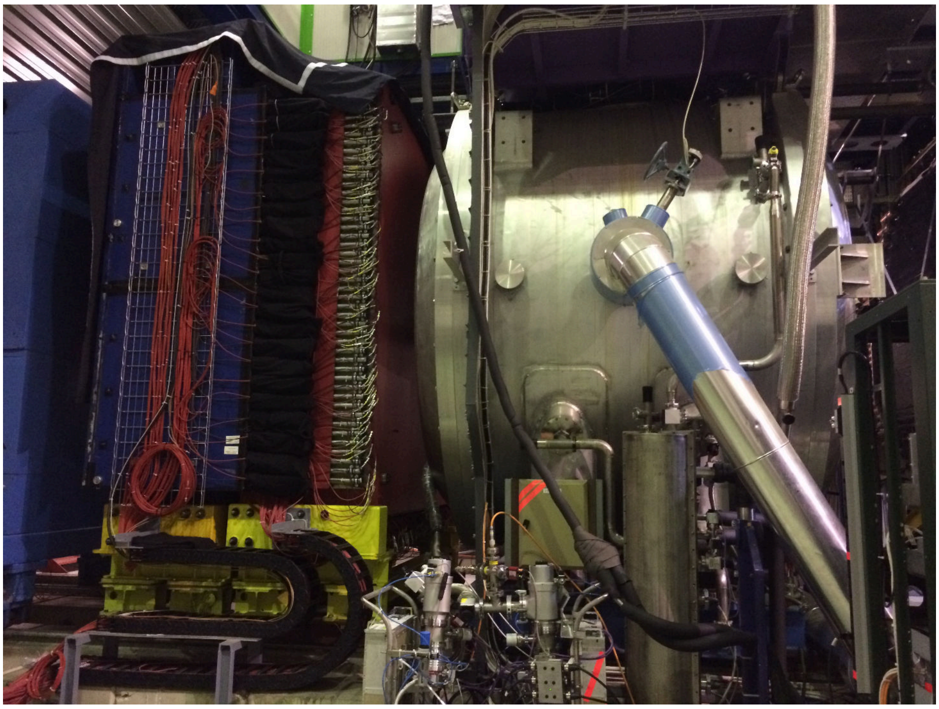

Figure 2.17: From left to right: the MUV1/MUV2 hadron calorimeter and the tank containing the LKr calorimeter. The beam travels from right to left (https://cds.cern.ch/record/2274473).

alternate layers of iron plates (24 layers, 25 mm thickness) and plastic scintillators. The scintillator layers are composed by 44 strips for each half of the calorimeter, with a total of 88 strips per scintillator plane; each strip is 1300 mm long, 119 mm wide and 4.5 mm thick and, like for MUV1, they are alternately aligned horizontally or vertically in each consecutive plane. The time resolution of the calorimeter measured with respect to the CHOD was found to be 0.9 ns, while the energy resolution is

$$\frac{\sigma(E)}{E} = 0.115 \oplus \frac{0.38}{\sqrt{E}} \oplus \frac{1.37}{E} \ , \tag{2.4}$$

where the energy E is measured in GeV [28].

The last component of the muon veto system is the **MUV3**, or **Fast Muon Veto**. An 80 cm thick iron wall separates the hadron calorimeter from the MUV3, so that a particle detected by the MUV3 has to survive the whole calorimetric system (LKr, MUV1 and MUV2) plus the iron wall: this means that the particle has to go through more than 14 interaction lengths. Therefore the MUV3 is used as a fast muon veto at L0 trigger, and also for

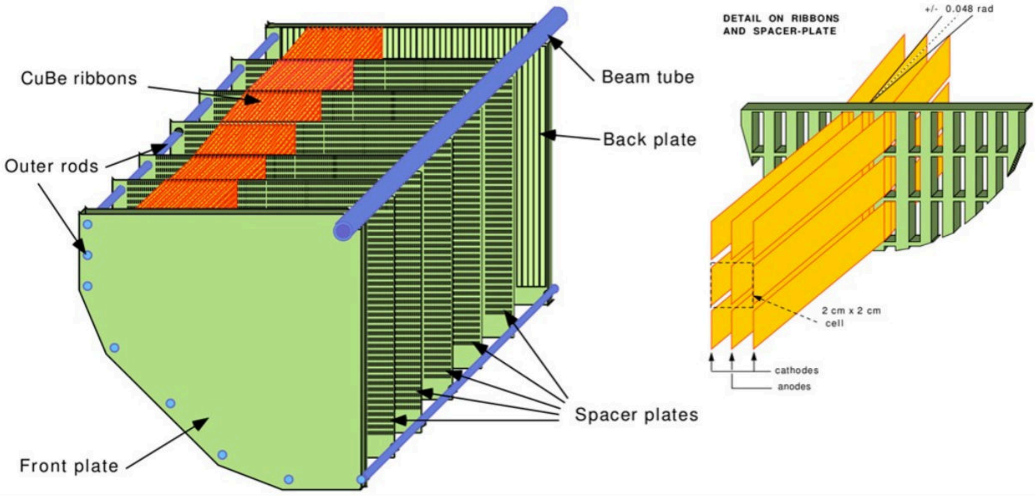

Figure 2.18: Left: structure of one quadrant of the LKr calorimeter. Right: detailed view of a cell structure.

muon identification. The detector is made of 50 mm thick scintillator tiles with different dimensions (140 tiles are 220×220 mm^2 plus 8 smaller tiles around the beam pipe), covering a total area equal to 2640×2640 mm^2. The time resolution of muons transversing single channels was measured to be in the range $0.4 - 0.6$ ns in 2015.

2.4.9 Photon veto

One of the most dangerous background for the measurement of $K^+ \to \pi^+ \nu \bar{\nu}$ is the $K^+ \to \pi^+ \pi^0$ decay. For this reason NA62 needs a hermetic and efficient photon veto to detect the photons from the decays of π^0's and reject the event. In particular, since the kinematic cuts provide a rejection factor of 10^4 for $K^+ \to \pi^+ \pi^0$ events, the remaining 10^8 rejection factor is left to the photon veto, where the requirement on the momentum range of the π^+ (15 GeV/c $< P_{\pi^+} <$ 35 GeV/c) ensures that the pair of photons from π^0 decays has an energy above 40 GeV. The photon veto system of NA62 makes use of different kind of sub-systems, each covering a specific angular region: the Large Angle Veto (LAV), the Liquid Krypton calorimeter (LKr), the Inner Radius Calorimeter (IRC) and the Small Angle Calorimeter (SAC) [28].

The **LAV** [41] is composed of 12 stations placed all along the beam direction, spaced by 6 m downstream and 12 m upstream (see fig. 2.5), providing full hermeticity for photons emitted at angles between 8.5 and 50 mrad with respect to the Z axis. The first eleven stations are placed along the fiducial decay volume, while the last one is located between the RICH and the CHOD, outside the vacuum tank, 3 m upstream the LKr, and is operated in air. Each station is made of 4 or 5 rings of lead-glass crystals (see fig. 2.19), each crystal read by a PMT, where every ring is staggered in azimuth with respect to the others in order to have good hermeticity. The rings are placed in a plane perpendicular to the beam direction. When one of the two photons from a $K^+ \to \pi^+\pi^0$ decay has an energy below 200 MeV, it is emitted at angles larger than the LAV coverage. Besides its fundamental role in the photon veto, the LAV takes part in the physics trigger.

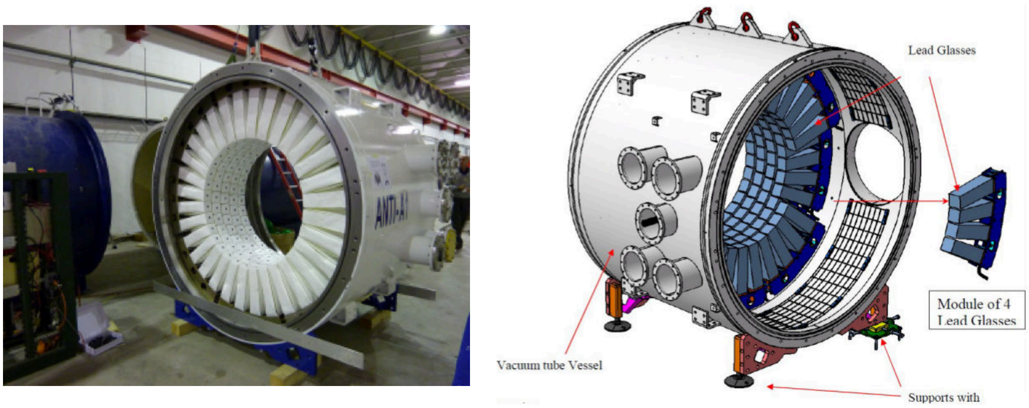

Figure 2.19: Left: picture of one of the LAV stations. Right: drawing of one of the LAV stations.

For angles between 1 and 8.5 mrad, the photon veto is provided by the LKr calorimeter. More details on this detector can be found in 2.4.7.

In order to veto photons emitted at small angles, NA62 is equipped with a Small Angle Veto (**SAV**), that consists of two shashlyk calorimeters (lead and plastic scintillator plates), IRC and SAC covering angle from 1 down to zero mrad.

The **IRC** (Intermediate-Ring Calorimeter) is placed right before the LKr and covers a ring-shaped region with an outer radius of 145 mm around the Z axis, while the inner radius is 60 mm but it has an offset of 12 mm towards positive X because of the deflection caused by the Spectrometer magnet on the beam particles. The IRC is composed of two modules, placed one after the other, with a depth of 89 and 154 mm (19 X_0).

The **SAC** (Small Angle Calorimeter) is placed right at the end of the NA62 detector, just upstream the beam dump, and covers the remaining angular region down to zero mrad. It consists of $70 + 70$ alternate layers of lead and plastic scintillators, with a transverse area of 205×205 mm^2 and a

1.5 mm thickness (19 X_0). The energy resolution is

$$\frac{\sigma(E)}{E} = \frac{8.8\%}{\sqrt{E}} \oplus \frac{7.1\%}{E} \ . \tag{2.5}$$

2.4.10 Additional veto detectors for $K_{3\pi}$

Two additional detectors for vetoing the $K^+ \to \pi^+\pi^-\pi^+$ decay (from now on $K^+_{3\pi}$) are present, namely MUV0 and HASC [28].

The **MUV0** is a scintillator hodoscope that detects π^- from $K^+_{3\pi}$ with momenta below 10 GeV/c. Those π^- experience a deflection towards positive X from the Spectrometer magnet, which is applied on top of the deflection caused by the TRIM5 magnet on the K^+ beam. For this reason, the MUV0 has been installed on the downstream flange of the RICH and covers a lateral area with 1.545 m $< X <$ 2.945 m and $|Y| <$ 0.7 m, and a total active surface of (1.4×1.4) m^2. The detector is composed of two layers with 48 scintillator tiles of dimension $(200 \times 200 \times 10)$ mm^3, grouped into 9 super-tiles, with the signal from each super-tile is read by a photomultiplier.

The **HASC** (HAdronic Sampling Calorimeter) was installed in order to detect the π^+ from $K^+_{3\pi}$ with momenta above 50 GeV/c, when they propagate through the holes at the center of the Spectrometer chambers. Since the detector is located after the MUV3, in a region where the BEND magnet sweeps away the π^+ in the K^+ beam towards negative X, the HASC covers an area with -0.48 m $< X < -0.18$ m and $|Y| <$ 0.15 m. It is composed of 9 modules $(100 \times 100$ mm$^2)$, where each module is a sandwich of 60 lead plates with 16 mm thickness intervalled with 60 scintillator plates with 4 mm thickness.

2.4.11 TDAQ system

The very high intensity of the NA62 beam requires the presence of a trigger and data acquisition system able to maintain a high acceptance for signal events while keeping a remarkable rejection of the background and minimizing the dead time. The most efficient and cost effective solution that met these requirements was an integrated trigger and data acquisition system (**TDAQ**) [42].

Currently in NA62 two trigger levels are present: a low-level trigger at hardware level called Level 0 (**L0**) and a high-level trigger called Level 1 (**L1**) at a software level. The L0 collects logical signals (*primitives*[3]) from CHOD,

[3]The L0 primitives are 64 bit words containing time and detector-specific information for each event.

L0Q1	Coincidence between hor. and vert. plane of the CHOD
L0RICH	Cluster of hits in time in the RICH
L0NA62CHOD	$1 \leq 4$ hits in the NewCHOD
L0QX	Hits in opposite quadrants of the NewCHOD
L0MUV3	Tile multiplicities in the MUV3
L0LAV12	Signal from one or more LAV12 blocks
L0Calo	$E \geq 30$ GeV in the LKr or more than 1 cluster

Table 2.2: Different trigger components used as input in the L0 trigger.

NewCHOD, RICH, LKr, LAV and MUV3, with an input rate of 10 MHz, that are combined in a dedicated FPGA-based L0 trigger processor (**L0TP**). The L0TP checks the time alignment of the primitives and consequently sends the L0 trigger decision to the readout of the detectors whenever the primitives match predetermined configurations called **masks**; a list of the primitives that can be used as input in the L0TP can be found in table 2.2.

At nominal beam intensity, the detectors are required to sustain extremely high rate and, in addition, a good resolution is mandatory already at the trigger level. The 750 MHz total rate of beam particle produces an event rate of 10 MHz in the acceptance of the downstream detectors. With a typical value of 1 ns, the time resolution at the trigger level can be considered efficient enough, minimizing fake triggers and signal rejection due to random veto. Most of the detectors adopted high-performance TDC and FPGA-based readout systems consisting in TEL62 boards and TDCB daughter-cards (see fig. 2.20) [43]. Some detectors (GTK, STRAW, LKr, MUV1 and MUV2) adopted different solutions due to specific constraints: the readout system of the GTK uses TDCPix chips to provide the hit time and time over threshold, sending the output to the GTK-RO VME 6U carrier board [44]; the STRAW spectrometer readout is based on the CARIOCA chips [45], integrated in a custom COVER board with an Altera Cyclone III FPGA [46][47]; the LKr, MUV1 and MUV2 calorimeters adopted a Flash ADC readout, where the basic element is the CREAM (Calorimeter Readout Module) that is a VME 6U board using four 8-channels, 14-bit ADCs [48]; the IRC and SAC use two different readout systems, the TDCB-TEL62 one and the CREAM-based system.

Typically, in 2017 data taking the physics mask for $\pi\nu\nu$ was defined as L0RICH·L0NA62CHOD·!L0QX·!L0MUV3·!L0Calo, while the control trigger made use just of the CHOD detector and was defined simply as L0Q1 but

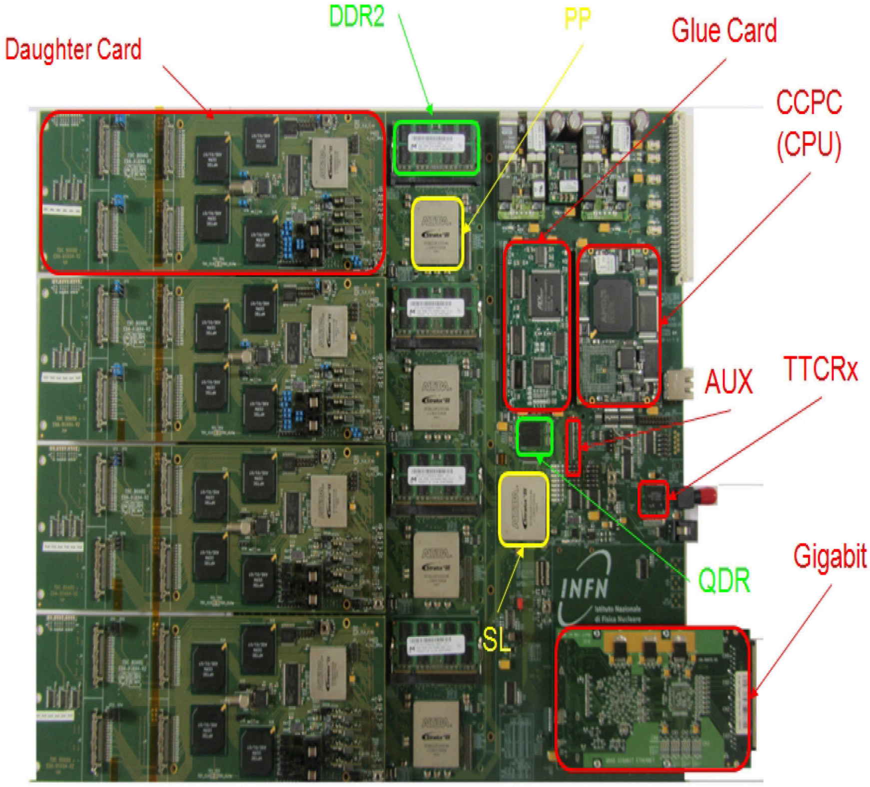

Figure 2.20: A TEL62 board equipped with four TDCB daughter-cards.

with a downscaling factor of 400.

When the detectors get a positive response from the L0, data are read out by the front end electronics, Multi Event Packets (MEPs) are built and sent to a PC Farm, with a rate of 1 MHz. Subsequently the L1 collects and processes data from KTAG, STRAW and LAV and produces higher level information that is used as a trigger at a software level; the rate out of the L1 is reduced to about 100 kHz and the final data sample can be stored for offline analysis. The L1 algorithms used in the analysis are shown in table 2.3.

A schematic view of the trigger and data acquisition process is shown in fig. 2.21. In order to have the correct association between triggered events and collected data, a precise synchronization at the level of 100 ps is required: NA62 employs a common clock with a frequency of 40.079 MHz, a combined system of a Logic Trigger Unit (LTU) and a Timing, Trigger and Control (TTC) boards to encode and deliver the clock and the trigger data to the readout of the detectors. The fundamental time unit is the inverse

L1KTAG	coincidence of ≥ 4 KTAG sectors within ± 5 ns with respect to L0 trigger time.
L1LAV	≤ 2 hits in the whole LAV system within ± 10 ns with respect to the L0 trigger time.
L1STRAW	longitudinal track momentum $P_z \leq 50$ GeV/c; closest distance of approach (CDA) to the beam axis ≤ 200 mm; vertex longitudinal position of the CDA ≤ 180 m; CDA between two reconstructed tracks ≥ 30 mm.

Table 2.3: Different algorithms used in the L1 trigger.

of the clock frequency, namely the *timestamp*, with a value of 24.950741 ns. The SPS announces the arrival of the protons sending a warning and synchronization signal, the Start-Of-Burst (SOB), one second before the actual extraction of the beam, enabling the detectors to start the data acquisition. Approximately 0.5 s after the end of the spill, the SPS sends an End-Of-Burst (EOB) signal; therefore the basic unit of data acquisition in NA62 is the spill, with a duration of ~ 6 s, and it is commonly referred to as **burst**. A coherent sequence of bursts taken within a few hours without significant changes to the NA62 hardware or to the data taking conditions is called **run**; the typical good run contains usually about 1500 bursts.

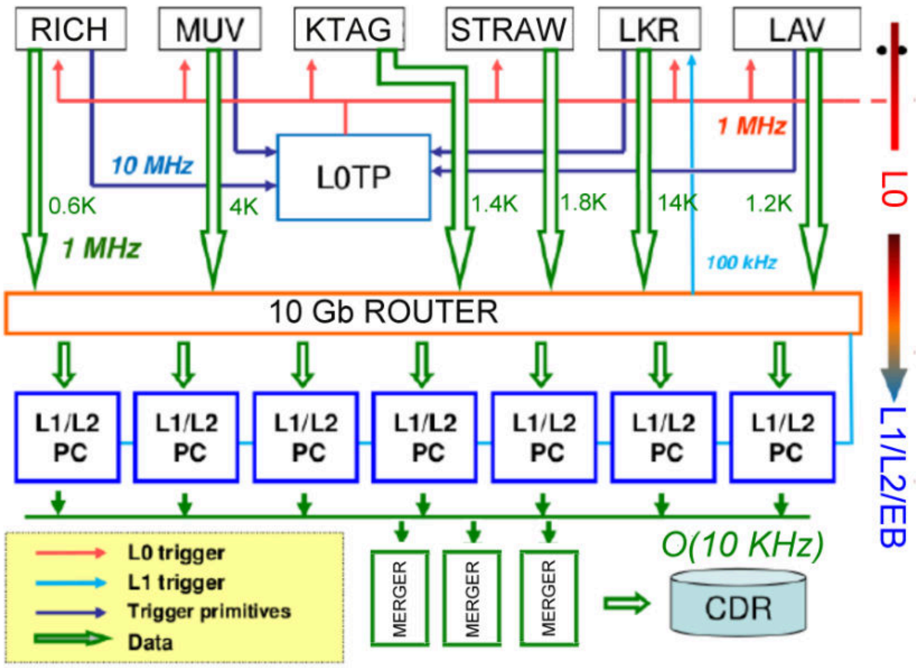

Figure 2.21: Simplified representation of the trigger and data acquisition process of NA62.

Chapter 3

Signal selection and background evaluation

In this chapter, the analysis strategy for the measurement of the $K^+ \to \pi^+ \nu\bar{\nu}$ decay[1] will be presented, along with the criteria for the signal selection and the evaluation of the relevant sources of background; the evaluation of the upstream background, the most important residual background source, is extensively described in chapter 4.

As explained below, a blind analysis strategy is adopted to protect against bias, and the selection is mostly cut based. Since most of the cuts used in the selection are the same used in the 2016 analysis, I will report all of them, but I will describe into details only the main differences, while a complete explanation of the 2016-like selection procedure can be found in [18] and [49].

3.1 The NA62 software framework

The data collected by the NA62 detectors are written into binary files, the *raw files* with a typical size of a few GB per burst. The NA62 collaboration developed a framework (**NA62FW**), mostly based on C++, in order to decode and reconstruct the raw files, simulate MC events and analyze the reconstructed files [50]. NA62FW consists of three main packages:

- `NA62MC`: a Geant4 [51] based package that provides a full NA62 detector simulation, with the possibility to define the beam shape, decay mode and the list of interactions to be considered.
- `NA62Reconstruction`: a ROOT [52] based reconstruction package. `NA62Reconstruction` decodes the event information, building objects

[1] From now on I may refer to the $K^+ \to \pi^+ \nu\bar{\nu}$ decay also as $\pi\nu\nu$.

called **hits**; each hit contains several information about the signal in the detector, such as the time, the amplitude and the channel number. Subsequently, the hits are grouped in higher-level objects called **candidates**, representing detector specific information such as tracks for the Spectrometer, rings for the RICH and crossings between vertical and horizontal counters for the CHOD. When dealing with files generated with `NA62MC`, the first step done by the reconstruction is the so-called **digitization**, that emulates the response of the detector readout to the simulated signals; then the digitized hits pass through the same reconstruction procedure as the hits from data. The reconstruction takes care of applying time corrections to all the detectors hits and/or candidates, such as T0's and time-walk corrections.

- `NA62Analysis`: a ROOT based analysis framework. `NA62Analysis` contains several tools and template classes called **Analyzers**, enabling the user to access the reconstructed files in an easy and direct way.

3.2 Data samples

The NA62 Collaboration took data for the measurement of the $K^+ \to \pi^+ \nu \bar{\nu}$ decay from 2016 to 2018; the data samples have been divided into 3 main different subsamples, one for each year. The 2016 run lasted 30 days, from mid-September to mid-October, and $\sim 10^{11}$ K^+ decays were collected. The 2017 run refers to the period from May to October, for a total of 161 days of data taking and $\sim 3 \times 10^{12}$ K^+ decays collected. 2018 was the last year of data taking before the Long Shutdown 2, and data were taken for 217 days from March to November, recording $\sim 5 \times 10^{12}$ K^+ decays.

A further sub-division of the 3 annual data sets (2016, 2017 and 2018) is done: different periods during the same year correspond to different conditions of the detector during the data taking and they require a special treatments at the reconstruction and analysis level. In particular, in the following chapter I will refer to two different periods of 2017 that I will call **2017-I** and **2017-II**[2]; data collected in 2017-II were taken after the insertion of a shielding[3] (see fig. 3.1) in the upstream part of the detector that removed part of the upstream background (see chapter 4), hence it is important to distinguish the two periods when analysing the upstream background characteristics.

[2]Actually, these two sub-samples are called 2017A and 2017B in the `na62fw`, but I chose to change nomenclature in order to avoid confusion with the naming convention used for the definition of the bifurcation analysis samples in chapter 4

[3]A copper block.

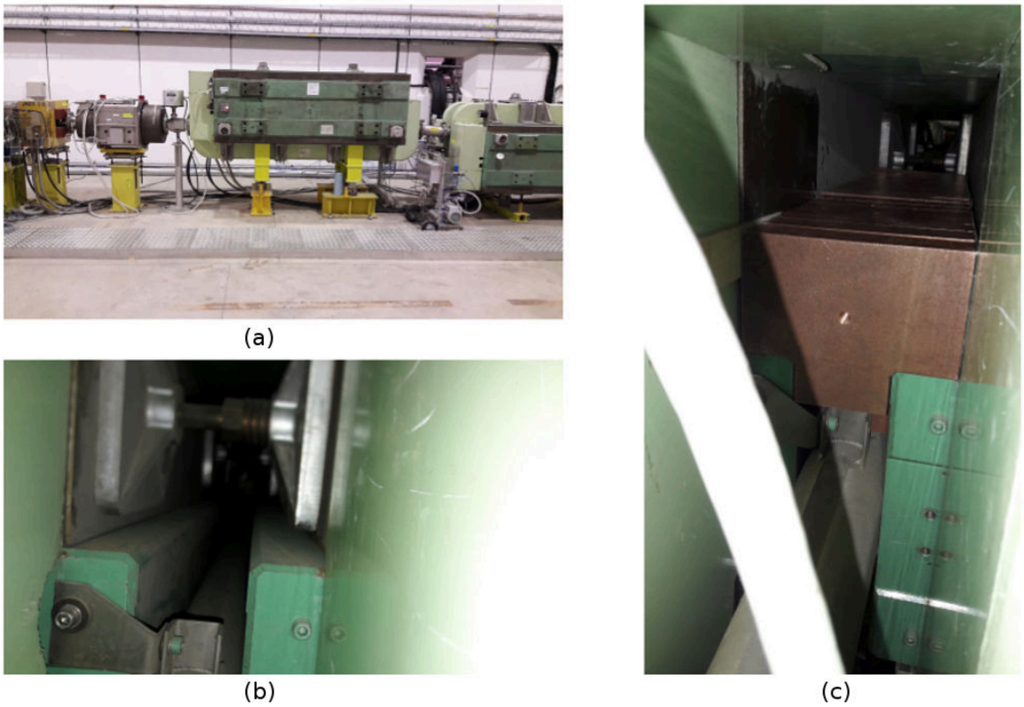

Figure 3.1: (a) From left to right: the TRIM5 magnet, the old collimator and the last achromat. (b) The inside of the last magnet of the achromat, before the insertion of the shielding. (c) The inside of the last magnet of the last achromat, with the copper shielding inserted in September 2017.

Prior to performing the analysis, the data must pass through different stages. The first step is the reconstruction, that builds objects like hits and candidates, with well-defined data members and member functions (see also 3.1). The reconstructed file undergoes a filtering procedure, where a loose selection on the data is performed. There are several filtering analyzers for different kind of analysis; the filter used for this analysis (called $\boldsymbol{\pi\nu\nu}$ **Filter** or **PNN Filter**) applies the following selection criteria:

- no global reconstruction errors in any of the detectors;
- event triggered by the L0 PNN mask;
- at least 1 and not more than 10 candidates reconstructed in the Spectrometer;
- at least 2 CHOD hits, one in a vertical and the other in a horizontal counter, both in the same quadrant;
- at least 1 Spectrometer track with the following characteristics and requirements:
  - hits in all 4 chambers;
  - $\chi^2 \leq 30$;
  - difference between the momentum before and after the fit not greater than 25 GeV/c;
  - extrapolation of the track in the acceptance of NewCHOD, CHOD, LKr and MUV3;
  - no good vertex with any other track with hits in 4 chambers and $\chi^2 \leq 30$; a vertex is *good* if the closest distance of approach (CDA) is less than 10 mm, the Z coordinate of the vertex is between 80000 and 180000 mm and the tracks are in a ± 10 ns time window with respect to each other;
  - momentum between 8 and 50 GeV/c;
  - at least 1 KTAG candidate with at least 4 sectors in a ± 5 ns time window with respect to CHOD;
  - at least 1 hit in each GTK station in a ± 2 ns time window with respect to CHOD;
  - no hits in MUV3 associated to the track in a ± 4 ns time window with respect to CHOD;

  - no photons in the LKr, where a photon in this case is defined as a cluster at least 180 mm away from the extrapolation of the track and in a ± 5 ns time window with respect to CHOD;
  - no photons in LAV, where a photon in this case is defined as a signal in any LAV block selected by the standard matching tool in a ± 2 ns time window with respect to CHOD.

The output of the filter is noticeably smaller than the original, but the data structure inside the file is still compatible with the parent reconstructed files; moreover, the filter selection is loose and general enough to enable different approaches to the same analysis.

The very last step in the data processing is extremely analysis-specific and is simply called *reduction*. In reduced files, candidates and hits are removed and only the values of the most important variables that will be used in the analysis are kept in a ROOT tree. Most of the values stored in this tree are high-level variables such as the squared missing mass, the boolean value of the photon veto response in the LAV, or the position of the downstream track extrapolated at the first chamber of the STRAW. The reduced files are much smaller and the structure is a simple ROOT tree, consequently the analysis performed on the reduced files is orders of magnitude faster than on the filtered files.

It is worth mentioning that some bursts (or, sometimes, whole runs) are discarded a priori from the analysis by the data quality software tools; this usually happens when there was a hardware failure during the data taking that cannot be recovered offline in any way.

3.3 Analysis strategy

As mentioned in 2.1, the signature of the $K^+ \to \pi^+\nu\bar{\nu}$ decay is just one charged track in the initial state and one charged track in the final state, with a missing mass from the two neutrinos. Thus, the main variable for the kinematic selection of the signal is the squared missing mass $m^2 = (P_K - P_\pi)^2$, where P_K and P_π are the 4-momenta of the kaon and the pion, respectively. The missing mass distribution for the signal is quite broad and overlaps with the distributions of various background sources, as shown in fig. 2.1. The main sources of background from kaon decays are:

- $K^+ \to \mu^+\nu_\mu$ ($K^+_{\mu 2}$): in the case that the muon is mis-identified as a pion, the $K_{\mu 2}$ can potentially be a background. Theoretically, the missing mass distribution for this process is completely contained in the negative side of the plot shown in fig. 2.1, with a peak close to zero, and therefore perfectly separated from the signal region; in reality, however, resolution effects come into play, spilling a significant part of this events into the signal region.

- $K^+ \to \pi^+\pi^0$ ($K^+_{2\pi}$): if the photons from the decay of the π^0 are lost, the $K_{2\pi}$ is indistinguishable from the signal, more so because its missing mass distribution happens to be right in the middle of the $K^+ \to \pi^+\nu\bar{\nu}$ missing mass distribution.

- $K^+ \to \pi^+\pi^+\pi^-$ ($K^+_{3\pi}$): the decays of this type populate the region with high missing mass and they can potentially become a background source if the kinematic variables are misreconstructed and the requirements on the track multiplicity fail.

- $K^+ \to \pi^+\pi^+e^+\nu_e$ (K^+_{e4}): because of the neutrino in the final state, the missing mass distribution of this process overlaps largely with the signal region at high missing mass, however its branching ratio is relatively very small ($\sim 10^{-5}$).

- Other K^+ decays such as $K^+ \to \mu^+\pi^0\nu_\mu$, $K^+ \to e^+\pi^0\nu_e$ and $K^+ \to \pi^+\gamma\gamma$ are found to be negligible with respect to this analysis.

Because of these features, two different regions in the m^2_{miss} can be identified in which the background is significantly lower, and can be used to select kinematically the signal: the first region (**R1**) between the $K_{\mu2}$ and the $K_{2\pi}$ peak, and the second region (**R2**) between the $K_{2\pi}$ peak and the $K_{3\pi}$ distribution. The pion is required to have a momentum between 15 and 35 GeV/c; the lower limit on the momentum is related to the RICH Cherenkov threshold, while the upper limit is chosen in order to keep an efficient PID in the whole momentum range (see also 2.4.5) and to have enough π^0 energy in $K^+_{2\pi}$ decays to veto the event. The branching ratios of the kaon decays listed above are reported in table 3.1.

The squared missing mass as a function of the pion momentum for the 2017 data sample is shown in fig. 3.2, where the signal and control regions are covered because of the blind analysis procedure adopted. The exact definition of the signal and control regions is given in 3.3.7.

3.3.1 Single-track event selection

Two main objects are created in the reduced tree, downstream tracks and upstream tracks. The **downstream track** is the candidate for the pion in the final state, built starting from a STRAW track candidate using as a reference

Process	Branching ratio
$K^+ \to \mu^+\nu_\mu$ ($K^+_{\mu 2}$)	63.56 %
$K^+ \to \pi^+\pi^0$ ($K^+_{2\pi}$)	20.66 %
$K^+ \to \pi^+\pi^+\pi^-$ ($K^+_{3\pi}$)	5.58 %
$K^+ \to \pi^+\pi^+e^+\nu_e$ (K^+_{e4})	4.3×10^{-5}
$K^+ \to \pi^+\nu\bar{\nu}$ (signal)	8.4×10^{-11}

Table 3.1: Branching ratios of the main kaon decays contributing to the background of $K^+ \to \pi^+\nu\bar{\nu}$. The branching ratio for the signal is reported as well for comparison.

the average time of the CHOD in a ±25 ns time window around the trigger time. The reconstructed tracks must always have associated candidates in RICH, NewCHOD, CHOD, and LKr; the track time is defined as a weighted average of the STRAW hits time and the matched candidates times in RICH, CHOD and LKr (the weights are inversely proportional to the detectors time resolution). The STRAW track is extrapolated and projected onto the XY plane of the downstream detectors (CHOD, NewCHOD, RICH and LKr) and associated with their candidates based on geometrical and time information. LKr, MUV1 and MUV2 hits are combined to reconstruct the total calorimetric energy of the downstream track, through a standard multi-variate algorithm (MVA) implemented in the NA62 software framework.

The **upstream track** is the candidate for the kaon in the initial state and it is built combining the information of KTAG and GTK. The track is reconstructed in the GTK using the time of the KTAG candidate as a reference.

The downstream tracks are associated to the upstream tracks using the time association and the closest distance of approach (**CDA**) between the two tracks. A matching discriminant is built starting from the CDA and $\Delta T = T_{\text{GTK}} - T_{\text{KTAG}}$ and represents the probability that the CDA and the ΔT have values larger than observed; the CDA and ΔT distributions prior to the selection are shown in fig. 3.3. The discriminant and the $K^+ - \pi^+$ matching definition are mostly unaltered with respect to the 2016 analysis, any changes to those definitions are given in the following. The matching discriminant definition is:

$$D(\text{CDA}, \Delta T) = [1 - p(\text{CDA})] \cdot [1 - p(\Delta T)] \ , \tag{3.1}$$

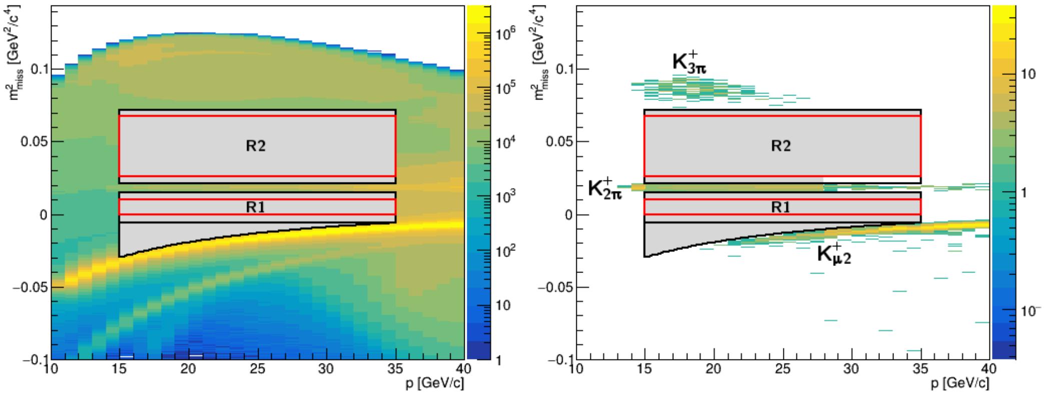

Figure 3.2: Left: squared missing mass vs momentum for the 2017 data set before the selection; the $K^+_{\mu 2}$, $K^+_{2\pi}$ and $K^+_{3\pi}$ regions are clearly visible. Right: squared missing mass vs momentum after the full $\pi\nu\nu$ selection. In both plots, the signal and control regions have been covered by, respectively, red and black boxes in order to perform a blind analysis.

where $p(\text{CDA})$ and $p(\Delta T)$ are the cumulative distributions of the CDA and ΔT:

$$p(\text{CDA}) = \frac{1}{N^{\text{Norm}}_{\text{CDA}}}\left[\int_0^{\text{CDA}} f(\text{CDA}')\,\text{dCDA}'\right] \tag{3.2}$$

$$p(\Delta T) = \frac{1}{N^{\text{Norm}}_{\Delta T}}\left[\int_0^{|\Delta T|} 2\cdot f(|\Delta T'|)\,\text{d}|\Delta T'|\right] . \tag{3.3}$$

In the equations above, $f(\text{CDA})$ and $f(\Delta T)$ are the probability density functions (PDFs) of CDA and ΔT, $N^{\text{Norm}}_{\text{CDA}}$ and $N^{\text{Norm}}_{\Delta T}$ are normalization factors evaluated in $\text{CDA} \in (0, 100)$ mm and $\Delta T \in (-0.95, 0.95)$ ns. The PDFs are evaluated from $K^+ \to \pi^+\pi^+\pi^-$ decays in the control trigger:

$$\begin{aligned} f(\text{CDA}) =&0.25\cdot e^{-0.5\cdot\left(\frac{\text{CDA}}{1.27}\right)^2} + 0.039\cdot e^{-0.5\cdot\left(\frac{\text{CDA}}{2.23}\right)^2} + \\ &0.0033\cdot e^{-0.145\cdot\text{CDA}} - 4.6\cdot 10^{-4} + 1.5\cdot 10^{-5}; \end{aligned} \tag{3.4}$$

$$f(\Delta T) = 0.027\cdot e^{-0.5\cdot\left(\frac{\Delta T}{0.13}\right)^2} + 0.0017\cdot e^{-0.5\cdot\left(\frac{\Delta T}{0.23}\right)^2} . \tag{3.5}$$

Another discriminant (D_{RICH}), similar to the one just described, can be built using $\Delta T_{\text{RICH}} = T_{\text{GTK}} - T_{\text{RICH}}$; both the KTAG and the RICH discriminant are used in the analysis, in order to reinforce the $K^+ - \pi^+$ association.

The PDF used for the $\Delta T_{\rm RICH}$ is:

$$f(\Delta T_{\rm RICH}) = 0.026 \cdot e^{-0.5\cdot\left(\frac{\Delta T}{0.141}\right)^2} + 0.001 \cdot e^{-0.5\cdot\left(\frac{\Delta T}{0.279}\right)^2} \; . \qquad (3.6)$$

The $K^+ - \pi^+$ association is successful if the following conditions are met:

- at least one of the two discriminants D and $D_{\rm RICH}$ is greater than 0.03;
- $D > 0.005$;
- $D_{\rm RICH} > 0.005$;
- $|T_{\rm GTK} - T_{\rm KTAG}| < 0.6$ ns.

The distribution of the KTAG discriminant $D(\mathrm{CDA}, \Delta T)$ is shown in fig. 3.4, along with the plot of the CDA vs ΔT.

A set of cuts is applied in order to reject a multi-track topology where multiple tracks are reconstructed both in GTK and STRAW: a STRAW track cannot have more than 4 associated GTK tracks; events with more than 2 tracks in the STRAW are rejected and, if there are 2 tracks in the STRAW, they must be both positive and their CDA must be greater than 30 mm. After this rejection, for events with 2 tracks in the STRAW, a matching to KTAG, GTK, RICH, CHOD, LKr, MUV1 and MUV2 is performed to keep only events where the candidates closest to the trigger time in each detector match the same track.

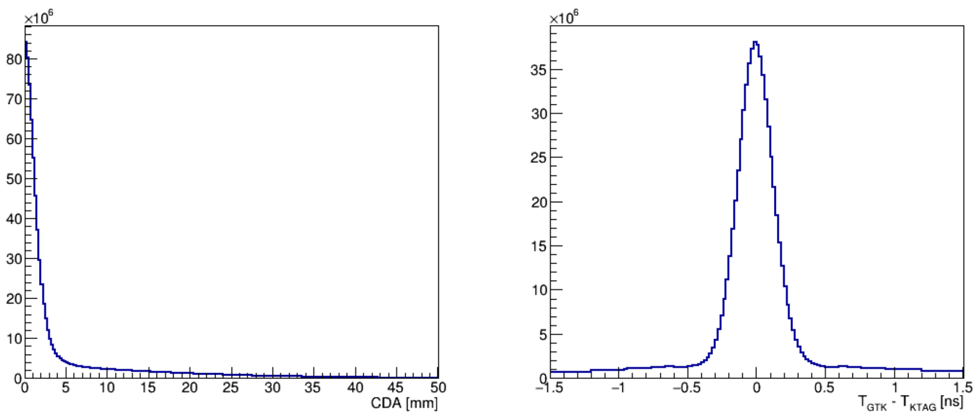

Figure 3.3: CDA and ΔT distributions for events before applying the $\pi\nu\nu$ selection.

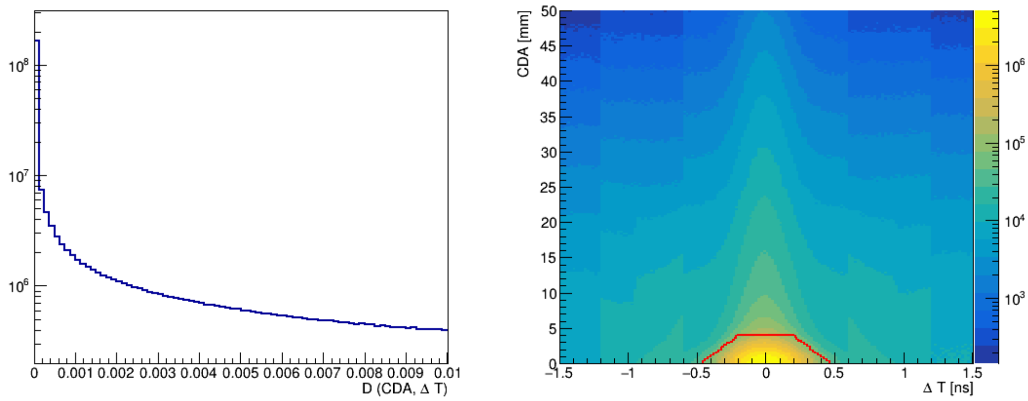

Figure 3.4: Left: Distribution of the KTAG matching discriminant $D(\text{CDA}, \Delta T)$. Right: CDA vs ΔT, the region inside the red line is the one selected by the matching discriminant cut.

3.3.2 RICH Particle Identification

The RICH particle identification is applied in the momentum range $(15, 35)$ GeV/c. Two main RICH variables can be used to reject particles that are not pions, the likelihood and the mass [53].

A π^+ is identified through a likelihood algorithm that extrapolates the track to the RICH mirror predicting the ring center; the algorithm uses the momentum to predict the ring radius and the number of hits for different particle hypothesis (π, μ, e, K) [54]. In fig. 3.5 the ring radius computed by the RICH algorithm is plotted as a function of the momentum of the particle. In the 2017 $K^+ \to \pi^+\nu\bar{\nu}$ selection, the following variable is computed:

$$\mathcal{L}^{!\pi}_{\text{max}} = \max\{\mathcal{L}(e), \mathcal{L}(\mu), \mathcal{L}(K), \mathcal{L}(\text{noise})\} \ , \tag{3.7}$$

where $\mathcal{L}(e, \mu, K)$ is the likelihood for a certain particle hypothesis (electron, muon or kaon) and $\mathcal{L}(\text{noise})$ is the likelihood calculated under the hypothesis that the hits are generated by a uniform distribution due to accidental hits.

Another cut can be applied on the mass computed using the RICH algorithm,

$$M^2_{\text{RICH}} = P^2_\pi \left(\frac{F^2 \cdot n^2}{F^2 + R^2} - 1 \right) \ , \tag{3.8}$$

where $F = 17020$ mm is the focal length of the RICH mirror, n is the refractive index of the neon in the detector, R is the Cherenkov ring radius and P_π is the π^+ momentum as measured by the STRAW spectrometer.

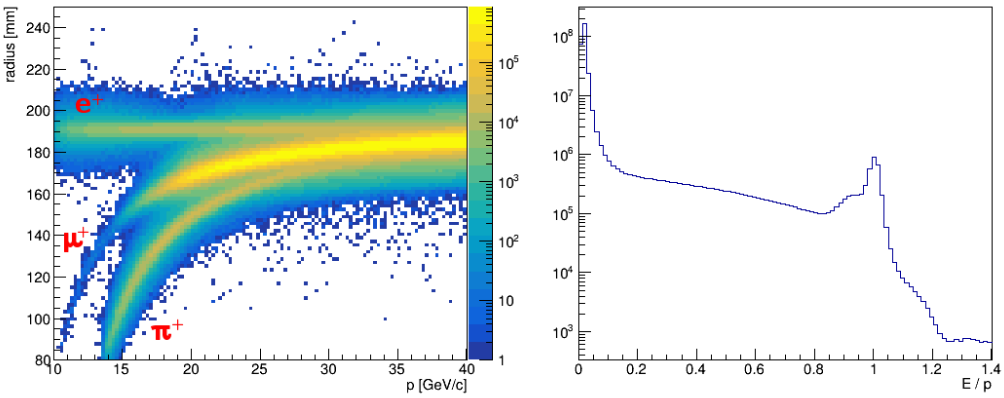

Figure 3.5: Left: ring radius as computed by the RICH algorithm as a function of the track momentum. Right: Ratio between the energy reconstructed by the LKr calorimeter and the momentum of the track.

The particle is positively identified as a π^+ if:

$$\mathcal{L}^{!\pi}_{\text{max}} < 0.12 \;, \tag{3.9}$$

$$125 \text{ MeV/c}^2 < M_{\text{RICH}} < 200 \text{ MeV/c}^2 \;. \tag{3.10}$$

3.3.3 Calorimetric particle identification

The calorimetric particle identification makes use of the information from LKr, MUV1, MUV2 and MUV3 and is optimized to suppress to an acceptable level the μ^+ from $K_{\mu 2}$ decays. The optimization is performed by the MVA implemented in the na62 software framework [55]. A μ^+ in the calorimetric system behave as a minimum ionizing particle (MIP) and is rejected if one of the following conditions is true:

- MUV3 hit in time with CHOD,
- $D_{\text{MIP}} < 1$,
- $Prob(\pi) < \max\{0.7, 0.98 - 0.4596 \cdot e^{-(P_\pi - 11.44)/5.27}\}$;

D_{MIP} is the MIP discriminant that is built according to the average energy of a MIP in LKr, MUV1 and MUV2; Prob(π) is the pion probability computed by the MVA tool. Muons undergoing catastrophic bremsstrahlung and absorbed in the LKr are rejected making use of two variables that define the shape of the shower and that can distinguish between electromagnetic and hadronic showers:

$$R_{\text{seed}} = \frac{E_{\text{seed}}}{E_{\text{cluster}}} \ , \tag{3.11}$$

$$R_{\text{cell}} = \frac{N_{\text{cell}}}{E_{\text{cluster}}} \ , \tag{3.12}$$

where E_{seed} is the energy of the most energetic cell in the cluster, E_{cluster} is the energy of the cluster associated to the track and N_{cell} is the number of cells in the cluster. An electromagnetic shower is identified by at least one of the following conditions:

- $R_{\text{seed}} > 0.2$ and $R_{\text{cell}} \leq 3\ \text{GeV}^{-1}$,
- $R_{\text{seed}} \leq 0.2$ and $R_{\text{cell}} < 1.8\ \text{GeV}^{-1}$,
- $R_{\text{seed}} > 0.35$,
- $R_{\text{seed}} < 0.05$.

The electromagnetic cluster satisfying these criteria is rejected only if $\frac{E_{\text{MUV1}}}{E_{\text{Calo}}} < 0.01$ and $\frac{E_{\text{MUV2}}}{E_{\text{Calo}}} < 0.01$, where E_{Calo} is the total energy in the calorimetric system (LKr, MUV1 and MUV2); if this last condition is not met, the cluster is rejected anyway if $0 < R_{\text{seed}} < 0.8$ and $R_{\text{cell}} < 1.4$.

In order to reject positrons, two additional cuts are applied on the ratio between the energy and the track momentum, requiring $E_{\text{LKr}}/P_{\pi} < 0.8$ and $E_{\text{Calo}}/P_{\pi} < 1.2$ (see fig. 3.5, right).

3.3.4 Photon rejection

The pion defining the downstream track must not have any extra activity associated to it in the downstream detectors participating in the photon veto, therefore any extra activity in LKr, LAV, SAC and IRC is used to reject the event.

As regards the LKr, extra in-time clusters are reconstructed with the standard LKr reconstruction and are taken into consideration only if they are more than 100 mm away from the cluster associated to the pion track.

Moreover, any event with extra hits in LAV, SAC or IRC is rejected by the standard matching tools in the NA62 software framework if the extra activity is within ±3 ns of the track time in the LAV and ±7 ns in the SAV.

3.3.5 Multiplicity rejection

The rejection of events with multiple charged tracks in the final state makes use of the HASC and MUV0, the LKr calorimeter, the hodoscopes and the STRAW spectrometer. The following conditions reject events in which a kaon decays in multiple charged tracks but not all of them are reconstructed in the STRAW, or events with photons interacting with the material before the calorimeter.

- Events with hits in the HASC in time with the track are rejected; these cut suppresses $K_{3\pi}$ decays where one of the π^+ travels inside the beam pipe and is deflected by the magnet after MUV3, releasing a signal in the HASC; alternatively a photon from a π^0 can interact with the material of the beam pipe and convert into an electron-positron pair, with the positron deflected by the magnet after MUV3 into the HASC.

- Events with hits in the MUV0 in time with the track are rejected; this cut rejects $K_{3\pi}$ decays where the π^- decays into a muon and an antineutrino before entering the RICH.

- Further charged multiplicity rejection is achieved combining in-time hits from LKr, CHOD and NewCHOD, asking for in-time activity in at least two out of three detectors in order to reduce the random veto.

- Finally, multiplicity rejection makes use of reconstructed STRAW segments not belonging to the pion track.

3.3.6 Beam background rejection

One of the main residual background to the $K^+ \to \pi^+ \nu \bar{\nu}$ in the NA62 apparatus after the rejection of kaon decays in the fiducial volume is the background originating by early kaon decays before the fiducial region, matched to accidental GTK tracks. The rejection of the upstream background relies on geometrical cuts applied on the impact position of the π^+ track at the first chamber of the STRAW and at the TRIM5 dipole magnet, in-time activity in the CHANTI and track multiplicity in the GTK. The study of the upstream background in the 2017 data is the main topic of my PhD thesis; a detailed description of the features of this background source can be found in chapter 4.

3.3.7 Kinematic selection of signal events

Events in the momentum range between 15 and 35 GeV/c surviving all the cuts described in the sections above, are divided into different kinematic regions. In particular, the squared missing mass m^2_{miss} is used for the definition of signal and control regions. The m^2_{miss} can be computed in three different ways:

$$m^2_{\text{miss}} = (P_K - P_\pi)^2 \ , \tag{3.13}$$

$$m^2_{\text{miss,nom}} = (P_{K,\text{nom}} - P_\pi)^2 \ , \tag{3.14}$$

$$m^2_{\text{miss,RICH}} = (P_K - P_{\pi,\text{RICH}})^2 \ , \tag{3.15}$$

where P_K is the 4-momentum of the kaon measured by the GTK, $P_{K,\text{nom}}$ is the nominal 4-momentum of the beam, P_π is the 4-momentum of the pion measured by the STRAW and $P_{\pi,\text{RICH}}$ is the 4-momentum of the pion measured by the RICH assuming the π^+ mass.

The m^2_{miss} is used for the definition of the signal regions, while the two other missing mass definitions are used to refine the kinematic selection in order to have a better suppression of the background originated by mis-reconstruction of tracks in the STRAW and in the GTK. The definition of the signal region is given in table 3.2, while the definition of the control regions is given in table 3.3; their limits are chosen to be adjacent to the signal regions but still far enough from the background peaking regions, so that they basically contain the non-gaussian part of the background resolution. The lower limit for the $K_{\mu 2}$ control region is based on the analytic formula of the squared missing mass of $K_{\mu 2}$ events when the π^+ mass is assumed,

$$m^2_{\text{kin}-\mu} = (m^2_{\pi^+} - m^2_{\mu^+})\left(1 - \frac{75}{p_\pi}\right) \ , \tag{3.16}$$

and its resolution is $\sigma = 1.2 \cdot 10^{-3}\ \text{GeV}^2/\text{c}^4$, constant in the $15 - 35$ GeV/c momentum range, calculated using $K_{\mu 2}$ MC events.

3.3.8 Background evaluation

As mentioned in the previous sections, the main background sources from kaon decays in the fiducial region are due to the $K^+ \to \mu^+\nu(\gamma)$, $K^+ \to \pi^+\pi^0(\gamma)$, $K^+ \to \pi^+\pi^+\pi^-$ and $K^+ \to \pi^+\pi^-e^+\nu$ decays. While for the last process the m^2_{miss} distribution overlap largely with the signal region R2 (fig. 2.1), the first three decays enter the signal regions only because of mis-reconstruction of the m^2_{miss}. The expected background events entering the signal region, for each background process i, can be computed as

$$N_i^{\text{bkg}} = N_i \cdot f_i^{\text{kin}} \ , \tag{3.17}$$

Signal regions definition			
Signal region	m^2_{miss}	$m^2_{\text{miss,nom}}$	$m^2_{\text{miss,RICH}}$
$R1(p_\pi < 20)$	$0, 0.01$	$-0.005, 0.0135$	$0, 0.01$
$R1(20 \leq p_\pi < 25)$	$0, 0.01$	$-0.005, 0.0135$	$0, 0.02$
$R1(p_\pi \geq 25)$	$0, 0.01$	$0, 0.0135$	$-0.005, 0.02$
$R2$	$0.026, 0.068$	$0.024, 0.068$	$0.02, 0.07$

Table 3.2: Definition of the signal regions R1 and R2. R1 definition depends on the momentum region. The pion momentum p_π is in GeV/c, all the squared missing masses are in GeV^2/c^4. The squared missing masses ranges are given as (m_l^2, m_h^2) and are to be intended as $m_l^2 < m^2 < m_h^2$.

Control regions definition	
$CR1$	$0.01 < m^2_{\text{miss}} < 0.015$
$CR2$	$0.021 < m^2_{\text{miss}} < 0.026$
$CR_{K_{\mu 2}}$	$m^2_{\text{kin}-\mu} + 0.0036 \leq m^2_{\text{miss}} < 0$
$CR_{K_{3\pi}}$	$0.068 \leq m^2_{\text{miss}} \leq 0.072$

Table 3.3: Definition of the control regions. $CR1$ and $CR2$ are control regions for the $K_{2\pi}$ decay, $CR_{K_{\mu 2}}$ is the control region for the $K_{\mu 2}$ background, while $CR_{K_{3\pi}}$ is the control region for $K_{3\pi}$. The definition of the $K_{\mu 2}$ kinematic boundary is given in eq. 3.16. All the squared missing masses are in GeV^2/c^4.

where N_i is the number of events remaining in the corresponding $m^2_{\rm miss}$ region of the decay i after the full $\pi\nu\nu$ selection, and $f_i^{\rm kin}$ is a fraction of background entering the signal region that can be modelled from data using the *tails* in the various background $m^2_{\rm miss}$ distributions. The whole procedure is applied in four equal bins of π^+ momentum, from 15 to 35 GeV/c. The procedure is first applied to predict the background in the control regions, so that the method can be validated and subsequently used to predict the background in the signal regions. The definition of the $m^2_{\rm miss}$ region for the decays is given in table 3.4.

$m^2_{\rm miss}$ regions for different K^+ decays	
$K^+ \to \mu^+\nu_\mu$	$m^2_{\rm kin-\mu} - 0.0060 < m^2_{\rm miss} < m^2_{\rm kin-\mu} + 0.0036$
$K^+ \to \pi^+\pi^0$	$0.015 < m^2_{\rm miss} < 0.02$, $0 < m^2_{\rm miss,RICH} < 0.07$
$K^+ \to \pi^+\pi^+\pi^-$	$m^2_{\rm miss} > 0.072$

Table 3.4: Definition of the background $m^2_{\rm miss}$ regions. The $K_{\mu2}$ analytic expression $m^2_{\rm kin-\mu}$ has been defined in eq. 3.16. You may notice that the boundaries of the missing mass regions are adjacent to the control regions in table 3.3.

As regards the $K^+ \to \pi^+\pi^-e^+\nu_e$ decay, the aforementioned procedure cannot be applied since the multiplicity rejection is correlated to the kinematics; therefore the background induced by this decay is evaluated from MC simulations.

3.3.9 Normalization and Single Event Sensitivity

The Single Event Sensitivity (SES) is defined as

$$\text{SES} = \frac{1}{N_K \cdot \epsilon_{\pi\nu\nu}} \ , \tag{3.18}$$

where N_K is the number of kaon decays in the fiducial region and $\epsilon_{\pi\nu\nu}$ is the signal efficiency. The number of kaon decays can be computed from the number $N_{\pi\pi}$ of $K^+ \to \pi^+\pi^0$ decays in the control trigger as follows:

$$N_K = \frac{N_{\pi\pi} \cdot R}{A_{\pi\pi} \cdot BR_{\pi\pi}} \ . \tag{3.19}$$

In the equation above, the $K^+ \to \pi^+\pi^0$ decays contributing to $N_{\pi\pi}$ are selected with a $\pi\nu\nu$-like selection releasing the photon and multiplicity rejection and requiring a m^2_{miss} in the $K^+ \to \pi^+\pi^0$ peak region; $A_{\pi\pi}$ is the acceptance for this selection, $R = 400$ is the downscaling factor of the control trigger and $BR_{\pi\pi}$ is the branching ratio of the $K^+ \to \pi^+\pi^0$ decay.

The efficiency of the $\pi\nu\nu$ selection can be written as

$$\epsilon_{\pi\nu\nu} = \sum_j A^j_{\pi\nu\nu}\epsilon^j_{\text{trig}}\epsilon^j_{\text{RV}} \ , \tag{3.20}$$

where the sum includes four equal bins j of 5 GeV momentum, $A_{\pi\nu\nu}$ is the signal selection acceptance, ϵ_{trig} is the trigger efficiency and ϵ_{RV} is the random veto efficiency. The random veto efficiency is defined so that $1 - \epsilon_{\text{RV}}$ is the percentage of signal events rejected by the photon and multiplicity cuts as a result of accidental activity in the detector. Other possible effects are either implicit in $A_{\pi\nu\nu}$ or they cancel out when multiplying by N_K to compute the SES, for instance the random veto due to accidental activity in the MUV3.

The expected number of signal events is

$$N^{\text{exp}}_{\pi\nu\nu} = \frac{BR_{\pi\nu\nu}(\text{SM})}{\text{SES}} \ , \tag{3.21}$$

where $BR_{\pi\nu\nu}(\text{SM})$ is the Standard Model expectation for the $K^+ \to \pi^+\nu\bar{\nu}$ decay.

The results of the $\pi\nu\nu$ analysis, along with the background evaluation are reported in chapter 5.

Chapter 4

Upstream Background

The so-called *upstream background* is by far the most dangerous source of background for the measurement of the $K^+ \to \pi^+ \nu\bar{\nu}$ decay at NA62; the study of this background was the main focus of my PhD activity.

4.1 Characteristics of the upstream background

We call upstream background any event originated before the fiducial decay volume that, for any reason, reaches the fiducial volume and survives all the cuts of the signal selection. Upstream background events can be originated either by early decays of K^+ or interactions of beam particles with the material in the beam line, and in particular there are the following main possibilities:

1. the downstream π^+ comes from an early K^+ decay between GTK2 and GTK3, with an accidental pile-up GTK track; the resulting π^+ sneaks through the inner part of the collimator and reaches the fiducial decay volume. This kind of events have been called *snakes* in the jargon of NA62.

2. the downstream π^+ comes from an early K^+ decay between GTK2 and GTK3, with an accidental pile-up GTK track; the resulting π^+ passes above the final collimator and reaches the fiducial decay volume, because of the lack of shielding in front of the central region of the last dipoles. This kind of events are called *mambas* in the jargon of NA62, and the background they originate was partially suppressed in the 2017-II data sample thanks to the shielding installed in September 2017.

3. the downstream π^+ comes from an interaction of a beam particle with GTK2 or GTK3, matched to an accidental K^+ in GTK.

4. the downstream π^+ is promptly produced in inelastic collisions of a beam K^+ with the GTK3.

5. the downstream π^+ comes from the decay of a long-living particle (e.g. K_S, K_L or K^+) produced in inelastic collisions of beam K^+ with the GTK3.

In the following, I will refer to these classification as *type 1*, *type 2*, *type 3*, *type 4* and *type 5* background, in the same order as they are listed above.

In the first three cases there is an accidental track in the GTK (pile-up track) matched to the downstream π^+ and, in particular, in the first two cases the K^+ that originated the downstream π^+ cannot form a track in the GTK because it decayed (or interacted) before the last station.

Various cuts are applied in the $\pi\nu\nu$ analysis to suppress and reject upstream events (see also 3.3.6). For what concerns the first three types of upstream background, the most relevant cuts are:

- $K^+ - \pi^+$ matching cut, that uses the time of KTAG, GTK, RICH and the CDA of the vertex, building the discriminant mentioned in 3.3.1; a full description of the procedure can be found in [56];

- CHANTI veto;

- cut on the fiducial region, performed in the R_{STRAW1} vs Z_{vertex} plane;

- cut on the extrapolated position of the downstream π^+ back at the position of the TRIM5 magnet; the cut rejects a rectangular region in $|X| < 100$ mm and $|Y| < 500$ mm (*box cut*, more on this cut later).

As regards the type 4 and 5 upstream events, where there is an interaction of beam K^+ with the GTK3, the rejection is mainly achieved by the following cuts:

- CHANTI veto, since the interaction producing the π^+ is associated to a high particle multiplicity easily detected by the CHANTI;

- cut on the fiducial region, same as above;

- CDA cut in the $K^+ - \pi^+$ matching;

- box cut at TRIM5, same as above.

The classification of the upstream background into the five groups listed above is backed up by the analysis of a data sample artificially enriched of upstream-like events, relaxing or inverting the cuts against the beam background on the $K^+ \to \pi^+\nu\bar{\nu}$ selection. In particular, the enriched sample passes a $\pi\nu\nu$ selection but the cuts on the Z_{vertex}, CHANTI and the box cut are not applied, while the $K-\pi$ matching cut is inverted. Figure 4.1 shows the distribution of these events at the TRIM5 position, where the events crowd around some regions that indicate that the tracks originated upstream of the GTK3 station enter the fiducial volume depending on the material and stray magnetic field on their path.

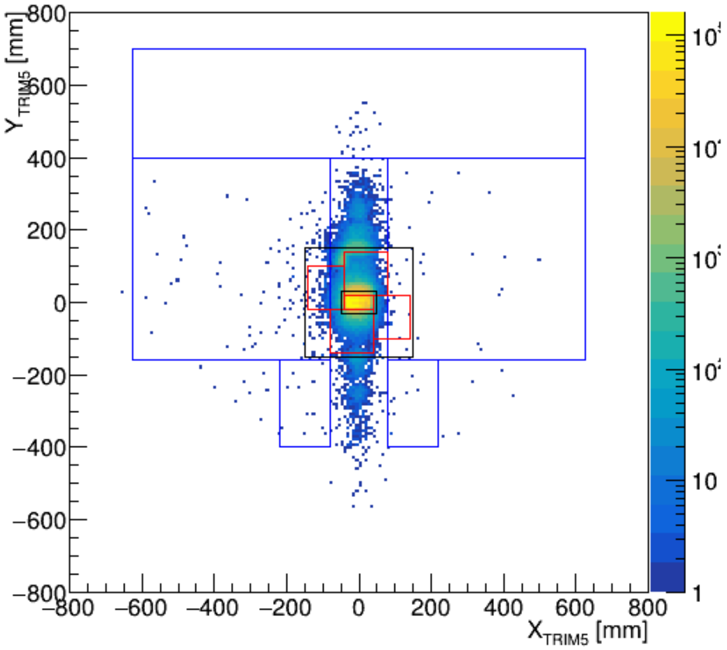

Figure 4.1: Distribution of the extrapolated position of the π^+ track at Z_{TRIM5} for a sample of data enriched with upstream-like events. The blue lines correspond to the region covered by the last dipole and second achromat, the black lines define the acceptance region covered by the CHANTI detector, while the red lines correspond to the contour of the final collimator.

In order to understand how these kind of events can represent a background to our signal, it is useful to refer to the simple sketches in fig. 4.3, 4.4 and 4.5. The standard signal event topology is depicted in fig. 4.3: a K^+ in the beam is detected in the KTAG and in all the three stations of the GTK;

the kaon enters the fiducial region and decays into a charged pion and two neutrinos; then, the downstream π^+ is detected by the STRAW spectrometer and by the other downstream sub-detectors. If the downstream track is extrapolated back at the Z coordinate of the TRIM5 magnet, the signal events are distributed uniformly around a ring centered on the beam pipe (see fig. 4.2), leaving the region of the beam pipe empty because the vertex between the upstream and the downstream track for a signal event is always inside the fiducial volume. This can be better understood looking at the dashed line in fig. 4.3.

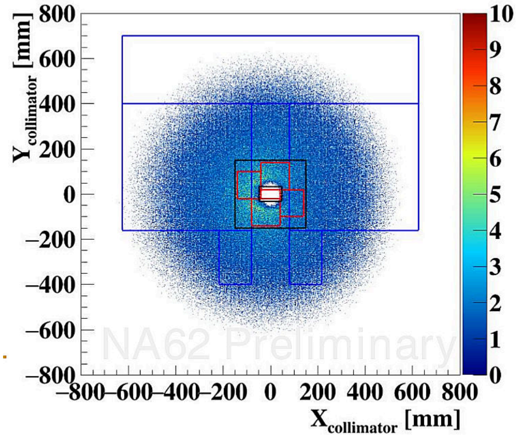

Figure 4.2: MC distribution of the downstream track of signal events extrapolated at the TRIM5 Z-position [57].

For the sake of argument, in the following I will present three possible upstream background scenarios.

- It might happen that a K^+ decays between GTK2 and GTK3 (fig. 4.4). Suppose, for instance, that the decay is a $K^+ \to \pi^+\pi^0$, and the photons from the π^0 decay are lost or absorbed by the material in the beam line. In some special cases, the π^+ in the final state could sneak through the holes in the collimators and reach the fiducial region: if a pile-up π^+ is present in the GTK, then this can form a fake vertex with the pion from the K decay, resulting in a signal-like signature. However, in this kind of events, the extrapolation of the downstream track at the TRIM5 position will result in a distribution very close to the center of the beam, unlike signal events (see fig. 4.1), therefore a geometrical box cut can be applied to get rid of this kind of background.
- A π^+ from an early K^+ decay in the achromat region (see also fig. 2.3), can pass through the aperture of the last dipole of the achromat itself

(since there is no collimation in Y), exiting at a coordinate Y and with a YZ slope such that it can jump above the final collimator, outside the acceptance of the CHANTI, and pass through the return yoke of TRIM5 without interacting (2.5 λ_I); this downstream pion can form a fake vertex in the fiducial region between 130 and 145 m with a pile-up track in the GTK (fig. 4.5). This kind of events, when extrapolated at the TRIM5 plane, are distributed along the vertical direction (see fig. 4.1).

- Alternatively the π^+ from an early event can pass through the cracks of the final collimator, inside the acceptance of CHANTI, and pass through the return yoke of TRIM5 without interacting. In this case the pion will be detected by CHANTI most of the times, but one has to take into account the detector inefficiency. Accidentally, they can make a fake vertex with a pile-up GTK track in the region between 115 and 130 m.

Because of the mechanisms just described, the extrapolated position at TRIM5 for a conspicuous number of upstream background events fall in the region defined by $|X| < 100$ mm and $|Y| < 500$ mm; the events falling into this region were consequently removed in the 2016 analysis (**box cut**) [18]. As mentioned earlier, the same cut is applied in the 2017 analysis, since no significant modification to the beam line was made with respect to the previous year.

All the topologies described would normally be rejected at the analysis level by the beam background cuts listed previously. The real problem arises from the fact that the upstream background tracks could undergo multiple scattering. For instance, if a π^+ from an early kaon decay is scattered at the first chamber of the spectrometer (STRAW1), the pointing of the track is lost, the extrapolation of the track at the TRIM5 position is not reliable anymore and the event may not be rejected by the box cut. In this case, the upstream background events mimic perfectly a signal event. Because of this, it is extremely important to evaluate the residual contribution of the upstream background inside the signal region.

The time structure of the upstream events is manifold and it can be visualized looking at the time coincidence between the three most relevant detectors (see fig. 4.6), i.e. the KTAG, the GTK and the RICH:

- In the case of **early kaon decays**, where the K^+ decays before GTK3, the RICH and KTAG detectors are in time because the downstream π^+ comes from the decay of the K^+; conversely the GTK and the KTAG are not in time, since the signal in the GTK must come from

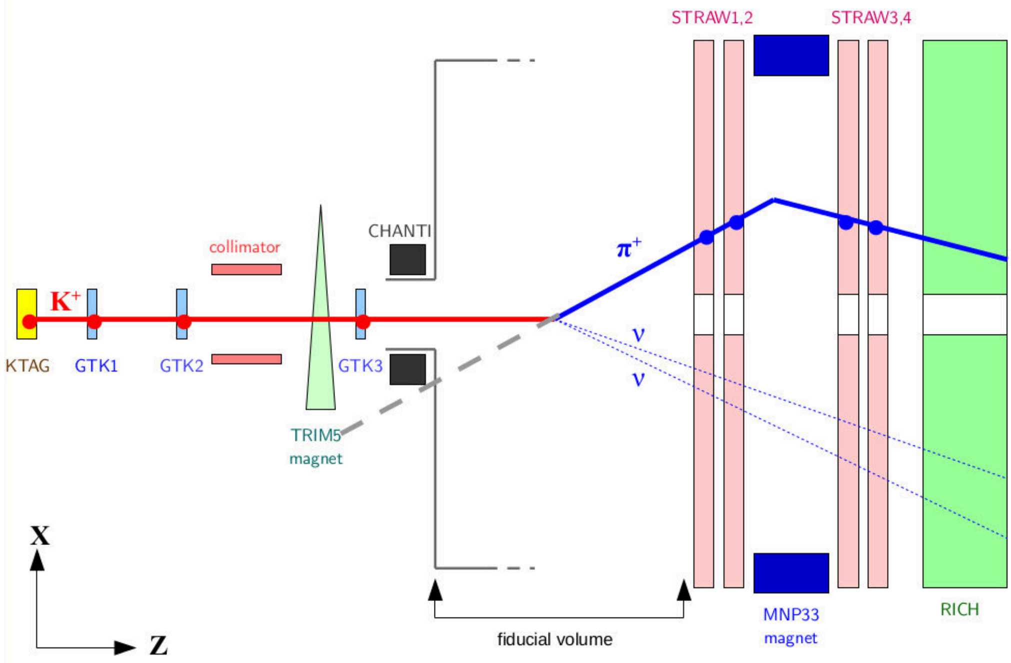

Figure 4.3: A simplified not-to-scale sketch of the NA62 experiment in the XZ plane. In this sketch, the typical topology of a signal event is depicted. The red line represent the beam K^+ decaying into a charged pion (blue solid line) and two neutrinos (blue dotted lines). The direction of the pion track can be extrapolated back (gray dashed line) at the TRIM5 magnet Z position.

an upstream pile-up π^+. Therefore, if one plots the distribution of $T_{\text{RICH}} - T_{\text{KTAG}}$ vs $T_{\text{GTK}} - T_{\text{KTAG}}$, these events will be distributed in the horizontal arm of the plot in fig. 4.6.

- In the case of **interactions**, there are various possibilities:
  - if a π^+ interacts with the GTK2 or GTK3 producing a π^+ (or a long-lived particle) that eventually reaches the decay volume, then a K^+ must be present in the GTK and therefore the GTK and KTAG are in time, but the KTAG and RICH are not (vertical arm of plot 4.6);
  - if a K^+ interacts with the GTK2 and there is a pile-up π^+ in the GTK, then the KTAG and RICH are in time, but KTAG and GTK are not (similarly to the early decay case);
  - if a K^+ interacts with the GTK3 station, all the three detector (KTAG, GTK and RICH) are in time with respect to each other (central part of the plot 4.6).

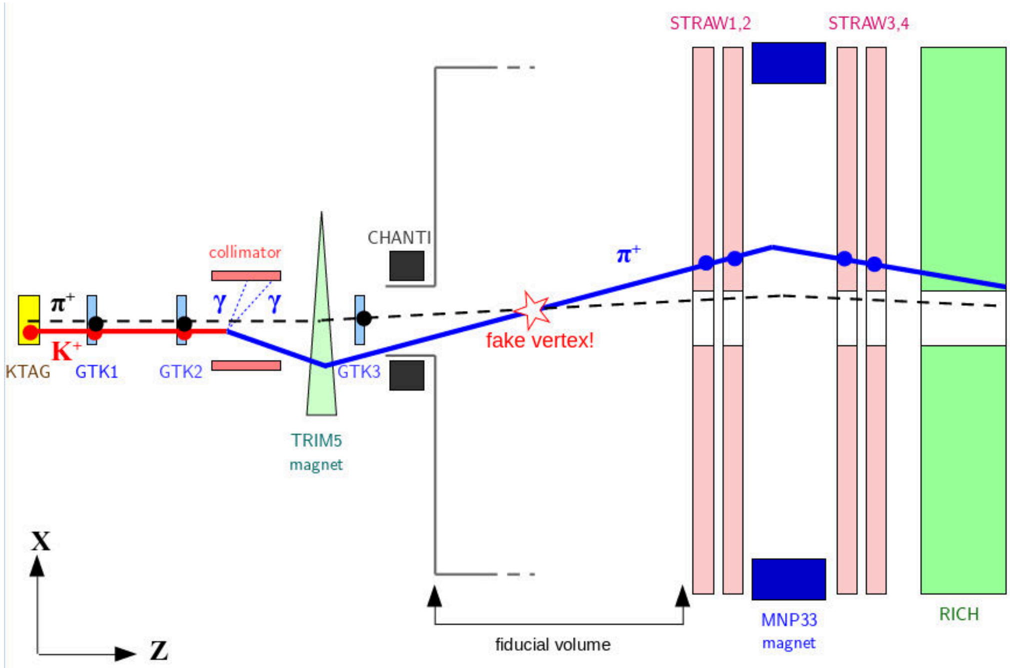

Figure 4.4: Simplified not-to-scale sketch of the NA62 experiment in the XZ plane. A beam K^+ (red line) decays between GTK2 and GTK3 into a π^+ (blue solid line) and a π^0; subsequently the π^0 decays into a pair of photons escaping detection (blue dotted lines). The GTK track is formed by a pile-up beam particle leaving a signal in all the GTK station (black dashed line), forming a fake vertex with the π^+ from the kaon decay.

So far there is no evidence of type 4 or type 5 events (interactions with the GTK): looking at the side-bands of the time distributions in the timing plot shows that the accumulation of events in the central part of the plot can be easily explained just in terms of the vertical and the horizontal arms.

4.2 2016 strategy: the bifurcation analysis

In order to evaluate the upstream background contribution to the signal region, in the 2016 analysis a bifurcation technique was adopted [18][58]. In a bifurcation analysis, two independent cuts are chosen and inverted, obtaining bifurcated samples that are outside of the signal region. The two independent criteria for the bifurcation technique need to be relevant for the background that is the subject of the study: the chosen cut in the 2016 analysis are the $K^+ - \pi^+$ association (hereinafter referred to as *cut1*) and the box cut (hereinafter referred to as *cut2*). Specifically, the $K^+ - \pi^+$ association is the

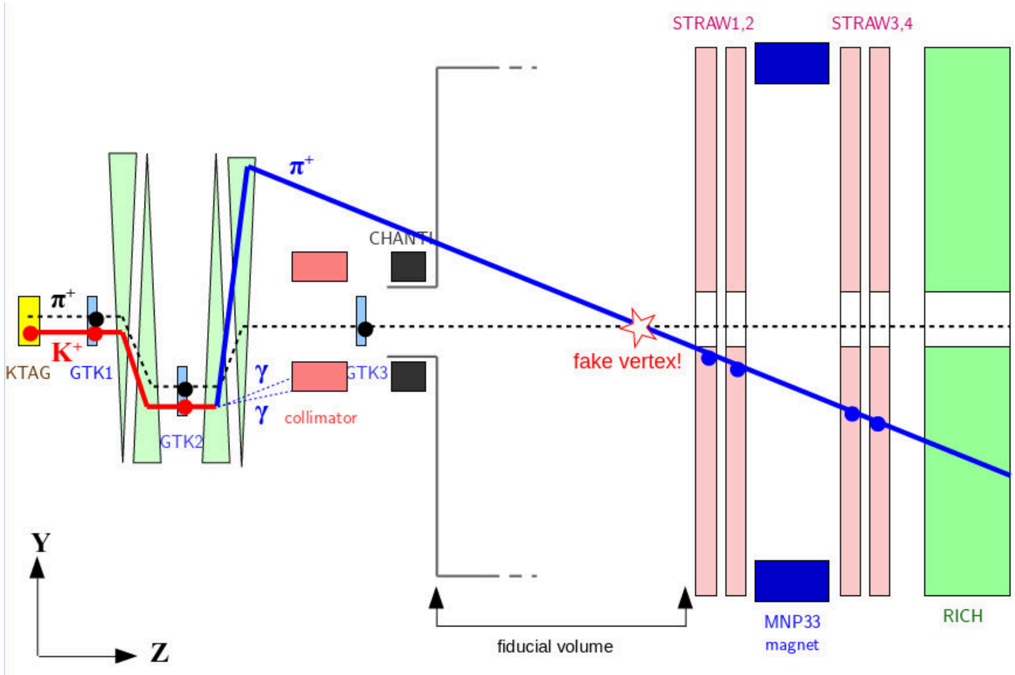

Figure 4.5: Simplified not-to-scale sketch of the NA62 experiment in the YZ plane. In this case a beam K^+ (red line) decays between GTK2 and GTK3 into a π^+ (blue solid line) and a π^0; subsequently the π^0 decays into a pair of photons escaping detection(blue dotted lines). The π^+ enters the decays region from above, jumping over the collimator, and form a fake vertex with a pile-up GTK track.

logical AND of three cuts ($K^+ - \pi^+$ discriminant, timing between KTAG and GTK, and CDA), and cut2 is just the boxcut defined in the previous section.

These two cuts define four sub-samples called A, B, C and D (see fig. 4.7). Sample A is the signal region where cut1 and cut2 are the same as those used in the $\pi\nu\nu$ selection[1]; in sample B the box cut (cut2) is inverted; in sample C the $K^+ - \pi^+$ association (cut1) is inverted; in sample D both cuts are inverted with respect to the $\pi\nu\nu$ selection; for the reader's convenience the bifurcation samples definitions are summarized in table 4.1.

In order to exploit the bifurcation technique, two essential conditions must be met: the criteria cut1 and cut2 must be uncorrelated and all the

[1]It is important to keep in mind that region A is the signal region, i.e. the combination of the two regions R1 and R2 defined in section 3.3. For this reason it is not possible to look into region A until the analysis is complete, since we decided to go for a blind analysis.

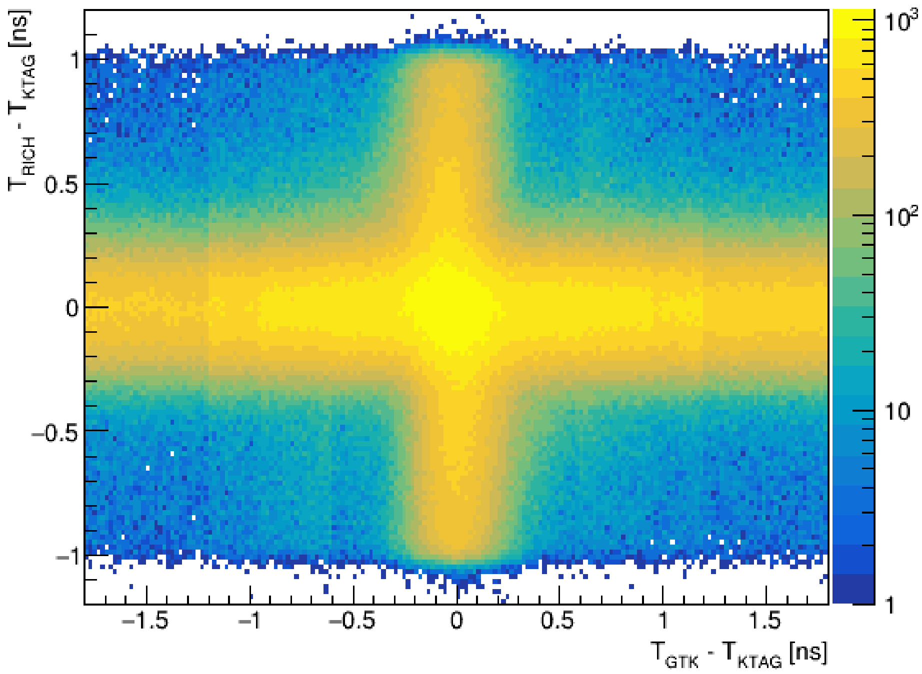

Figure 4.6: Distribution of upstream background-like events in $T_{\text{RICH}} - T_{\text{KTAG}}$ vs $T_{\text{GTK}} - T_{\text{KTAG}}$, times in ns. The sample shown in the plot has been enriched with upstream events.

events in the bifurcated samples B, C and D must be of the same nature. If these two assumptions are valid, then the expected upstream background in region A is related to the number of events observed in the bifurcated samples by the following simple equation:

$$A_{\text{exp}} = \frac{B \cdot C}{D} \tag{4.1}$$

Indeed, if N_0 is the total number of events before applying the criteria cut1 and cut2, and $P(\text{cut}i)$ is the probability that an event satisfies the criterium cut$i$, then

$$A_{\text{exp}} = N_0 P(\text{cut1} \cap \text{cut2}) = N_0 P(\text{cut1}) P(\text{cut2}) \tag{4.2}$$

because of the uncorrelation between cut1 and cut2. Exploiting the definition of the bifurcation samples,

$$B = N_0 P(\text{cut1}) P(\overline{\text{cut2}}) \tag{4.3}$$

A (signal region)	(good matching) × (out of box)
B	(good matching) × (in box)
C	(bad matching) × (out of box)
D	(bad matching) × (in box)

Table 4.1: Definition of the bifurcation analysis sub-samples. All the sub-samples pass a $\pi\nu\nu$ selection, the only difference is in the way the $K^+ - \pi^+$ matching and the box cut are applied.

$$C = N_0 P(\overline{\text{cut1}}) P(\text{cut2}) \tag{4.4}$$

$$D = N_0 P(\overline{\text{cut1}}) P(\overline{\text{cut2}}) \tag{4.5}$$

one can easily demonstrate the validity of equation 4.1.

The method can be validated redefining the bifurcation samples, as shown in fig. 4.7. The two independent criteria are varied, so that the new bifurcation samples B', C' and D' are consistent with the previous ones. In this way, new samples B", C" can be used to evaluate the expected background in a new control region A'. For the new samples, the following relations hold:

$$A_{\text{exp}} = \frac{B' \cdot C'}{D'} \tag{4.6}$$

$$A'_{\text{exp}} = \frac{B'' \cdot C''}{D'} = A'_{\text{obs}} \tag{4.7}$$

where the control region A' can be opened[2] (A'_{obs}) since it is completely separated from the signal region A.

In the case that more than one background source is present, e.g., let's say, there are two background sources called u and v ($N_0 = N_u + N_v$), the basic assumption under which this model is built does not hold, but some relations between the samples can still be defined. In general, two different backgrounds will have different survival probabilities for the two cuts and this introduces a cross term in the equations. In this case, if one defines $\Delta_{\text{cut1}} = P_v(\text{cut1}) - P_u(\text{cut1})$ and $\Delta_{\text{cut2}} = P_v(\text{cut2}) - P_u(\text{cut2})$, equation 4.1 becomes:

$$A_{\text{exp}} = \frac{B \cdot C}{D} + \frac{N_u N_v}{D} \Delta_{\text{cut1}} \Delta_{\text{cut2}} \ . \tag{4.8}$$

[2]As opposed to the signal region A that is kept *closed* because of the blind analysis strategy adopted.

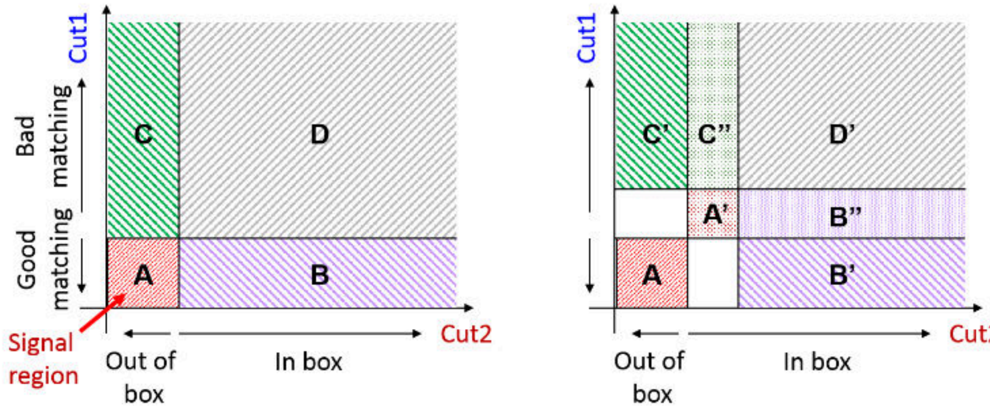

Figure 4.7: Representation of the bifurcation technique. On the left hand side, cut1 and cut2 define the signal region A and the bifurcation samples B, C and D, which can be used to evaluate the expected events in A. On the right hand side, the validation procedure is shown: the two criteria cut1 and cut2 are slightly varied in order to obtain new samples B', C' and D', consistent with the previous samples. At the same time, regions B'', C'' and D' can be used to evaluate the expected background in the control region A'. Illustration taken from [59].

The main problem here is that equation 4.8 can be evaluated only either opening the signal region or using a Monte Carlo simulation[3].

4.3 Limitations of the bifurcation analysis in 2017 data

The evaluation of the upstream background in 2017 is definitely trickier than in 2016. While the 2016 analysis was very meticulous and the results concerning the upstream background rely on reasonable assumptions, it is worth noticing that the statistics in 2016 was so low that the presence of different upstream background sources or other small differences with respect to the model were hardly noticeable.

In particular, with regards to the upstream background studies, the main features of 2017 data which differ with respect to 2016 are the higher statistics

[3]A third way would be to rearrange eq. 4.8 in a way that it depends only on the total number of events N_0 and not on the number of events in the signal region. However this is obviously equivalent to implicitly opening the signal box, therefore it is not an acceptable solution for this analysis.

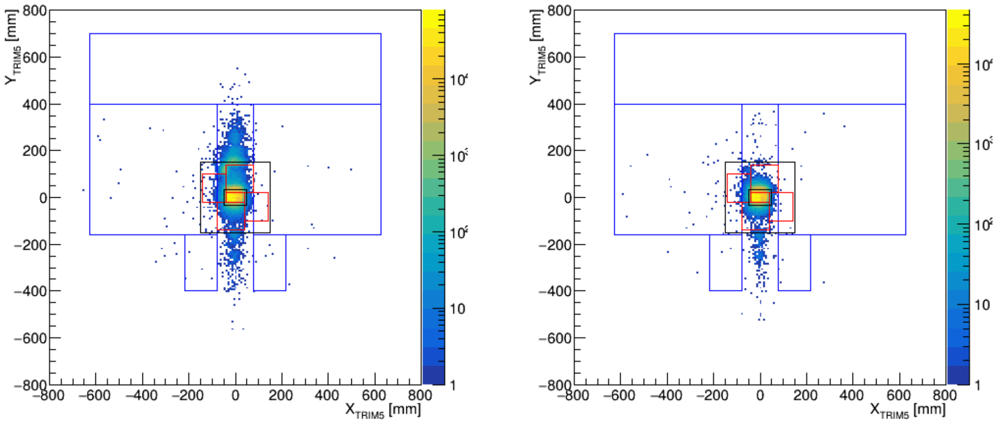

Figure 4.8: Left: extrapolation of the downstream π^+ track in the (X,Y) plane at the TRIM5 Z-position for the data sample 2017-I (before the insertion of the plug). The events pass a $K^+ \to \pi^+ \nu \bar{\nu}$ selection but with an inverted $K^+ - \pi^+$ association. The cuts on CHANTI, the fiducial volume and the box cut are not applied. Right: same plot but for events in the 2017-II sample, after the insertion of the copper plug that removes almost completely the type 2 upstream events. It is worth mentioning that the 2017-II sample is ~ 2 times smaller than 2017-I.

and the presence of the copper plug in the last period of the data taking (fig. 3.1). Therefore, data collected in 2017 were split into two main sets that I will call 2017-I (before the insertion of the plug) and 2017-II (after the insertion of the plug)[4]. The results of the upstream background analysis on the 2017 data sample is given in the following.

The first data sample analyzed was 2017-I, since it is the largest one and the most similar to the data taking conditions of 2016, while 2017-II is the only sample of 2017 with the copper plug inserted, providing important information on the structure of the background itself. Plots in figure 4.8 show the clear effect of the copper plug, and they demonstrate the geometrical origin of type 2 events, suppressed by the plug in the 2017-II data.

In the following, I will give an argument to demonstrate that the bifurcation technique used for the 2016 analysis cannot be applied to 2017 data. In order to do this, I will compute the results of the bifurcation analysis in 2017-I and extrapolate from there to 2017-II, comparing the expectation to

[4]Actually two additional sub-samples are present. Their contribution is taken into account in the final result, although it is pretty negligible for the arguments I will make in the following.

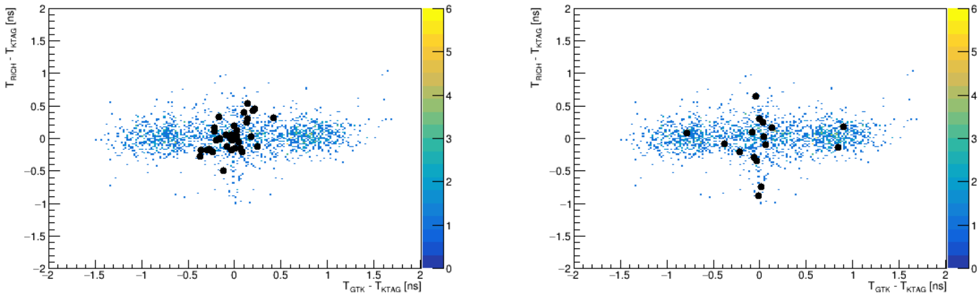

Figure 4.9: Left: time distributions of events in the bifurcation samples B (black circles) and D (colored dots) for the 2017-I period. Right: same plot for sample C (black circles) and D (colored dots).

the observed numbers.

Before computing the results of the bifurcation analysis, it is interesting to look at the time and geometrical distributions of the different bifurcation sub-samples B, C and D for 2017-I events. The time distribution is shown in figure 4.9 : from these distributions, it is clear that sample D is dominated by accidental associations between upstream and downstream tracks; sample B and C look accidental too, though the low statistics does not allow for conclusive statements. Figure 4.10 shows the geometrical distribution of extrapolated tracks at TRIM5.

In 2017-I, the number of events observed in the bifurcation sub-samples are $B = 34$, $C = 16$ and $D = 1816$. Assuming the bifurcation technique can be used, the number of upstream background events expected in the signal region A are:

$$A^{2017\text{-I}} = \frac{B \cdot C}{D} = 0.30^{+0.10}_{-0.09} \,. \tag{4.9}$$

Moving to the 2017-II sample, the time distribution is shown in figure 4.11. Although the statistics is significantly lower than in 2017-I, looking at these distributions the events still look quite accidental at first glance. The geometrical distributions of the extrapolation at TRIM5 (figure 4.12) does not show particular features with respect to 2017-I, except for the suppression of type 2 events at positive Y due to the copper plug. Since I am interested in validating the technique and understanding better the features of the upstream background, I will not compute the expected background events in the 2017-II data set, as I have just done for the 2017-I one, and I will follow a different path. I will try to do an educated guess on the number of events expected in the bifurcation samples in 2017-II, knowing the number of events observed in 2017-I. Of course a discrepancy is expected between

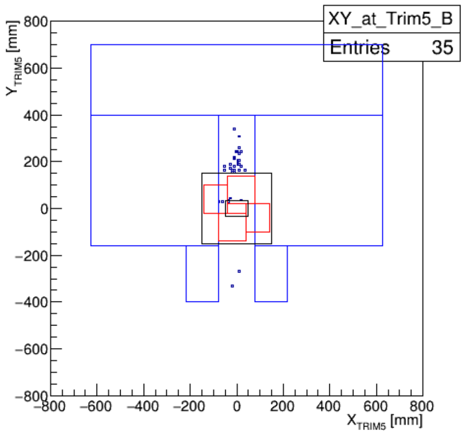

(1) Sample B

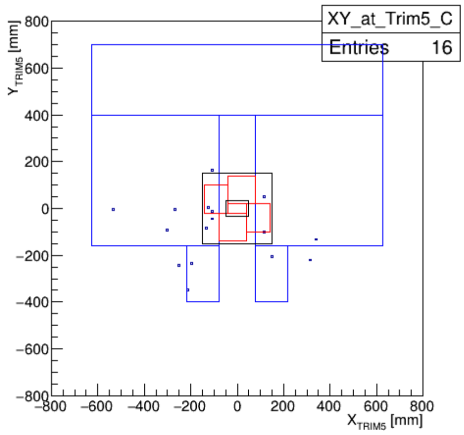

(2) Sample C

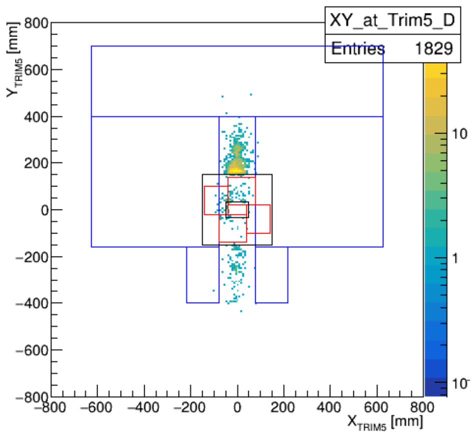

(3) Sample D

Figure 4.10: Extrapolation in the (X,Y) plane of the downstream π^+ track at the TRIM5 Z-position for events in the bifurcation samples B, C and D for the 2017-I period.

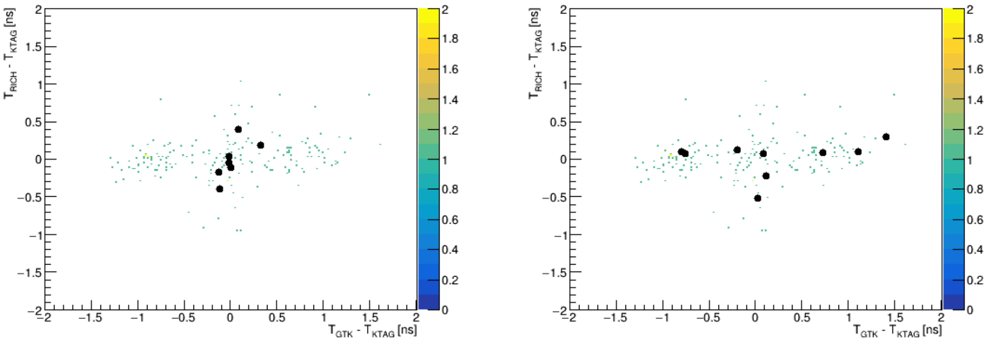

Figure 4.11: Left: time distributions of events in the bifurcation samples B (black circles) and D (colored dots) for the 2017-II period. Right: same plot for sample C (black circles) and D (colored dots). Both sample B and C are compared to sample D since D has a much higher statistics and having it in the background of the plots makes clearer how the low-statistics sample B and C are distributed.

the expected and observed events in 2017-II, because there is a fundamental difference between the two periods, that is the copper plug.

	B	**C**	**D**	$N_{\pi^+\pi^0}$
2017-I	34	16	1816	33×10^6
2017-II	7	9	184	19×10^6

Table 4.2: Number of events in the bifurcation samples B, C and D for the 2017-I and 2017-II periods. The number of $K^+ \to \pi^+\pi^0$ is also shown.

In order to extrapolate from 2017-I to 2017-II, a scaling factor is needed; a reasonable choice is the number of $K^+ \to \pi^+\pi^0$ decays. All the relevant numbers for the following calculation are shown in table 4.2. The number of events in sample D expected in 2017-II (if the plug was not there) are:

$$D_{\text{exp}}^{\text{2017-II}} = D_{\text{obs}}^{\text{2017-I}} \cdot \frac{N_{\pi^+\pi^0}^{2017-II}}{N_{\pi^+\pi^0}^{2017-I}} = 1816 \cdot \frac{19}{33} \sim 1000 \,, \tag{4.10}$$

which is roughly 6 times more than the observed number (184). As already stated, there is no particular concern in this discrepancy since we are not taking into account the effect of the plug in the calculation and we can

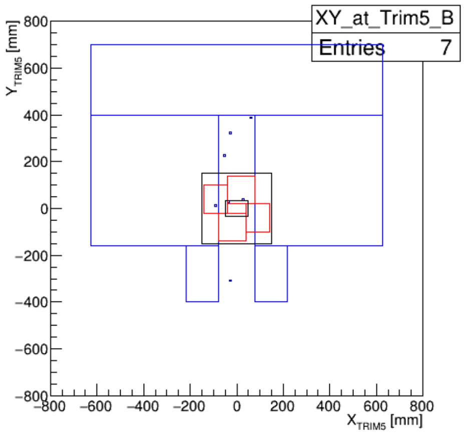

(1) Sample B

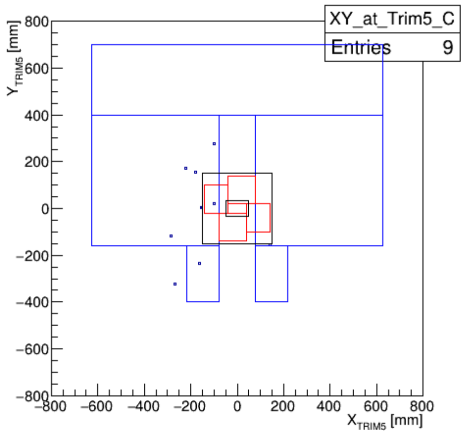

(2) Sample C

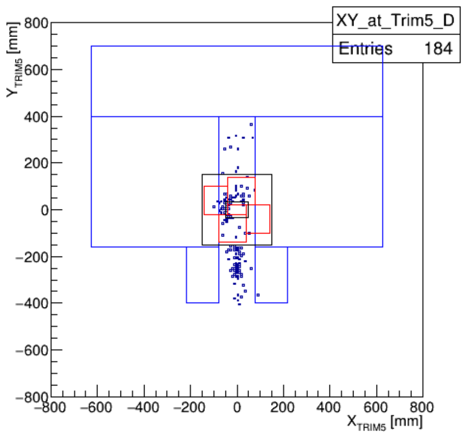

(3) Sample D

Figure 4.12: Extrapolation in the (X,Y) plane of the downstream π^+ track at the TRIM5 Z-position for events in the bifurcation samples B, C and D for the 2017-II period.

assume that the suppression factor is purely due to the plug. Moving to sample B, the expected events in 2017-II are:

$$B^{\text{2017-II}}_{\text{exp}} = B^{\text{2017-I}}_{\text{obs}} \cdot \frac{N^{2017-II}_{\pi^+\pi^0}}{N^{2017-I}_{\pi^+\pi^0}} = 34 \cdot \frac{19}{33} \sim 20 \ , \tag{4.11}$$

that is approximately a factor 3 more than the number of events observed (7). Again, a discrepancy is expected because of the plug; while the difference in the suppression factors between samples B and D is odd, it could still be understood taking into account the very low statistics of sample B in both the periods.

Things get interesting when moving to sample C, where performing the same calculation one obtains:

$$C^{\text{2017-II}}_{\text{exp}} = C^{\text{2017-I}}_{\text{obs}} \cdot \frac{N^{2017-II}_{\pi^+\pi^0}}{N^{2017-I}_{\pi^+\pi^0}} = 16 \cdot \frac{19}{33} \sim 9 \ , \tag{4.12}$$

which is exactly the number of events observed in sample C in 2017-II: events in C seems to be totally unaffected by the presence of the copper plug. This conclusion is paramount: events in sample C are fundamentally different from events in sample B or D and, in particular, the plug that is specifically built to remove type 2 events does not have any effect on the events in C.

Consequently, one of the two key assumptions upon which the bifurcation analysis is built does not hold anymore and a new method to evaluate the upstream background must be found. Even if one could recover in some way the bifurcation analysis, a new method for the upstream background evaluation is mandatory, because the bifurcation analysis cannot be applied in any meaningful way in the 2018 data sample; the reason is that in 2018 a new collimator was installed, and this collimator gets rid of most of the upstream events[5] in the bifurcation samples (more on this topic in section 4.6). Trying to apply the bifurcation analysis in 2018 data would result in numbers with uncertainties that are too large for our purposes.

4.4 Evaluation of the upstream background in 2017 data

The new method I will discuss in the following relies on the evaluation of the probability that a downstream track is associated to an upstream track[6]. The

[5]The collimator is particularly effective against type 2 events.

[6]It is important to mention that this method was first presented by me to the NA62 Collaboration in a simplified version, and then developed further by R. Marchevski to include a dependence on ΔT.

number of expected upstream background events ($N_{\text{up-bkg}}$) can be written as the product of the number of events with a downstream π^+ originating upstream ($N_{\pi^+}^{\text{upstream}}$) times the probability that the downstream π^+ is matched to an accidental GTK track (p_{mistag}):

$$N_{\text{up-bkg}} = N_{\pi^+}^{\text{upstream}} \cdot p_{\text{mistag}} \ . \tag{4.13}$$

The aforementioned probability, in turn, can be written as

$$p_{\text{mistag}} = p_{\text{pile-up}}^{\text{reco}} \cdot p_{K-\pi}^{\text{matching}} \ , \tag{4.14}$$

where $p_{\text{pile-up}}^{\text{reco}}$ is the probability that the track is reconstructed and survives the pile-up treatment, and $p_{K-\pi}^{\text{matching}}$ is the probability that the reconstructed track is matched to a downstream π^+. Therefore, the expected number of upstream background events is

$$N_{\text{up-bkg}} = N_{\pi^+}^{\text{upstream}} \cdot p_{\text{pile-up}}^{\text{reco}} \cdot p_{K-\pi}^{\text{matching}} \ . \tag{4.15}$$

The product of the first two terms defines the number of accidental upstream events and is something very similar to what can be found in the bifurcation sample C, though not quite the same[7], therefore I will call this term N_C:

$$N_{\text{up-bkg}} = N_C \cdot p_{K-\pi}^{\text{matching}} \tag{4.16}$$

Given the definition of N_C, a way to evaluate it is to count the events passing a $\pi\nu\nu$ selection but with a $CDA > 4$ mm.

For the sake of simplicity, from now on I will refer to the last term in eq. 4.16 ($p_{K-\pi}^{\text{matching}}$) as *mismatch probability*. This probability can be evaluated with several methods, I will evaluate it from MC distributions of accidental upstream events. In particular, for the evaluation of the mismatch probability, the PDFs of all the relevant variables used in the $K^+ - \pi^+$ matching are needed, i.e. the CDA and the time of KTAG, GTK and RICH. The CDA distribution of upstream events has a limited statistics, since the MC tools needed had just been developed and tested by the NA62 Geant4 beam line working group at the time of writing this thesis (fig. 4.14); I chose to fit the distribution with a fourth grade polynomial, after comparing the goodness of the fit (χ^2) with other hypothesis. The CDA distribution I used is the one for type 1 events (snakes), since they are by far the main contribution to the sample N_C; indeed I demonstrated in 4.3 how sample C does not contain type 2 events (mambas), and interactions are either suppressed by the kinematics

[7]It is important to keep in mind that sample C contains events that are inside the box cut (like the signal) but are rejected by the matching discriminant cut.

(type 3) or simply not noticeably present (type 4 and 5, as shown at the beginning of the chapter). The time distributions have been generated by me considering gaussian PDFs for KTAG and RICH, with a sigma compatible with the time resolution taken from data, and using a uniform distribution in a ± 1.2 ns time window for the GTK, compatible with the time distribution of pile-up tracks at that time window. In particular, the time of the three detectors was generated according to the following distributions (see also fig. 4.13):

- KTAG: gaussian with $\mu = 0$ and $\sigma = 75$ ps;
- GTK: uniform between -1.2 and 1.2 ns;
- RICH: gaussian with $\mu = 0$ and $\sigma = 95$ ps.

Once the distributions are defined, it is possible to generate random points in the CDA vs ΔT (or ΔT_{RICH}) plane, as shown in fig. 4.14; then, those points can be used to compute the kinematic discriminants $D(\text{CDA}, \Delta T)$ and $D_{\text{RICH}}(\text{CDA}, \Delta T_{\text{RICH}})$.

The mismatch probability is the fraction of events selected by the $K^+ - \pi^+$ matching procedure described in 3.3.1 applied in the same way as in the $\pi\nu\nu$ analysis. Indeed, these events have been specifically generated to be accidental in time and with a CDA distribution consistent with an accidental-events topology, therefore they "should" be rejected by the $\pi\nu\nu$-like matching discriminant cut; if they are not rejected, they contribute to a *mismatched* sample.

The expected number of upstream background events in the signal region is:

$$N_{\text{up-bkg}} = \int_0^{0.6\text{ns}} N_C(|\Delta T|) \cdot p_{K-\pi}^{\text{matching}}(|\Delta T|) \cdot f_{\text{scale}} \, \mathrm{d}(|\Delta T|) \tag{4.17}$$

which is discretized in bins of $|\Delta T|$ as

$$N_{\text{up-bkg}} = \sum_{|\Delta T|} N_C(|\Delta T|) \cdot p_{K-\pi}^{\text{matching}}(|\Delta T|) \cdot f_{\text{scale}} \ . \tag{4.18}$$

In the formula above, f_{scale} is a scaling factor that has to be introduced to correct for the events rejected by the $CDA > 4$ mm requirement in the definition of the sample N_C. This scaling factor can be evaluated from the fraction of events with CDA < 4 mm in the CDA vs ΔT plot generated from the MC; this increases the value of $N_{\text{up}-\text{bkg}}$ of $\sim 10\%$.

The values of the mismatch probability and the number of events N_C are listed for each bin of $|\Delta T|$ in table 4.3. The statistical uncertainty on the mismatch probability is of the order of $\sim 2\%$ while the uncertainty on f_{scale} is negligible.

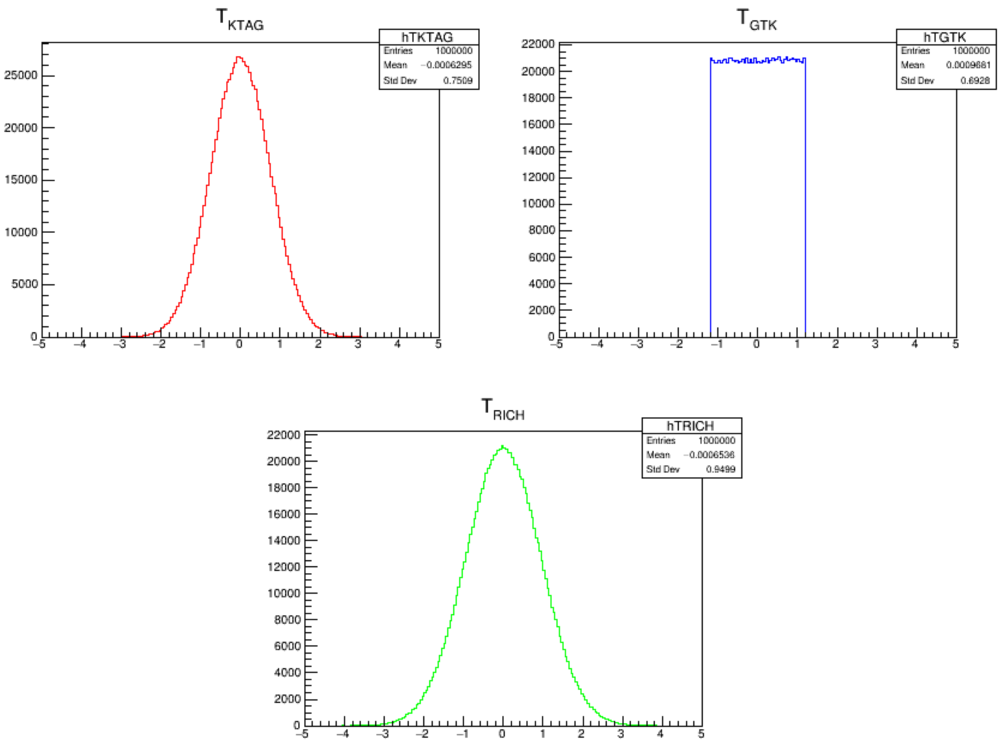

Figure 4.13: Random time values generated for KTAG, GTK and RICH. The KTAG and RICH times take into account the respective time resolutions, while the GTK times are distributed uniformly in $(-1.2, 1.2)$ ns.

4.5 Validation of the method

The method presented above can be validated in a simple way using control sub-samples of data dominated by a specific component of the background. Following the definition of the bifurcation samples, we can define four sub-samples with these characteristics:

B1 good $K^+ - \pi^+$ matching and extrapolation of the π^+ track at TRIM5 inside a box defined by $|X| < 100$ mm and $|Y| < 140$ mm;

B2 good $K^+ - \pi^+$ matching and extrapolation of the π^+ track at TRIM5 inside a box defined by $|X| < 100$ mm, $|Y| > 140$ mm and $|Y| < 500$ mm;

D1 bad $K^+ - \pi^+$ matching and extrapolation of the π^+ track at TRIM5 inside a box defined by $|X| < 100$ mm and $|Y| < 140$ mm;

D2 bad $K^+ - \pi^+$ matching and extrapolation of the π^+ track at TRIM5 inside a box defined by $|X| < 100$ mm, $|Y| > 140$ mm and $|Y| < 500$ mm.

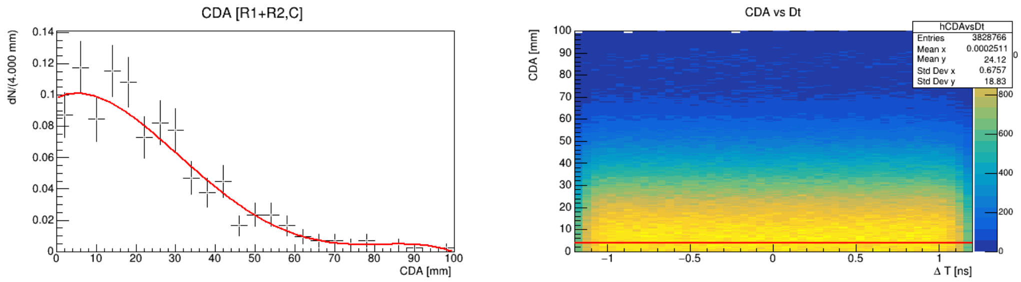

Figure 4.14: Left: fitted Monte Carlo CDA distribution of type 1 upstream events (normalized) coming from a true $Z_{\text{vertex}} < 100$ m. Right: MC-generated points in the CDA vs ΔT plane, according to the CDA distribution on the left and requiring that the KTAG and GTK association is accidental.

The modified box cuts upon which the definition of these subsamples relies are depicted in figure 4.15. Because of this classification, sample D1 is dominated by type 1 events (snakes) while D2 is dominated by type 2 events (mambas). Since events in sample D2 are particularly abundant, the CDA distribution of type 2 events can be directly measured from data; the mismatch probability and the CDA of type 2 events is shown in fig. 4.16, while the time distributions of events in B2 and D2 are shown in fig. 4.17. Finally, the same distributions for events in B1 and D1 are reported in fig. 4.18.

Sample B1 (B2) is to D1 (D2) as sample N_C is to the signal region A; we can estimate the number of expected upstream background events in region A using the events N_C weighted with the suppression coming from the $K^+ - \pi^+$ matching, that comes from the shapes of the CDA and ΔT of the events in the sample. Therefore, a way to validate the method is to predict the correct number of events in B1 and B2 using the number of events in D1 and D2, respectively, and applying the mismatch probability of the relevant type of events.

In particular, the mismatch for type 1 is the same used for the evaluation of the upstream background and relies on MC simulations, since sample D1 does not have enough statistics, while the mismatch for type 2 events is the one shown in fig. 4.16 and is measured from data.

The validation procedure predicts $N_{\text{B1}}^{\text{exp}} = 8.2 \pm 0.9$ events in B1 and $N_{\text{B2}}^{\text{exp}} = 36 \pm 2$ events in B2; these results have to be compared to the events observed in B1 and B2 that are 12 ± 3 and 40 ± 6, respectively. The validation procedure is consistent within the error dominated by the statistics in data. As I mentioned before, better results will be achieved as soon as a more substantial MC sample of upstream events will be

$\lvert\Delta T\rvert$ bin	$N_C(\lvert\Delta T\rvert)$	$p_{K-\pi}^{\text{matching}}(\lvert\Delta T\rvert)$
$[0.00, 0.04]$	2	0.0972
$[0.04, 0.08]$	2	0.0919
$[0.08, 0.12]$	3	0.0833
$[0.12, 0.16]$	2	0.0754
$[0.16, 0.20]$	1	0.0633
$[0.20, 0.24]$	1	0.0521
$[0.24, 0.28]$	1	0.0387
$[0.28, 0.32]$	0	0.0240
$[0.32, 0.36]$	1	0.0124
$[0.36, 0.40]$	2	0.00586
$[0.40, 0.44]$	0	0.00178
$[0.44, 0.48]$	0	0.00011

Table 4.3: Number of events N_C observed in each bin of 0.04 ns of $|\Delta T|$, with the corresponding mismatch probability evaluated from MC simulation of type 1 events with $Z_{\text{vtx}} < 100$ m. The relative error on the probability due to statistics goes from $\sim 0.9\%$ on the first bins up to $\sim 2\%$ on the last ones. All the bins after the last one reported have a product $N_C \cdot p_{K-\pi}^{\text{matching}} = 0$.

available, allowing to study better the exact composition of all the upstream sub-samples. The number of events found in D1 and D2 and the respective mismatch probabilities are reported in table 4.4 and 4.5.

4.6 Upstream Background in 2018

As discussed in section 4, the upstream background was one of the major sources of background in 2016 and 2017. As already shown previously, in 2017 a copper plug was inserted in order to absorb type 2 events and reduce partially this kind of background in the 2017-II data sample. However, during the 2018 data taking, a critical move was enacted in order to definitely suppress type 2 events.

In particular, on 20th June 2018 the old NA48 collimator (informally known as *rainbow collimator*) was placed and aligned between the last station

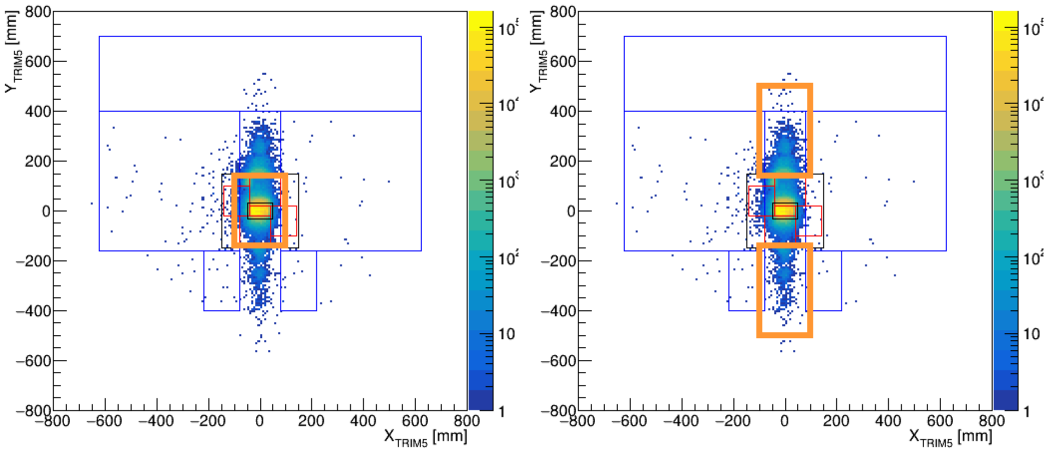

Figure 4.15: Extrapolation of the downstream track at the TRIM5 Z position for a data sample enriched with upstream background events; the orange boxes show the modified box cuts for the validation of the upstream background. Left: the box cut used for the definition of the subsamples B1 and D1; this region is dominated by type 1 events. Right: the box cut used for the definition of the subsamples B2 and D2; this region is dominated by type 2 events.

of the GigaTracker and the CHANTI. This new collimator is shown in fig. 4.20, while the previous collimator used in the 2016 and 2017 data taking is shown in fig. 4.19. The effect of the collimator is clear from fig. 4.21, where the type 2 component of the upstream background has been completely suppressed.

An important consequence of this for the 2018 analysis is that the box cut can be significantly shrunk in the Y coordinate with respect to 2016 and 2017, increasing the acceptance for the $K^+ \to \pi^+ \nu \bar{\nu}$ selection. Since the type 2 component is absorbed by the collimator, one possibility is to change the Y cut in the box from $|Y| > 500$ mm to $|Y| > 140$ mm.

The method discussed in section 4.4 will allow us to evaluate the upstream background in the signal region event after the installation of the new collimator, whereas the bifurcation method would fail because of the lack of statistics.

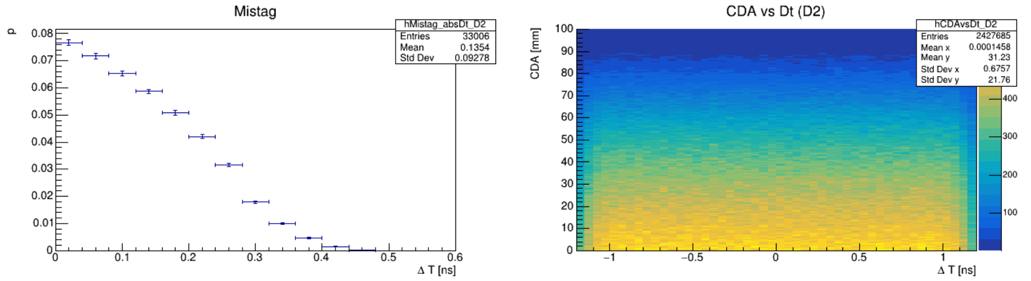

Figure 4.16: Left: mismatch probability for events in D2 as a function of $|\Delta T|$. Right: CDA vs ΔT for events in D2; the CDA distribution is evaluated from data.

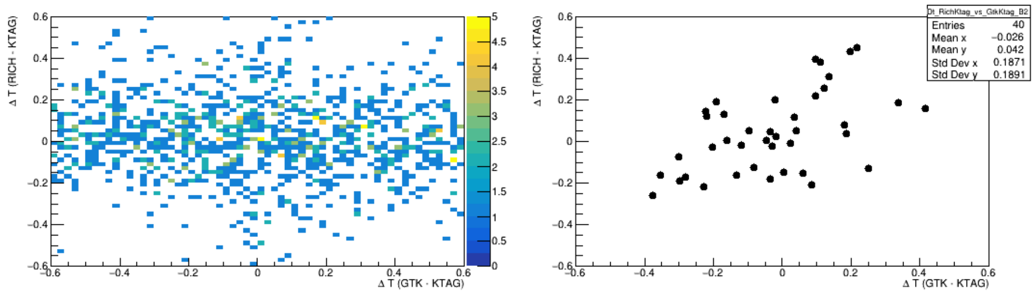

Figure 4.17: Time distribution of events in the B2 and D2 sub-samples (time in ns).

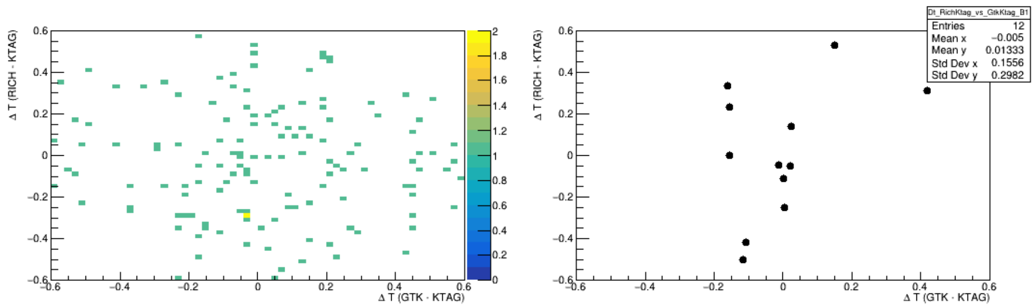

Figure 4.18: Time distribution of events in the B1 and D1 sub-samples (time in ns).

$\|\Delta T\|$ bin	$N_{D1}(\|\Delta T\|)$	$p_{K-\pi}^{\text{matching}}(\|\Delta T\|)$
$[0.00, 0.04]$	2	0.0972
$[0.04, 0.08]$	2	0.0919
$[0.08, 0.12]$	3	0.0833
$[0.12, 0.16]$	2	0.0754
$[0.16, 0.20]$	1	0.0633
$[0.20, 0.24]$	1	0.0521
$[0.24, 0.28]$	1	0.0387
$[0.28, 0.32]$	0	0.0240
$[0.32, 0.36]$	1	0.0124
$[0.36, 0.40]$	2	0.00586
$[0.40, 0.44]$	0	0.00178
$[0.44, 0.48]$	0	0.00011

Table 4.4: Number of events in the validation region D1 observed in each bin of 0.04 ns of $|\Delta T|$, with the corresponding mismatch probability evaluated from MC simulation of type 1 events with $Z_{\text{vtx}} < 100$ m.

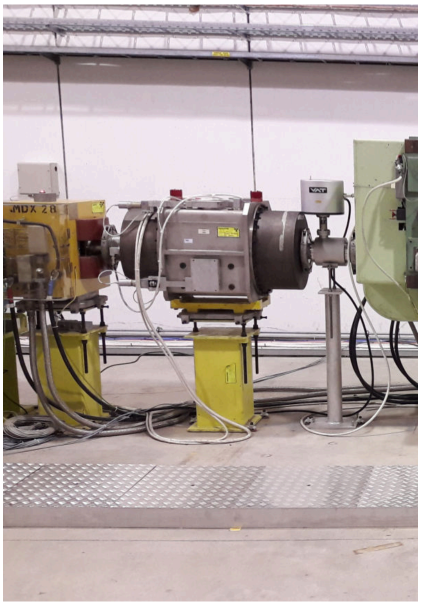

Figure 4.19: The NA62 collimator used in the 2016 and 2017 data taking.

$\lvert\Delta T\rvert$ bin	$N_{D1}(\lvert\Delta T\rvert)$	$p_{K-\pi}^{\text{matching}}(\lvert\Delta T\rvert)$
$[0.00, 0.04]$	99	0.0767
$[0.04, 0.08]$	93	0.0717
$[0.08, 0.12]$	94	0.0652
$[0.12, 0.16]$	79	0.0587
$[0.16, 0.20]$	85	0.0420
$[0.20, 0.24]$	71	0.0315
$[0.24, 0.28]$	65	0.0179
$[0.28, 0.32]$	67	0.00997
$[0.32, 0.36]$	66	0.00466
$[0.36, 0.40]$	54	0.00142
$[0.40, 0.44]$	70	0.00008
$[0.44, 0.48]$	48	0

Table 4.5: Number of events in the validation region D2 observed in each bin of 0.04 ns of $|\Delta T|$, with the corresponding mismatch probability evaluated from data.

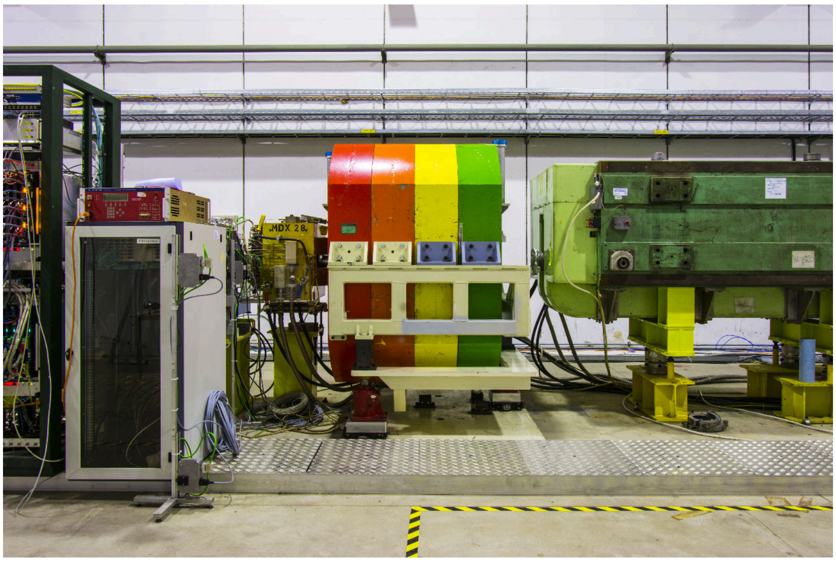

Figure 4.20: The old NA48 collimator, now positioned along the NA62 beam line in order to suppress the upstream background (photo courtesy of Silvia Martellotti).

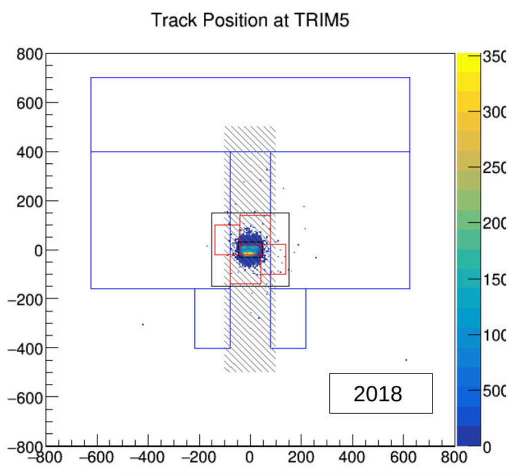

Figure 4.21: Extrapolation of the downstream π^+ track at the TRIM5 Z-position for a sub-sample of the 2018 data.

Chapter 5

Results

In the following I will present the results obtained applying the method established in 4.4 to my $\pi\nu\nu$ selection to evaluate the upstream background in the signal region.

The whole signal selection is applied, according to the procedure described in detail in 3.3. First of all a single-track event selection is performed, matching the π^+ track to the downstream detectors, building the K^+ track in the upstream detectors and applying the $K^+ - \pi^+$ association thanks to the matching discriminant; next the RICH and the calorimetric PID are applied to select downstream pions and reject muons and electrons; subsequently the photon rejection gets rid of events with extra activity in the photon veto; the multiplicity cuts reject events with multiple charged tracks in the final state; finally the beam background rejection is applied.

As reported in 4.4, the upstream background is evaluated selecting events with a large CDA and weighting them with the probability that an accidental track is matched to the downstream pion. Given the numbers reported in 4.3 and applying eq. 4.18 the expected number of upstream background events in the signal region is

$$N_{\text{up-bkg}} = 1.1 \pm 0.3 \ . \tag{5.1}$$

The signal box of the $K^+ \to \pi^+\nu\bar{\nu}$ analysis on 2017 data was opened in September 2019 during the KAON Conference in Perugia (Italy) and 2 events were observed (fig. 5.1). The results presented by the NA62 Collaboration come from the analyses of Dr. Giuseppe Ruggiero [57] and Dr. Radoslav Marchevski [60], with a signal selection compatible with the one presented in this thesis and used by me to study the upstream background. The SES and the expected number of signal events in the signal regions were expected to be:

$$\text{SES} = (0.389 \pm 0.021) \times 10^{-10} \ , \tag{5.2}$$

$$N^{\text{exp}}_{\pi\nu\nu} = 2.16 \pm 0.12 \pm 0.26_{\text{ext}} \ , \tag{5.3}$$

while the expected events in the signal regions for the various background sources and the total background contribution are reported in table 5.1. The SES was evaluated according to the procedure reported in 3.3.9, where the acceptance for the signal was evaluated to be $A_{\pi\nu\nu} \sim 3\%$, the acceptance for the normalization channel is $A_{\pi\pi} \sim 8.5\%$, the random veto $\epsilon_{\text{RV}} \sim 64\%$ and the trigger efficiency is close to 90%.

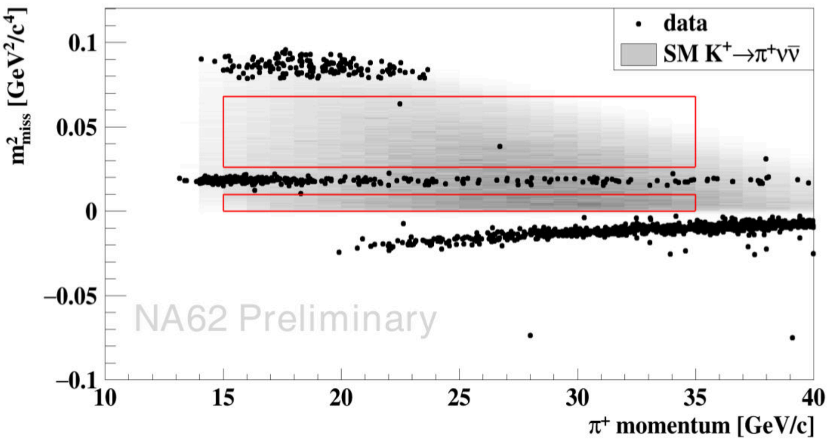

Figure 5.1: The two events observed in 2017 data, as presented at the KAON 2019 conference in Perugia by the NA62 Collaboration [57].

Combining the 2 events observed in the signal region in the 2017 data set with the event observed in the 2016 data set [18], NA62 is able to put the following upper limits to the branching ratio of $K^+ \to \pi^+\nu\bar{\nu}$:

$$BR(K^+ \to \pi^+\nu\bar{\nu}) < 1.85 \times 10^{-10} \quad @\,90\% \text{ C.L.} \tag{5.4}$$

$$BR(K^+ \to \pi^+\nu\bar{\nu}) < 2.44 \times 10^{-10} \quad @\,95\% \text{ C.L.} \tag{5.5}$$

as well as a two-sided 68% band,

$$BR(K^+ \to \pi^+\nu\bar{\nu}) = 0.47^{+0.72}_{-0.47} \times 10^{-10} \ . \tag{5.6}$$

The result presented by the NA62 Collaboration includes an evaluation of the upstream background; the value found and used for the result is $0.9 \pm 0.2_{\text{stat}} \pm 0.2_{\text{syst}}$, in very good agreement with what was found in this thesis. The small difference between the two values arises from small differences in the fitted CDA distribution of type 1 events, leading to slightly different mismatch probabilities in the first few bins. Unfortunately the statistics used by the MC to generate the CDA distribution is limited but this can be improved in the future with an extended MC-generation campaign to obtain more accurate results. Possible improvements to suppress the upstream background are discussed in chapter 6.

Process	Expected events
$K^+ \to \pi^+\nu\bar{\nu}$ (SM)	$2.16 \pm 0.12 \pm 0.26_{\text{ext}}$
$K^+ \to \pi^+\pi^0(\gamma)$ IB	$0.29 \pm 0.03_{\text{stat}} \pm 0.03_{\text{syst}}$
$K^+ \to \mu^+\nu_\mu(\gamma)$ IB	$0.11 \pm 0.02_{\text{stat}} \pm 0.03_{\text{syst}}$
$K^+ \to \mu^+\nu_\mu(\mu^+ \to e^+$ decay)	$0.04 \pm 0.02_{\text{syst}}$
$K^+ \to \pi^+\pi^-e^+\nu_e$	$0.12 \pm 0.05_{\text{stat}} \pm 0.03_{\text{syst}}$
$K^+ \to \pi^+\pi^+\pi^-$	$0.02 \pm 0.02_{\text{syst}}$
$K^+ \to \pi^+\gamma\gamma$	$0.005 \pm 0.005_{\text{syst}}$
$K^+ \to l^+\pi^0\nu_l$	negligible
Upstream background	$0.9 \pm 0.2_{\text{stat}} \pm 0.2_{\text{syst}}$
Total background	$1.5 \pm 0.2_{\text{stat}} \pm 0.2_{\text{syst}}$

Table 5.1: The expectation for the $\pi\nu\nu$ signal and the background sources in the signal regions as presented by the NA62 Collaboration at the KAON conference in Perugia [57].

Chapter 6

Conclusions

Flavour physics is one of the most important areas where physicists can hope to find signals of new physics and, in particular, precision measurements on rare or forbidden kaon decays still represent a very productive field where theories beyond the Standard Model can be tested.

The measurements of the branching ratios of the $K^+ \to \pi^+\nu\bar{\nu}$ and $K_L \to \pi^0\nu\bar{\nu}$ decays will give fundamental information about the flavour structure of the new physics. In figure 6.1 the preliminary results of NA62 with the 2016 and 2017 data sets combined are compared to the experimental result of the E797/E949 Collaboration and the most recent SM expectation. So far NA62 is compatible with both E797/E949 and the SM but there is still room for improvement. Indeed the 2018 data set is currently being analyzed; in this data set, about twice the number of K^+ decays were collected with respect to 2017. Moreover there will be another period of data taking after the long shutdown 2 (LS2) of LHC, with the first year (2021) already approved. Nevertheless, the NA62 preliminary result already allows to make some general considerations:

- Given the preliminary upper limits reported in eq. 5.4 and 5.5, NA62 is able to exclude the largest enhancements to $BR(K^+ \to \pi^+\nu\bar{\nu})$ allowed by some NP models (Randall-Sundrum, Littlest Higgs with T-parity, MSSM non-MFV, LFU violation models) in specific portions of their phase spaces, introducing further constraints to the free parameters related to each model; however the measurement is still not accurate enough to exclude any of the models in particular. Figure 6.2 shows the expectation for $BR(K^+ \to \pi^+\nu\bar{\nu})$ for the models that the NA62 measurement can already constrain. More specifically, the NA62 90% C.L. upper limit excludes a small portion of the RS model but just for the points predicted by fitting the experimental value of ϵ_K with an arbitrarily high fine-tuning, while the points relative to a moderate fine-tuning are still well consistent with the measurement (fig. 6.2a) [19]. As regards the LHT model with T-parity, NA62 can now exclude a large portion of the high-BR horizontal branch, however that area is already largely excluded by the constraint on $K_L \to \mu^+\mu^-$ (fig. 6.2b) [23]. In the MSSM for SUSY at 10 TeV, NA62 is able to place a mild constraint but just in a very specific scenario where ϵ_K is not imposed in the model and the left-right squark mixing angle θ^b_{LR} has the largest value taken into consideration by the model itself (fig. 6.2c) [61]. Finally, in LFU violation models where the lepton flavour interactions are mainly coupled to third-generation left-handed fermions, NA62 can already exclude a large range of possibilities in one of the scenarios considered (fig. 6.2d) [24].

- The new upper limit on $BR(K^+ \to \pi^+\nu\bar{\nu})$ provides a new model-independent limit on $BR(K_L \to \pi^0\nu\bar{\nu})$ that comes from the Grossman-Nir bound [57][25],

$$BR(K_L \to \pi^0\nu\bar{\nu}) < 8.14 \times 10^{-10} \quad @\,90\%\text{ C.L.} \tag{6.1}$$

- The NA62 preliminary 90% C.L. is very close to the central value measured by E797/E949 and we can already exclude the upper part of the two-sided band quoted by E797/E949; therefore, it is very unlikely that the branching ratio takes a value which is more than twice the SM one (see fig. 6.1).

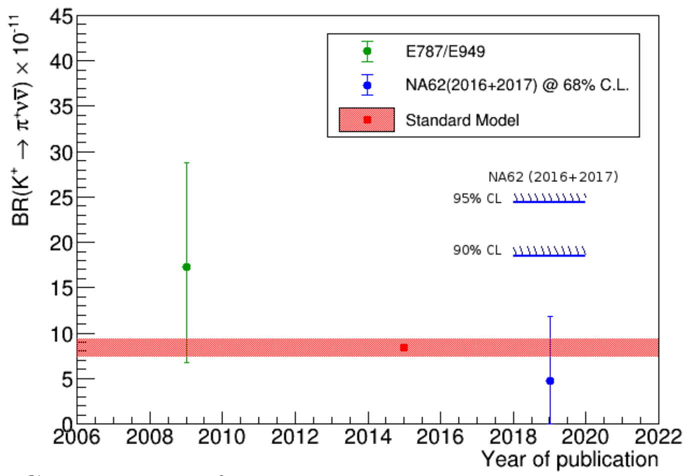

Figure 6.1: Comparison of the experimental results on $BR(K^+ \to \pi^+\nu\bar{\nu})$ obtained by NA62 and the E797/E949 Collaboration, along with the most recent SM expectation. The NA62 point comes from the combination of the 2016 and 2017 data set; the two upper limits at 90% and 95% C.L. are also shown.

As it has been shown in this work, the upstream background is probably the trickiest background to the $\pi\nu\nu$ measurement at NA62 in terms of understading the physics behind it and suppressing it in a meaningful way. I have demonstrated how the bifurcation analysis used for the 2016 data set cannot be applied because of the multifaceted nature of the upstream events and I proposed an alternative method based on the usage of the probability of matching the downstream track to an accidental upstream track. This is important not only for the 2017 data set but also for the 2018 one, where the presence of the new collimator (see 4.6) would make it impossible to apply the bifurcation method because of the lack of statistics in the control samples.

This new method was developed further by other people in the collaboration, in order to take into account the different CDA distribution of type 1 and type 2 events. I applied the new method in two different control regions, obtaining results that are consistent with the observations; finally I calculated the expected upstream background inside the signal region and found a value consistent with the preliminary result presented at KAON 2019 by the NA62 Collaboration. The very small difference is understood in terms of a slightly different PDF originated from the CDA distribution of MC type 1 events; this will be improved in the future as soon as a better MC sample is available.

The new method has the additional advantage of showing where we can look for possible improvements for the suppression of the upstream background. In particular, the NA62 Collaboration endorsed the construction of a fourth station of the Gigatracker (GTK4) and an Anti-Counter detector before the final collimator that will allow for a better time resolution of the GTK and a better pile-up treatment; according to simulations, this will reduce the upstream background of a factor $3-4$ [62].

Moreover the new collimator that suppresses the source of π^+ originated upstream reaching the fiducial volume will allow to loosen the box cut, although it cannot be completely removed because of upstream kaon decays still passing through the hole in the collimator. Finally a MVA can lead to improvements in the $K^+ - \pi^+$ association.

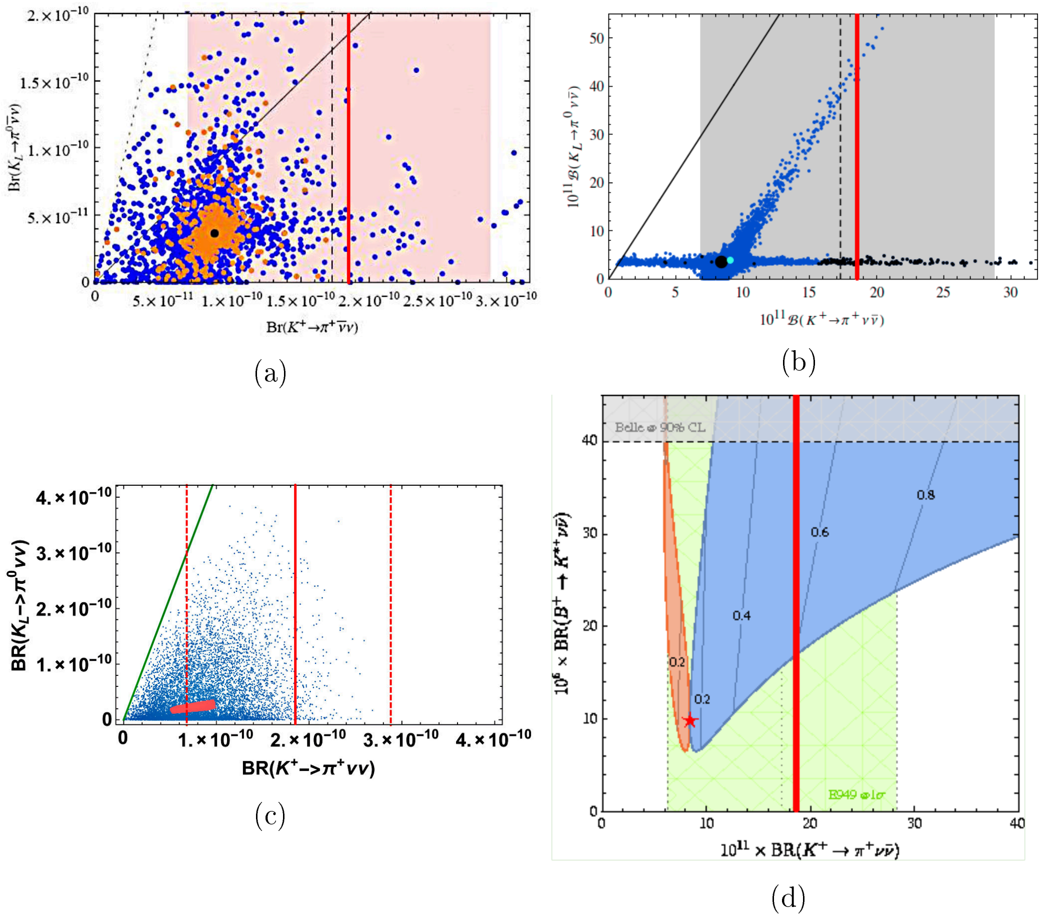

Figure 6.2: Predictions of NP models for $BR(K^+ \to \pi^+\nu\bar{\nu})$, compared to the NA62 upper limit at 90% C.L. (thick red line). The E797/E949 1σ band is also shown in each plot.

(a) $BR(K_L \to \pi^0\nu\bar{\nu})$ vs. $BR(K^+ \to \pi^+\nu\bar{\nu})$ in the Randall-Sundrum model; the black dot represents the SM prediction, orange dots refer to a moderate fine-tuning of the fit of the experimental value of ϵ_K, while blue dots are obtained with an arbitrarily high fine-tuning [19].

(b) $BR(K_L \to \pi^0\nu\bar{\nu})$ vs. $BR(K^+ \to \pi^+\nu\bar{\nu})$ in the Littlest Higgs model with T-parity; the black dots are excluded by the constraint on $K_L \to \mu^+\mu^-$ [23].

(c) $BR(K_L \to \pi^0\nu\bar{\nu})$ vs. $BR(K^+ \to \pi^+\nu\bar{\nu})$ in MSSM for SUSY at 10 TeV, without imposing ϵ_K and with a down-type left-right squark mixing angle $\theta^b_{LR} = 0.3$ [61].

(d) $BR(B^+ \to K^{*+}\nu\bar{\nu})$ vs. $BR(K^+ \to \pi^+\nu\bar{\nu})$ in models with lepton flavour violating interactions mainly coupled to left-handed third-generation fermions; the orange (blue) area corresponds to $c_{13} = 0$ ($c_{13} = 2$), where c_{13} is the ratio between the singlet and triplet Wilson coefficients in the model [24].

Additional improvements to the $K^+ \to \pi^+\nu\bar{\nu}$ measurement include: a better PID algorithm for the muon rejection; the removal of the cut on Z_{vertex} vs R_{STRAW1} to reject $K^+_{3\pi}$ decays, since it has been observed that these background events are very well separated from the signal region; a more intensity-resilient TDAQ system for detectors with critical occupancy issues, such as CHANTI and KTAG; an additional HASC detector, symmetrical to the existing one with respect to the beam pipe, in order to have a better photon rejection; an improved treatment of the random veto that can be achieved with a better clustering algorithm in the LKr; a better usage of the LAV variables (currently the LAV veto does not make use of the LAV station position or the time-over-threshold information) and the exploitation of the angle-energy correlation of photons in SAV with those in LAV and LKr.

Taking into account the improvements to the selection for the 2018 analysis just mentioned, the number of signal events expected in the 2018 data set is 7.0 ± 0.7 with an expected background of 4.8 ± 1.0 events [62], considering conservatively the same signal to background ratio as in 2017.

The first year of data taking after the LS2 has already been approved: considering all the improvements to the hardware and to the analysis that have been listed above, the expected number of signal events in a 2018-equivalent data taking year is 14.0 ± 1.5. Extending this prediction to the whole three-years period between LS2 and LS3, the total number of signal events is 42 ± 5. Using a counting approach and assuming a signal-to-background ratio of the order of 2.5, the first year of data taking after LS2 will lead to a 3.8σ SM signal evidence when combined with data already taken from 2016 to 2018; preliminary studies show that a m^2_{miss} and π^+ momentum shape analysis will raise the significance of the observation to 5σ. With three years of data taking after LS2, NA62 will be able to perform a 20% precision measurement of the branching ratio of the $K^+ \to \pi^+\nu\bar{\nu}$ decay [62].

Appendix A

CHOD software and performances

An important part of my PhD activity was dedicated to the development and improvement of the software related to the old CHOD detector (the NA48-CHOD). A detailed description of this detector is given in 2.4.6, while the following sections concern the work I have done on the software and the performances reached by the CHOD detector after all the offline corrections are applied.

A.1 CHOD efficiency

I developed the `CHODEfficiency` analyzer in order to have a fast way to check the performances of the detector a few hours after a run is taken. In fact during the data taking, the NA62 Online Monitor[1] is the main tool shifters have to spot important problems in the data acquisition; though some particular issues need a slightly more sofisticated approach dedicated to every single detector, such as a specific efficiency analyzer.

`CHODEfficiency` integrates all the bursts taken in a run and computes the efficiency of the detector in different ways. The analyzer takes into account only events passing the PNN trigger flag and in the acceptance of the NewCHOD. The Control trigger events are not taken into account for obvious reasons, since the control trigger condition is a signal in the CHOD itself. In order to compute the efficiency, every track found in the Spectrometer is extrapolated to the CHOD plane: the efficiency is the number of the extrapolated tracks with a corresponding CHOD candidate in the point of the extrapolation, normalized by the number of tracks.

A report in pdf format is generated, showing 17 plots (see a few examples

[1] `NA62OnlineMonitor` is an Analyzer showing the most relevant plots for each detector during the data taking in the NA62 Control Room.

in fig. A.1 and A.2). The first four plots show the overall efficiency of the detector as a function of the burst identification number. The four plots differ by the kind of events that are selected:

- with or without single-track requirement in the STRAW;
- with or without shower-like events rejection required.

The plot generated selecting single-track and no-shower events is particularly important, since it is the "cleanest" one and it is used in order to generate the *bad burst* list (bad bursts are bursts that didn't pass certain quality criteria for one or more detectors, e.g. due to a malfunction of the hardware). The second group of four plots shows the overall efficiency as a function of the momentum of the track; the difference between the four plots is the same as for the previous group. The third group of four plots shows the overall efficiency as a function of the Z coordinate of the vertex between the upstream and the downstream track. The last group of four plots shows a 2D map of the efficiency of the every single CHOD intersection point. An additional 2D plot shows the integrated illumination of the detector for the whole run and it could be useful to spot very peculiar problems.

The 2D efficiency plot with the single-track and no-shower requests is probably the most useful to spot problems in the hardware or in the time alignment of the channels. Indeed, when a scintillator (or a group of them) is not working properly, a huge drop in the efficiency is clearly visible there, and it is easy to identify the flawed channel (or board), like in fig. A.2.

As mentioned above, the other output of `CHODEfficiency` (a part from the report) is the bad burst list. The bad burst list contains the number of all the bursts flagged as "bad" by the analyzer. There are two criteria according to which a burst is flagged as bad by `CHODEfficiency`. Either the efficiency is too low, i.e. $\epsilon < 0.9$ (flag=LOWEFF), or the statistics is too low, i.e. $N_{events} < 100$ (falg=LOWSTAT). The bad burst list can be passed as a parameter at the analysis level to skip all the bad bursts in a run.

A.2 Time calibration of the CHOD detector

The reconstruction analyzers for all the detectors contain the code needed to reconstruct the raw data and organize them in high level structures such as hits and candidates (see section 3.1), that can be used conveniently in physics analysis. The CHOD reconstruction and digitizer were already present at the beginning of my doctoral course, but major improvements and new features have been added, especially concerning the time information of hits and candidates.

Typically, the CHOD candidate is defined as the coincidence of two signals or hits, one in a vertical counter and the other in a horizontal one. A few conditions should be met to reconstruct the candidate:

- the hits must be closer than 10 ns with respect to each other;
- the difference between a hit time and the trigger time must be less than 25 ns;
- the hits must belong to the same quadrant of the detector;
- the T0's of the two hits must be good in order to avoid unphysical intersections between the slabs;
- the number of hits around the trigger ($\pm$25 ns) must be less than 40.

Moreover, in order to have a better time resolution, only hits with both leading and trailing time are taken into account; this last condition can actually be released modifying a parameter in a configuration file, so that it will be possible to reconstruct a few 2018 test runs taken without a trailing time in the CHOD.

Two corrections should always be applied to the time of hits (or candidates) in the CHOD, the *T0* corrections and the *slewing* corrections.

The **T0 corrections** are needed to take into account the delay due to the position where the particle hits the scintillator with respect to the position of the photomultiplier; the farther the actual impact point is from the photomultiplier, the greater will be the delay that has to be added to the time associated to the signal in the PM. In other words, since all the PM of the CHOD are placed at the external end of each slab, if the particle hits the detector close to the central part, the absolute value of the T0 correction will be high; conversely a particle hitting a slab close to the PM position should receive a minor T0 correction.

As it is clear from this definition, the CHOD T0 correction needs the information of two crossing counters in order to be applied, because the distance between the PM and the actual position of the particle has to be known. Originally, this issue was addressed with the calculation and implementation of 2048 T0's, one for each possible intersection point between the 64 vertical and 64 horizontal slabs. This strategy was fine for the 2016 data taking, but definitely non-optimal for the 2017 and 2018, when the intensity was higher. The reason why this approach failed is that a significant amount of sharp double peaks in the time coincidences between vertical and horizontal hits started to appear, originated by random coincidences between counters due to the higher intensity. Another problem of the old approach was the very low statistics for many external intersection points which led to inaccurate results in the automatic evaluation of T0's (see fig. A.3).

A better and more stable approach makes use of the scintillators light velocities. Typically, the photons travel inside the CHOD counters with a velocity[2] of ~ 0.07 ns/cm or, alternatively, ~ 14 cm/ns. I developed a new analyzer (`CHODLightVelocitiesCalculation`) to calculate the light velocities for each of the 128 counters. The light velocities are pretty much stable during the three years of data taking, as it is shown in fig. A.4. The new T0's are 128, one for each slab. Each hit is consequently corrected taking into account the light velocity and the distance from the PM given by the intersection between the slabs. This new procedure doesn't have problems related to the low statistics, since all the intersection points benefit from the statistics of all the others in the same counters and random coincidences are not an issue in this case. A comparison between the old and the new T0's is shown in fig. A.3.

Other important corrections that have to be applied and that I implemented in the framework are the **slewing corrections**[3]. The need for these corrections is to be found in the different rising time between pulses with different amplitudes, producing different leading times for the hits when a threshold is fixed. The slewing corrections for the CHOD consist of 2048 *slewing slopes* and 2048 *slewing constant*, one for each intersection point, and are derived from the distribution of the Time-Over-Threshold (TOT) obtained for some runs evenly distributed along the data taking periods. They are applied offline to the time of each hit in the reconstruction process, according to the formula:

$$t_{\text{corrected}} = t_{uncorrected} - s \cdot \text{TOT} - c \;, \tag{A.1}$$

where $s = s(IP)$ and $c = c(IP)$ are the slewing slope and constant, functions of the intersection point IP. The slewing slope is obtained from the linear fit of the distribution of the time of the CHOD with respect to the KTAG versus the TOT; the slewing constant is simply $(-1) \cdot s \cdot <\text{TOT}>$, where $<\text{TOT}>$ is the average TOT for that particular IP (see fig. A.5).

The importance of the T0 and the slewing corrections is clear from fig. A.6, where one can see how the time distribution of the hits gets well-centered and narrower after the T0's and the slewing corrections are applied.

Another aspect that has to be taken into account when applying time corrections is the run dependence. As a matter of fact, the scintillators or the PMs of the detector will lose efficiency over time, and this degradation

[2]The speed of light in a vacuum is ~ 0.033 ns/cm or ~ 29.98 cm/ns.

[3]In the literature, the time slewing is also known as *time walk*.

of the hardware could lead to significant differences in the value of the T0's, the light velocities, the time-over-threshold and the slewing corrections. As regards the light velocities, the values didn't change significantly in the period 2016-2018, as it is shown in fig. A.4; the T0's stability is not a real problem since T0's are automatically computed offline for each single run. This is not true for the time-over-threshold and, consequently, the slewing corrections. So far a few sets of slewing corrections have been generated for different periods, in order to have enough variability, but the framework still doesn't generate them on a run by run base. This is not crucial, since the effect of the slewing corrections is not as important as the effect of the T0, and a small change in their values doesn't imply a significant variation on the time performance; nevertheless this step will definitely be implemented in the future. The degradation of the TOT over the years is shown in fig. A.7.

Moving to the time resolution of the detector, the performance is shown in fig. A.8. One can see how the detector performances slightly degraded over time, however the differences are really marginal. Taking into account a resolution of 70 ps for the KTAG (that is almost negligible in this case), the time resolution of the CHOD candidate is ~ 200 ps in 2016, ~ 230 ps in 2017 and ~ 250 ps in 2018. The CHOD detector is more than 25 years old, nonetheless it is still performing quite well, with a time resolution that meets the requirements of the experiment and that is still relatively close to the one that was measured in the NA48 experiment [31].

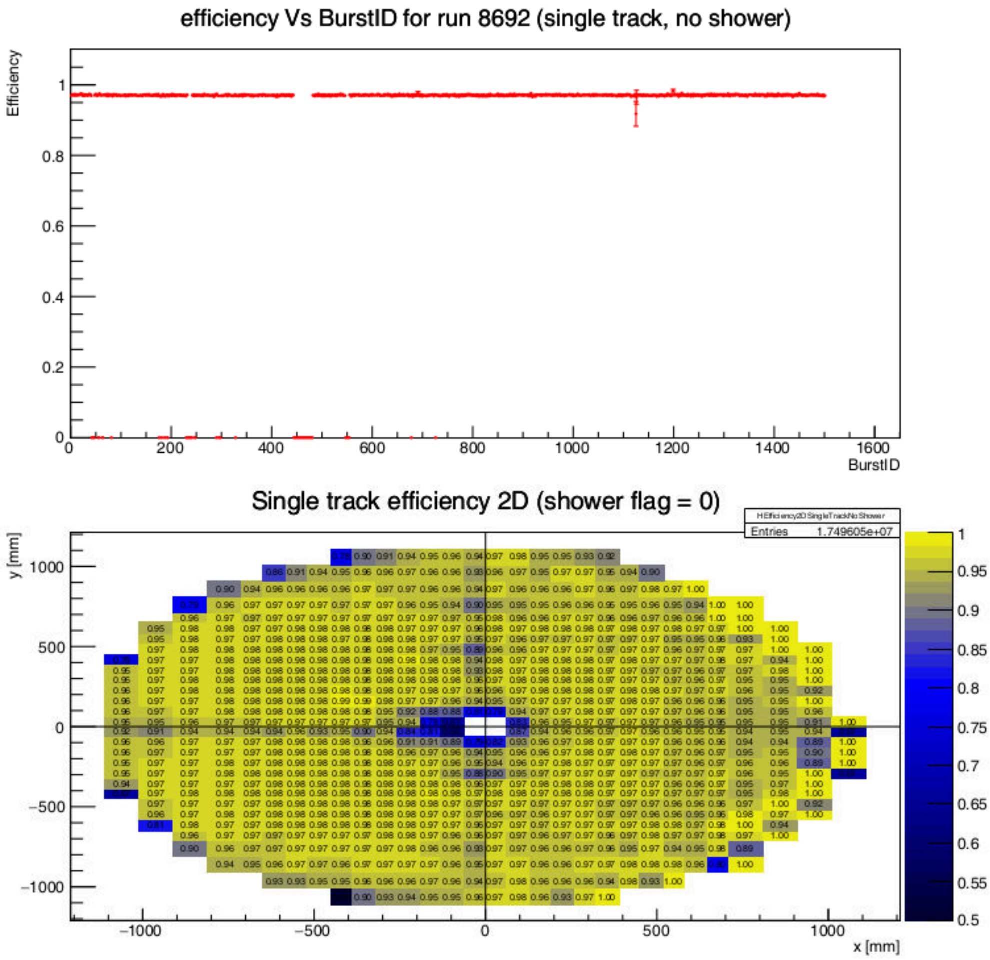

Figure A.1: Two of the plots generated by the `CHODEfficiency` analyzer, both of them requiring a single track event that is of type "no-shower". The top plot shows the efficiency in the run as a function of the burst number, while the second one shows the overall efficiency of the run as a function of the intersection point in the detector. This is a typically good run for the CHOD, with an efficiency that is almost always above 90% for all the bursts.

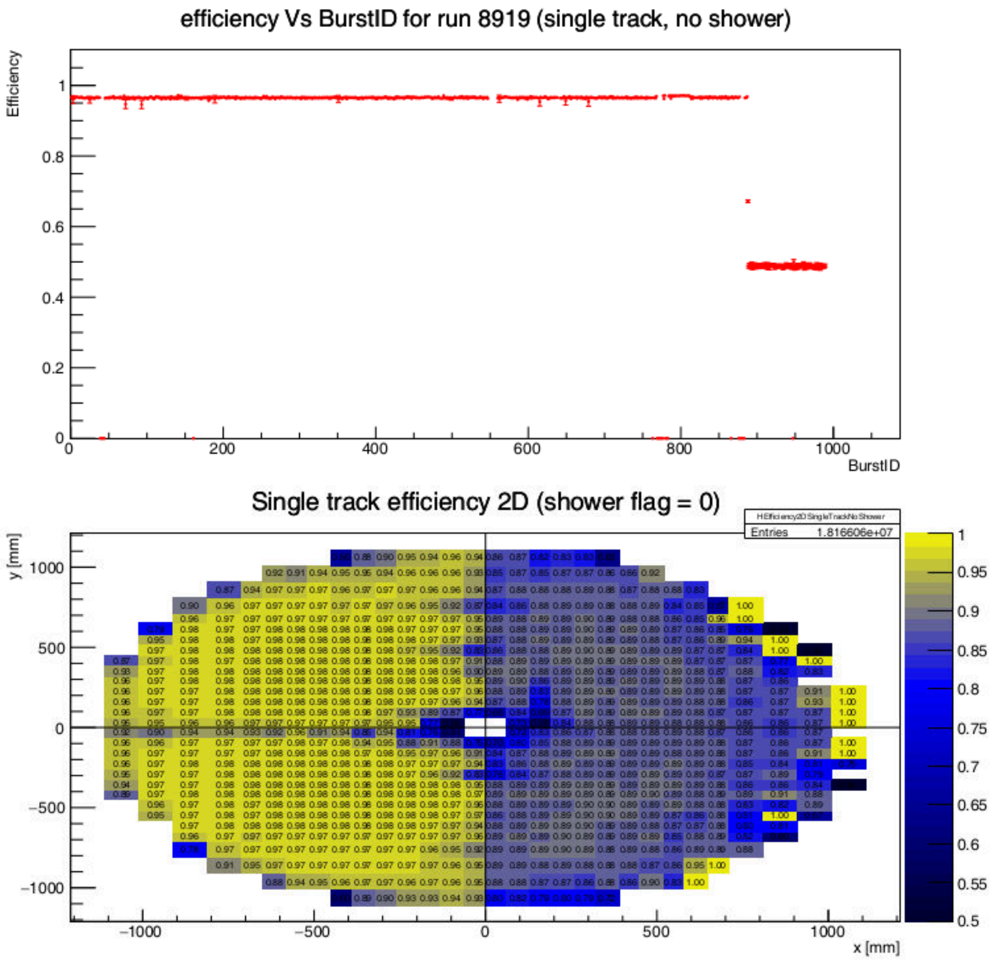

Figure A.2: Two of the plots generated by the `CHODEfficiency` analyzer, both of them requiring a single track event that is of type "no-shower". The top plot shows the efficiency in the run as a function of the burst number, while the second one shows the overall efficiency of the run as a function of the intersection point in the detector. The last part of this run is clearly bad: the efficiency is 50% for the last ~ 100 bursts and the reason can be inferred by the bottom plot, where one can see that one of the four readout boards (connected to a half of a plane) was off.

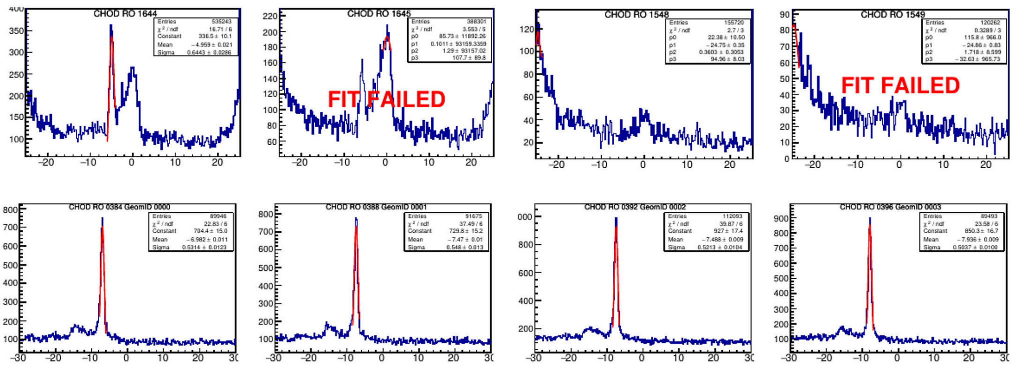

Figure A.3: Comparison between the fit obtained with the old (top plots) and the new (bottom plots) T0 evaluation procedure for the CHOD detector. With the old procedure, several intersection points out of the 2048 possible ones had sharp double peaks (top row, first two plots) because of random coincidences or the lack of statistics (top row, last two plots). Reducing the number of T0's to 128, one for each counter, the statistics is not a problem anymore and no double peaks are present (bottom row).

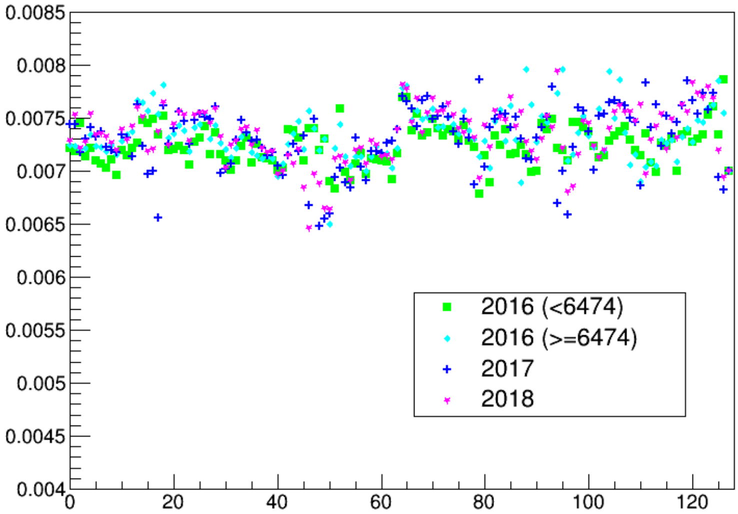

Figure A.4: Light velocities in the 128 scintillation counters of the CHOD detectors for different periods of data taking.

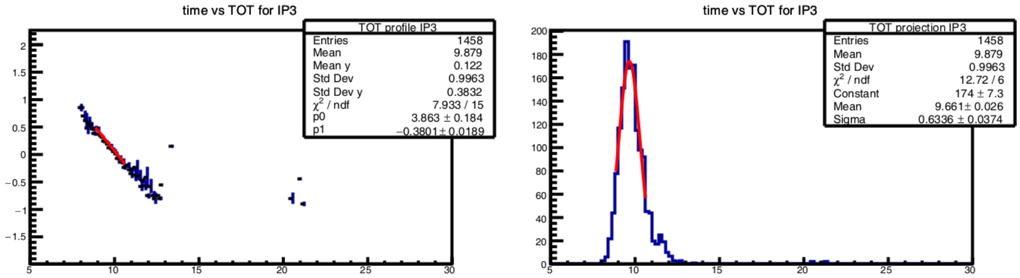

Figure A.5: Both plots refer to one intersection point of the vertical slab 32. Left plot: time (wrt KTAG) vs. time-over-threshold. Right plot: TOT distribution.

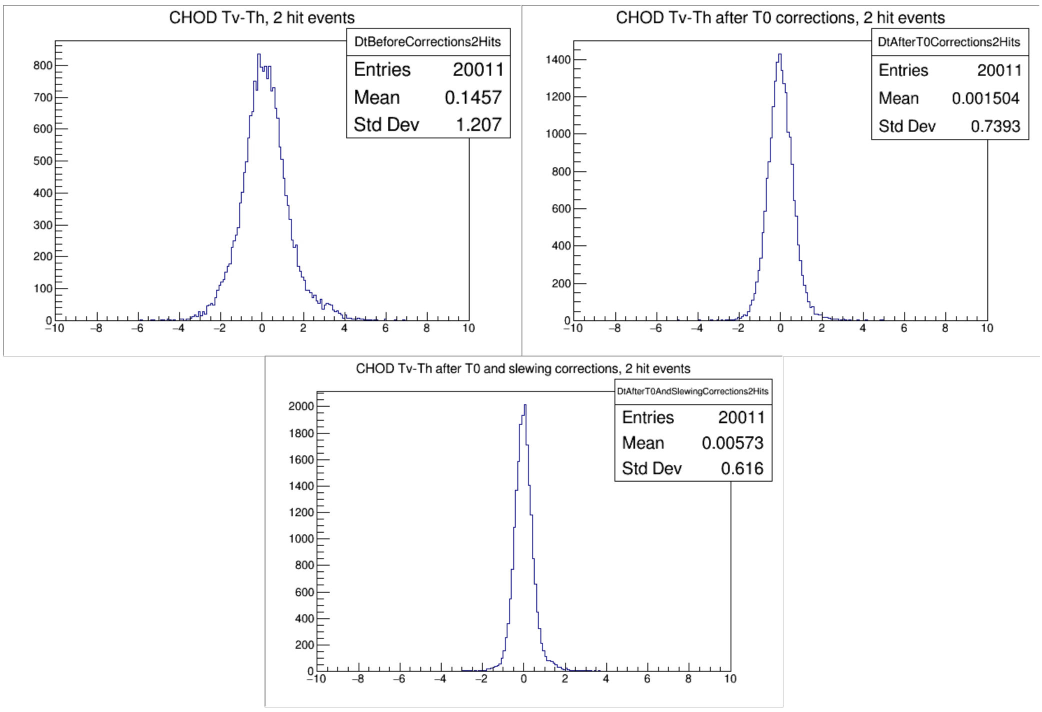

Figure A.6: The top left plot shows the difference between a hit in the vertical plane and a hit in the horizontal one, before applying any correction; on the second plot on the top, the T0's are applied and hence the mean of the distribution is well-centered at zero; on the bottom plot both the T0's and the slewing corrections are applied and the distribution gets narrower. All the plot refer to a single burst from a 2017 run.

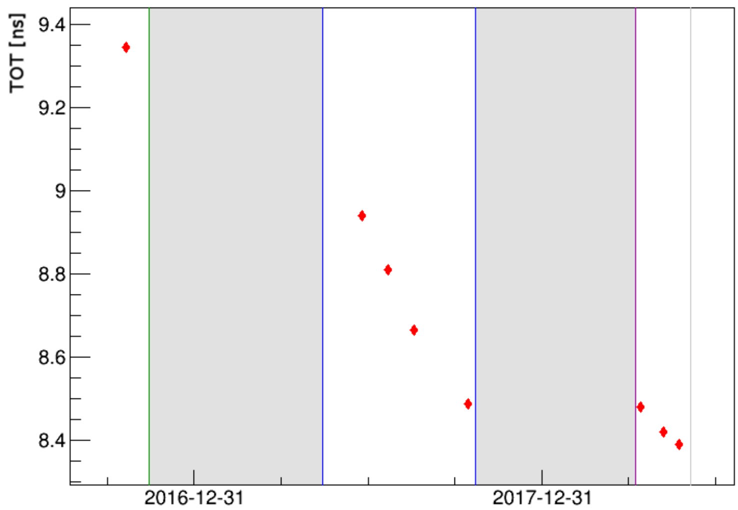

Figure A.7: Evolution of the mean value of the time-over-threshold from 2016 to 2018. Each point refers to a single run; the grey areas are periods where there was no data taking.

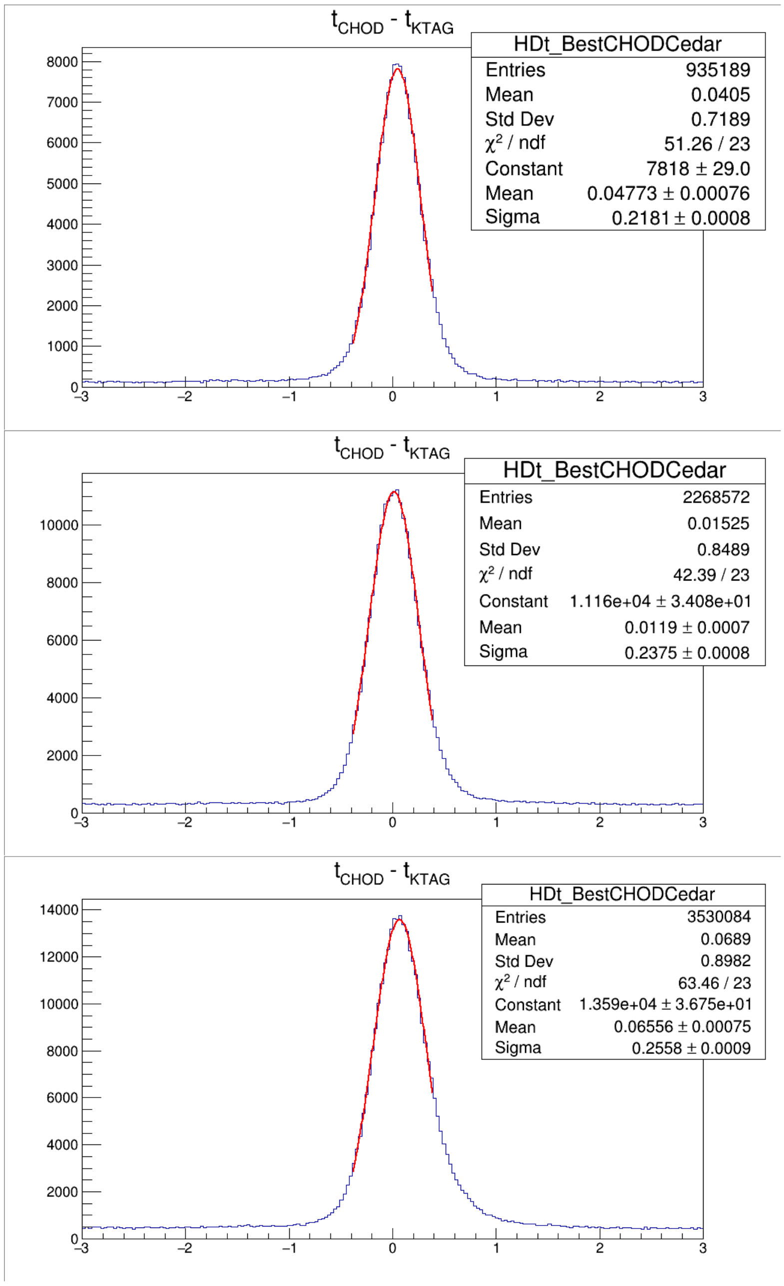

Figure A.8: Difference between the time of the best CHOD candidate associated to the track and a KTAG candidate for three different runs from each year of data taking. From top to bottom, the plots refer respectively to the 2016, 2017 and 2018 data taking.

Bibliography

[1] M. Tanabashi et al. 'Review of Particle Physics'. In: *Phys. Rev. D* 98 (3 2018), p. 030001. DOI: 10.1103/PhysRevD.98.030001.

[2] K. Agashe et al. 'RS1, custodial isospin and precision tests'. In: *JHEP* 08 (2003), p. 050. DOI: 10.1088/1126-6708/2003/08/050.

[3] G. Aad et al. 'Observation of a new particle in the search for the Standard Model Higgs boson with the ATLAS detector at the LHC'. In: *Phys. Lett. B* 716.1 (2012), pp. 1 –29. DOI: https://doi.org/10.1016/j.physletb.2012.08.020.

[4] S. Chatrchyan et al. 'Observation of a new boson at a mass of 125 GeV with the CMS experiment at the LHC'. In: *Phys. Lett. B* 716.1 (2012), pp. 30 –61. ISSN: 0370-2693. DOI: https://doi.org/10.1016/j.physletb.2012.08.021.

[5] M. Thomson. *Modern Particle Physics*. Cambridge University Press, 2013. ISBN: 9781107034266.

[6] M. Bauer and T. Plehn. *Yet Another Introduction to Dark Matter*. Springer, 2019. ISBN: 9783030162337. DOI: 10.1007/978-3-030-16234-4.

[7] M. Sozzi. *Discrete Symmetries and CP Violation: From Experiment to Theory*. Oxford University Press, 2008. ISBN: 9780199296668.

[8] A. Bettini. *Introduction of Elementary Particle Physics*. 2nd ed. Cambridge University Press, 2014. ISBN: 9781107050402.

[9] R. P. Woodard. 'How Far Are We from the Quantum Theory of Gravity?' In: *Rept. Prog. Phys.* 72 (2009), p. 126002. DOI: 10.1088/0034-4885/72/12/126002.

[10] E. Cortina Gil et al. 'Search for heavy neutral lepton production in K^+ decays'. In: *Phys. Lett.* B778 (2018), pp. 137–145. DOI: 10.1016/j.physletb.2018.01.031.

[11] E. Cortina Gil et al. 'Search for production of an invisible dark photon in π^0 decays'. In: *JHEP* 05 (2019), p. 182. DOI: 10.1007/JHEP05(2019)182.

[12] E. Cortina Gil et al. 'Searches for lepton number violating K^+ decays'. In: *Phys. Lett.* B797 (2019), p. 134794. DOI: 10.1016/j.physletb.2019.07.041.

[13] B. Dobrich et al. 'ALPtraum: ALP production in proton beam dump experiments'. In: *JHEP* 02 (2016), p. 018. DOI: 10.1007/JHEP02(2016)018.

[14] L. Wolfenstein. 'Parametrization of the Kobayashi-Maskawa Matrix'. In: *Phys. Rev. Lett.* 51 (21 1983), pp. 1945–1947. DOI: 10.1103/PhysRevLett.51.1945.

[15] A. J. Buras et al. '$K^+ \to \pi^+\nu\overline{\nu}$ and $K_L \to \pi^0\nu\overline{\nu}$ in the Standard Model: status and perspectives'. In: *JHEP* 11 (2015), p. 033. DOI: 10.1007/JHEP11(2015)033.

[16] A. V. Artamonov et al. 'Study of the decay $K^+ \to \pi^+\nu\overline{\nu}$ in the momentum region $140 < P_\pi < 199$ MeV/c'. In: *Phys. Rev. D* 79 (9 2009), p. 092004. DOI: 10.1103/PhysRevD.79.092004.

[17] J. K. Ahn et al. 'Search for the $K_L \to \pi^0\nu\overline{\nu}$ and $K_L \to \pi^0 X^0$ decays at the J-PARC KOTO experiment'. In: *Phys. Rev. Lett.* 122.2 (2019), p. 021802. DOI: 10.1103/PhysRevLett.122.021802.

[18] E. Cortina Gil et al. 'First search for $K^+ \to \pi^+\nu\overline{\nu}$ using the decay-in-flight technique'. In: *Phys. Lett.* B791 (2019), pp. 156–166. DOI: 10.1016/j.physletb.2019.01.067.

[19] M. Blanke et al. 'Rare K and B Decays in a Warped Extra Dimension with Custodial Protection'. In: *JHEP* 03 (2009), p. 108. DOI: 10.1088/1126-6708/2009/03/108.

[20] T. Blažek and P. Maták. 'Left–left squark mixing, $K^+ \to \pi^+\nu\overline{\nu}$ and minimal supersymmetry with large tanβ'. In: *Int. J. Mod. Phys.* A29.27 (2014), p. 1450162. DOI: 10.1142/S0217751X14501620.

[21] G. Isidori et al. 'Exploring the flavour structure of the MSSM with rare K decays'. In: *JHEP* 08 (2006), p. 064. DOI: 10.1088/1126-6708/2006/08/064.

[22] A. J. Buras, D. Buttazzo, and R. Knegjens. '$K \to \pi\nu\overline{\nu}$ and ε'/ε in simplified new physics models'. In: *JHEP* 11 (2015), p. 166. DOI: 10.1007/JHEP11(2015)166.

[23] M. Blanke, A. J. Buras, and S. Recksiegel. 'Quark flavour observables in the Littlest Higgs model with T-parity after LHC Run 1'. In: *Eur. Phys. J.* C76.4 (2016), p. 182. DOI: 10.1140/epjc/s10052-016-4019-7.

[24] M. Bordone et al. 'Probing Lepton Flavour Universality with $K \to \pi\nu\bar{\nu}$ decays'. In: *Eur. Phys. J.* C77.9 (2017), p. 618. DOI: 10.1140/epjc/s10052-017-5202-1.

[25] Y. Grossman and Y. Nir. '$K_L \to \pi^0\nu\bar{\nu}$ beyond the standard model'. In: *Phys. Lett. B* 398.1 (1997), pp. 163 –168. DOI: https://doi.org/10.1016/S0370-2693(97)00210-4.

[26] J. Charles et al. 'CP violation and the CKM matrix: Assessing the impact of the asymmetric *B* factories'. In: *Eur. Phys. J.* C41.1 (2005), pp. 1–131. DOI: 10.1140/epjc/s2005-02169-1.

[27] *Prospective studies on $K^+ \to \pi^+\nu\bar{\nu}$ and $K_L \to \pi^0\nu\bar{\nu}$ rare kaon decays.* URL: http://ckmfitter.in2p3.fr/www/studies/plots_kpinunu15/ckm_plots_kpinunu15.html.

[28] E. Cortina Gil et al. 'The Beam and detector of the NA62 experiment at CERN'. In: *JINST* 12.05 (2017), P05025. DOI: 10.1088/1748-0221/12/05/P05025.

[29] O. S. Brüning et al. *LHC Design Report.* CERN Yellow Reports: Monographs. Geneva: CERN, 2004. DOI: 10.5170/CERN-2004-003-V-1.

[30] V. Kain et al. 'SPS Slow Extracted Spill Quality During the 2016 Run'. In: CERN-ACC-2017-121 (2017), MOPIK049. 4 p. DOI: 10.18429/JACoW-IPAC2017-MOPIK049.

[31] V. Fanti et al. 'The Beam and detector for the NA48 neutral kaon CP violations experiment at CERN'. In: *NIM* A574 (2007), pp. 433–471. DOI: 10.1016/j.nima.2007.01.178.

[32] E. Goudzovski et al. 'Development of the kaon tagging system for the NA62 experiment at CERN'. In: *Nucl. Instrum. Meth.* A801 (2015), pp. 86–94. DOI: 10.1016/j.nima.2015.08.015.

[33] G. Aglieri Rinella et al. 'The NA62 GigaTracKer: a low mass high intensity beam 4D tracker with 65 ps time resolution on tracks'. In: (2019). DOI: 10.1088/1748-0221/14/07/P07010.

[34] F. Ambrosino et al. 'CHANTI: a Fast and Efficient Charged Particle Veto Detector for the NA62 Experiment at CERN'. In: *JINST* 11.03 (2016), P03029. DOI: 10.1088/1748-0221/11/03/P03029.

[35] A. Sergi. ‘NA62 Spectrometer: A Low Mass Straw Tracker’. In: *Physics Procedia* 37 (2012). Proceedings of the 2nd International Conference on Technology and Instrumentation in Particle Physics (TIPP 2011), pp. 530 –534. DOI: https://doi.org/10.1016/j.phpro.2012.03.713.

[36] S. Shkarovskiy. ‘NA62 spectrometer to search for $K^+ \to \pi^+\nu\bar{\nu}$’. In: *JINST* 12.02 (2017), pp. C02027–C02027. DOI: 10.1088/1748-0221/12/02/c02027.

[37] G. Anzivino et al. ‘Commissioning and performance of the NA62 RICH detector’. In: *NIM A* 876 (2017), pp. 84 –88. DOI: https://doi.org/10.1016/j.nima.2017.01.072.

[38] D. Aisa et al. ‘Mirror system of the RICH detector of the NA62 experiment’. In: *JINST* 12 (2017), P12017–P12017. DOI: 10.1088/1748-0221/12/12/P12017.

[39] G. Anzivino et al. ‘Precise mirror alignment and basic performance of the RICH detector of the NA62 experiment at CERN’. In: *JINST* 13.07 (2018), P07012. DOI: 10.1088/1748-0221/13/07/P07012.

[40] S. Kholodenko. ‘NA62 Charged Particle Hodoscope. Design and performance in 2016 run’. In: *JINST* 12.06 (2017), p. C06042. DOI: 10.1088/1748-0221/12/06/C06042.

[41] P. Massarotti et al. ‘The Large-Angle Photon Veto System for the NA62 Experiment at CERN’. In: *PoS* ICHEP2012 (2013), p. 504. DOI: 10.22323/1.174.0504.

[42] R. Ammendola et al. ‘The integrated low-level trigger and readout system of the CERN NA62 experiment’. In: *NIM* A929 (2019), pp. 1–22. DOI: 10.1016/j.nima.2019.03.012.

[43] B. Angelucci et al. ‘TEL62: an integrated trigger and data acquisition board’. In: *JINST* 7.02 (2012), pp. C02046–C02046. DOI: 10.1088/1748-0221/7/02/c02046.

[44] A. Kluge et al. ‘The TDCpix readout ASIC: A 75 Ps resolution timing front-end for the NA62 Gigatracker hybrid pixel detector’. In: *NIM A* 732 (2013), pp. 511–514. DOI: 10.1016/j.nima.2013.06.089.

[45] N. Azorskiy et al. ‘The NA62 spectrometer acquisition system’. In: *JINST* 11.02 (2016), pp. C02064–C02064. DOI: 10.1088/1748-0221/11/02/c02064.

[46] P. Lichard et al. ‘Performance evaluation of multiple (32 channels) sub-nanosecond TDC implemented in low-cost FPGA’. In: *JINST* 9 (Mar. 2014), p. C03013. DOI: 10.1088/1748-0221/9/03/C03013.

[47] Altera. *Cyclone III device handbook"*. URL: https://www.intel.com/content/www/us/en/programmable/products/fpga/cyclone-series/cyclone-iii/support.html.

[48] A. Ceccucci et al. ‘The NA62 liquid Krypton calorimeter’s new readout system’. In: *JINST* 9.01 (2014), pp. C01047–C01047. DOI: 10.1088/1748-0221/9/01/c01047.

[49] R. I. Marchevski. ‘First measurement of the $K^+ \to \pi^+\nu\bar{\nu}$ decay with the NA62 experiment at CERN’. Presented 19 Feb 2019. 2018. URL: http://cds.cern.ch/record/2663316.

[50] *NA62 Software Framework Documentation*. URL: https://na62-sw.web.cern.ch/sites/na62-sw.web.cern.ch/files/doxygen/index.html.

[51] *Geant4 Simulation ToolKit*. URL: https://geant4.web.cern.ch/.

[52] *ROOT Data Analysis Framework*. URL: https://root.cern.ch/.

[53] F. Brizioli. *Improved usage of RICH for $K^+ \to \pi^+\nu\bar{\nu}$ analysis of 2017 data*. https://na62.web.cern.ch/NA62/restricted/NotesDoc/NA62-19-08.pdf. NA62 Internal Note - NA62-19-08. 2019.

[54] J. Engelfried. *RICH Likelihoods in NA62*. URL: https://indico.cern.ch/event/452212/.

[55] R. Aliberti. ‘Particle Identification with Calorimeters for the Measurement of the Rare Decay $K^+ \to \pi^+\nu\bar{\nu}$ at NA62’. Presented 21 Jan 2019. 2018. URL: http://cds.cern.ch/record/2671696.

[56] G. Ruggiero and R. I. Marchevski. *$K^+ \to \pi^+\nu\bar{\nu}$ Selection*. https://na62.web.cern.ch/NA62/restricted/NotesDoc/NA62-18-04.pdf. NA62 Internal Note - NA62-18-04. 2018.

[57] G. Ruggiero. *New result on $K^+ \to \pi^+\nu\bar{\nu}$ from the NA62 experiment*. URL: https://indico.cern.ch/event/769729/.

[58] J. Nix et al. *Blind background prediction using a bifurcated analysis scheme*. 2007. arXiv: 0708.0318 [physics.data-an].

[59] R. I. Marchevski and G. Ruggiero. *$K^+ \to \pi^+\nu\bar{\nu}$ Analysis*. https://na62.web.cern.ch/NA62/restricted/NotesDoc/NA62-18-05.pdf. NA62 Internal Note - NA62-18-05. 2018.

[60] R. I. Marchevski. *New result on $K^+ \to \pi^+\nu\bar{\nu}$*. URL: https://indico.cern.ch/event/846814/.

[61] Morimitsu Tanimoto and Kei Yamamoto. 'Probing SUSY with 10 TeV stop mass in rare decays and CP violation of kaon'. In: *PTEP* 2016.12 (2016), 123B02. DOI: 10.1093/ptep/ptw160.

[62] NA62 Collaboration. *ADDENDUM I TO P326 Continuation of the physics programme of the NA62 experiment*. Tech. rep. CERN-SPSC-2019-039. SPSC-P-326-ADD-1. URL: https://cds.cern.ch/record/2691873.